

SHORT-TERM IRRADIANCE FORECASTING USING AN
IRRADIANCE SENSOR NETWORK AND DATA ASSIMILATION

by

Antonio Tomas Lorenzo

A Dissertation Submitted to the Faculty of the

COLLEGE OF OPTICAL SCIENCES

In Partial Fulfillment of the Requirements
For the Degree of

DOCTOR OF PHILOSOPHY

In the Graduate College

THE UNIVERSITY OF ARIZONA

This draft was generated on February 28, 2017.

THE UNIVERSITY OF ARIZONA
GRADUATE COLLEGE

As members of the Dissertation Committee, we certify that we have read the dissertation prepared by Antonio Tomas Lorenzo, titled Short-term irradiance forecasting using an irradiance sensor network and data assimilation and recommend that it be accepted as fulfilling the dissertation requirement for the Degree of Doctor of Philosophy.

Date: 14 April 2017

Alexander D. Cronin

Date: 14 April 2017

Matthias Morzfeld

Date: 14 April 2017

Barrett G. Potter Jr.

Final approval and acceptance of this dissertation is contingent upon the candidate's submission of the final copies of the dissertation to the Graduate College.

I hereby certify that I have read this dissertation prepared under my direction and recommend that it be accepted as fulfilling the dissertation requirement.

Date: 14 April 2017

Dissertation Director: Alexander D. Cronin

Date: 14 April 2017

Dissertation Director: Matthias Morzfeld

STATEMENT BY AUTHOR

This dissertation has been submitted in partial fulfillment of requirements for an advanced degree at the University of Arizona and is deposited in the University Library to be made available to borrowers under rules of the Library.

Brief quotations from this dissertation are allowable without special permission, provided that accurate acknowledgment of the source is made. Requests for permission for extended quotation from or reproduction of this manuscript in whole or in part may be granted by the head of the major department or the Dean of the Graduate College when in his or her judgment the proposed use of the material is in the interests of scholarship. In all other instances, however, permission must be obtained from the author.

SIGNED: Antonio Tomas Lorenzo

TABLE OF CONTENTS

LIST OF FIGURES	6
LIST OF TABLES	8
ABSTRACT	9
CHAPTER 1 INTRODUCTION	10
1.1 State of Solar Power in the Southwest and Future Challenges	13
1.2 Solar Irradiance Forecasting	16
1.3 This Dissertation in Brief	19
CHAPTER 2 IRRADIANCE MONITORING NETWORK	32
2.1 Design of Custom Sensors	32
2.1.1 Photodiode Sensor	33
2.1.2 Hardware	34
2.1.3 Software	36
2.1.4 Possible Improvements	39
2.2 Rooftop PV Systems as Sensors	39
2.3 Network Deployment	40
CHAPTER 3 IRRADIANCE NETWORK FORECASTS	43
3.1 Irradiance Forecast Error Metrics	44
3.1.1 Example Forecasts	45
3.1.2 Taylor Diagrams	47
3.1.3 Suggestions	50
3.2 Future Work	50
CHAPTER 4 OPTIMAL INTERPOLATION TO IMPROVE SATELLITE NOWCASTS WITH DATA	52
4.1 Satellite to Irradiance Algorithms for OI	52
4.1.1 UASIBS Model	52
4.1.2 Semi-Empirical Model	53
4.1.3 Other Models	55
4.2 Correlation Parameterization	56
4.3 Parameter Estimation	60
4.4 Image Position Errors	62
4.5 Future Work	64

TABLE OF CONTENTS – *Continued*

CHAPTER 5 FUTURE WORK	65
5.1 Satellite Image Forecasts	65
5.2 Cloud Data Assimilation in WRF	69
5.3 Ensemble WRF Forecasting	69
5.4 Intelligent Forecast Fusion	69
CHAPTER 6 SOFTWARE	71
CHAPTER 7 CONCLUSIONS	72
7.1 Future Work	72
REFERENCES	73
APPENDIX A REPRINT: SHORT-TERM PV POWER FORECASTS BASED ON A REAL-TIME IRRADIANCE MONITORING NETWORK	76
APPENDIX B REPRINT: IRRADIANCE FORECASTS BASED ON AN IRRADIANCE MONITORING NETWORK, CLOUD MOTION, AND SPATIAL AVERAGING	82
APPENDIX C REPRINT: OPTIMAL INTERPOLATION OF SATELLITE DERIVED IRRADIANCE AND GROUND DATA	95
APPENDIX D REPRINT: OPTIMAL INTERPOLATION OF SATELLITE AND GROUND DATA FOR IRRADIANCE NOWCASTING AT CITY SCALES	102
APPENDIX E LIST OF PUBLICATIONS CO-AUTHORED BY A. T. LORENZO	112

LIST OF FIGURES

Figure 1.1	Annual installations of solar PV in the US	10
Figure 1.2	Variable power output of a 28 MW solar power plant	12
Figure 1.3	Heatmaps of SVERI load, solar power, wind power, and renewable load fraction	14
Figure 1.4	Heatmaps of temperature, dewpoint, irradiance, and wind speed	15
Figure 1.5	Projected SVERI 2027 duck curves	16
Figure 1.6	Forecast horizon for various forecast types	18
Figure 1.7	Wind speed and GHI output from UA-WRF	19
Figure 1.8	Speculative errors for various forecasting techniques	20
Figure 1.9	Irradiance forecast errors across forecast horizons	21
Figure 1.10	Picture of a sensor deployment.	23
Figure 1.11	One sensor predicting the output of another	24
Figure 1.12	Illustration of the network forecast methodology	27
Figure 1.13	Example of a sensor's influence on network forecasts	28
Figure 1.14	Taylor diagram for the network and various persistence forecasts	29
Figure 1.15	Satellite image and irradiance estimate	30
Figure 1.16	Improved satellite irradiance estimates using optimal interpolation	31
Figure 2.1	Comparison of photodiode and pyranometer signals	33
Figure 2.2	Custom sensor circuit diagram	35
Figure 2.3	Assembled sensor circuit board	36
Figure 2.4	Interior of the sensor enclosure	37
Figure 2.5	A complete custom sensor	38
Figure 2.6	Map of sensor locations	41
Figure 3.1	Example of data from one sensor predicting the output of another	44
Figure 3.2	Forecasts for a day with thick, broken clouds	46
Figure 3.3	Forecasts for a day with scattered clouds	46
Figure 3.4	Taylor diagram for day 1 example forecasts	48
Figure 3.5	Taylor diagram for day 2 example forecasts	49
Figure 4.1	Scatterplot of predicted vs measured clear-sky index for UASIBS	54
Figure 4.2	Scatterplot of predicted vs measured clear-sky index for the semi-empirical model	55

LIST OF FIGURES – *Continued*

Figure 4.3	Clearness versus Cloudiness for SE model on 4/19	57
Figure 4.4	Clearness versus Cloudiness for SE model on 6/15	58
Figure 4.5	Clearness versus Cloudiness for UASIBS on 6/15	59
Figure 4.6	Optimization surfaces for OI parameters	61
Figure 4.7	An example of a failure of the geolocation correction	63
Figure 5.1	Map of all available irradiance sensors	66
Figure 5.2	Comparison of visible images from the current and future GOES	67
Figure 5.3	An visible image of the western US from GOES-16	68

LIST OF TABLES

1.1	Error statistics for network forecasts	22
1.2	Optimal interpolation error metrics	25
3.1	Error metrics for contrived test forecasts	47

ABSTRACT

write abstract as simple text here

CHAPTER 1

INTRODUCTION

The installed capacity of solar power in the US continues to grow as a result of aging coal and natural gas power plants, lower costs, state renewable portfolio standards, and efforts to decarbonize the electrical grid. As shown in Figure 1.1, this growth has been steady since 2010 and shows no signs of abating.

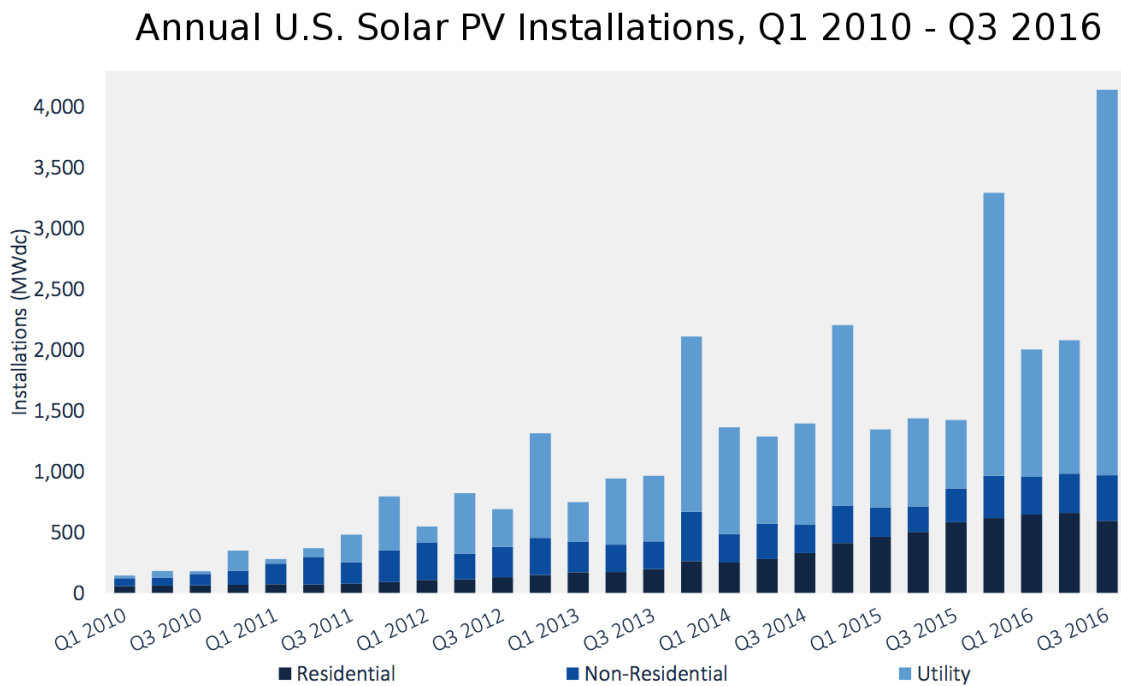


Figure 1.1: Annual installations of solar photovoltaic (PV) systems in the US.
[Source: [1]]

Sunlight is the fuel that drives all solar power plants. Unlike sources of fuel for conventional power generators like coal or natural gas, the solar resource is highly variable due to the chaotic nature of the weather. This variability of the solar resource leads to uncertainty at the electric utility and increases management

costs [2]. Forecasts help utilities manage the variability in a number of ways [3, 4], including the optimal dispatch of battery storage [5]. Ultimately, better forecasts increase the amount of solar power that utilities add to the grid.

An example of the variability that a 28 MW power plant experiences due to clouds is shown in Fig. 1.2. The power plant starts producing power near sunrise, and reaches its peak power output of 28 MW in a few hours. However, clouds begin moving over the plant in the afternoon causing large fluctuations in the power. Ramps (change in power per time) as large as 25 MW occur in a span of 5 minutes. This means the utility needs to have generation standing by to provide the power when a cloud passes over the plant and turn off quickly when the power returns in order to always match the electricity load and generation.

This dissertation will explore solar forecasting techniques that incorporate data from a ground sensor network. First, the current state of solar power in the Southwest US and a brief overview of general solar forecasting methods will be discussed. Then, a brief overview of solar irradiance forecasting methods will be presented. Finally, a summary of the work in this dissertation will be provided.

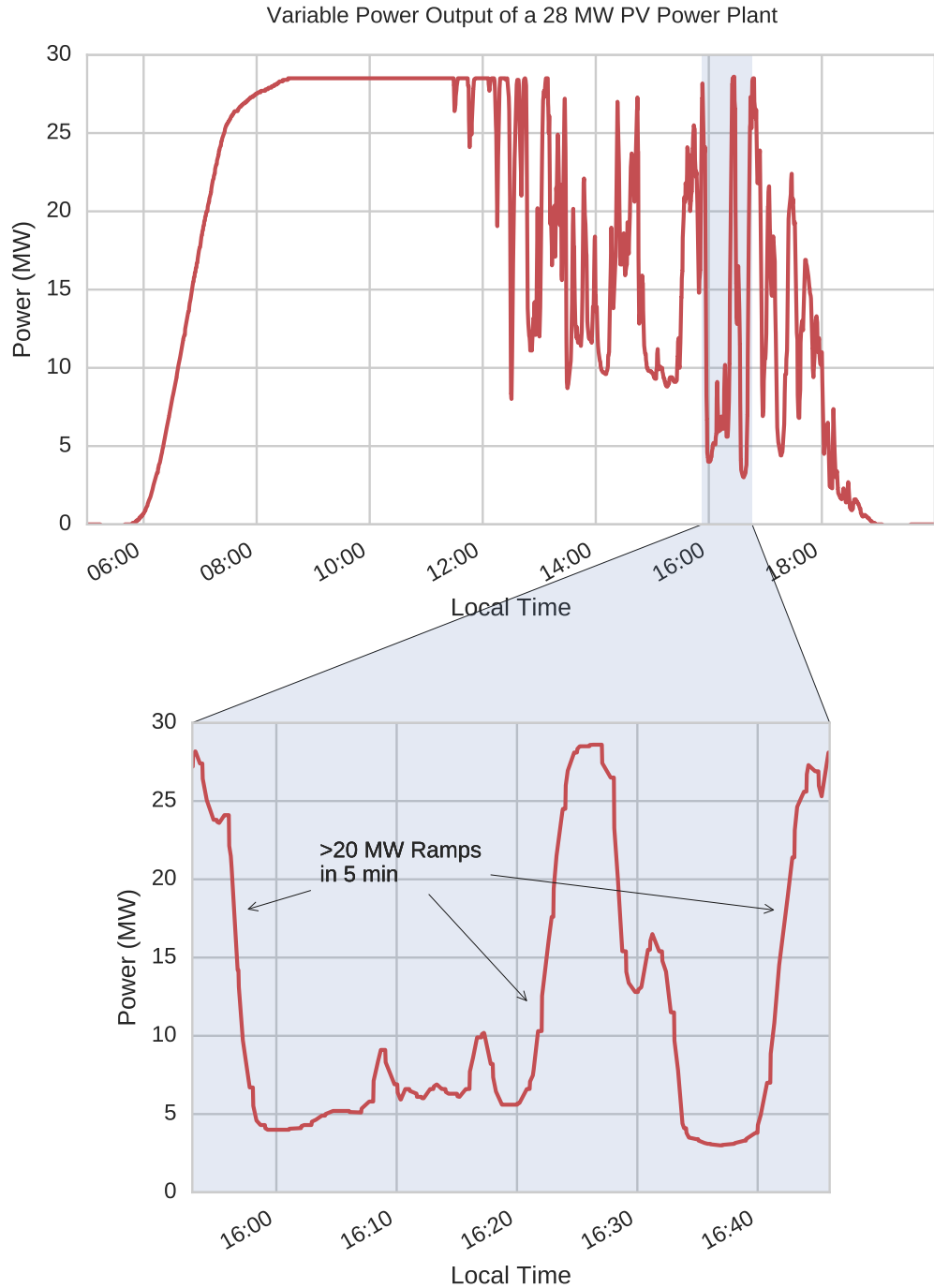


Figure 1.2: Power output of a 28 MW power plant near Tucson, AZ on a variable day. Changes in power as large as 25 MW can occur in a span of only 5 minutes. This variability stresses the grid, but can be handled with proper forecasting.

1.1 State of Solar Power in the Southwest and Future Challenges

As of early 2017, members of the Southwest Variable Energy Resource Initiative (SVERI) have a total of 1100 MW of installed solar capacity, 800 MW of installed wind capacity, and a peak load of 23 GW [?]. Another roughly 1 GW of generation comes from distributed generation (DG) solar systems that are installed on residential or commercial rooftops. Heatmaps showing the time of day load, wind and solar generation, and wind and solar fraction of load for two years are shown in Fig. 1.3. Heatmaps for weather variables at the University of Arizona are shown in Fig. 1.4 to correlate weather to, for example, the abrupt decrease in load around 10/14 corresponding to the end of monsoon season.

Utilities in Arizona are well on their way to generate 15% of their energy from renewable resources by 2025 as required by the Arizona Renewable Energy Standard and Tariff [?]. As mentioned above, DG solar systems provide a large fraction of the total renewable energy generation. One problem utilities encounter with DG systems is that real-time monitoring is limited. Since the power generated by these systems can also be consumed on site, variability in DG power is visible to the utilities as variability in the load. Real-time estimates (or nowcasts) and forecasts of this DG variability will be required for the most accurate load forecasts.

Similar to DG, utilities may consider power generated at large solar and wind power plants to be modifiers of the load instead of plants that are controlled and dispatched. Utilities are then interested in what they call the net load or the total load minus the generation from solar and wind power plants. Based on projections from 2014 SVERI data, we project net load profiles will resemble those in Fig. 1.5. Notice the large power ramps that occur in the so called duck curve in November. Dealing with these 3 GW ramps in only a few hours would cost a great deal if utilities rely only on the current grid technology. Using forecasts, utilities can better control large solar and wind power plants and avoid some of these large ramps. Other smart grid technologies such as energy storage and time of use rates will also play a critical role in maintaining the reliability of the future grid.

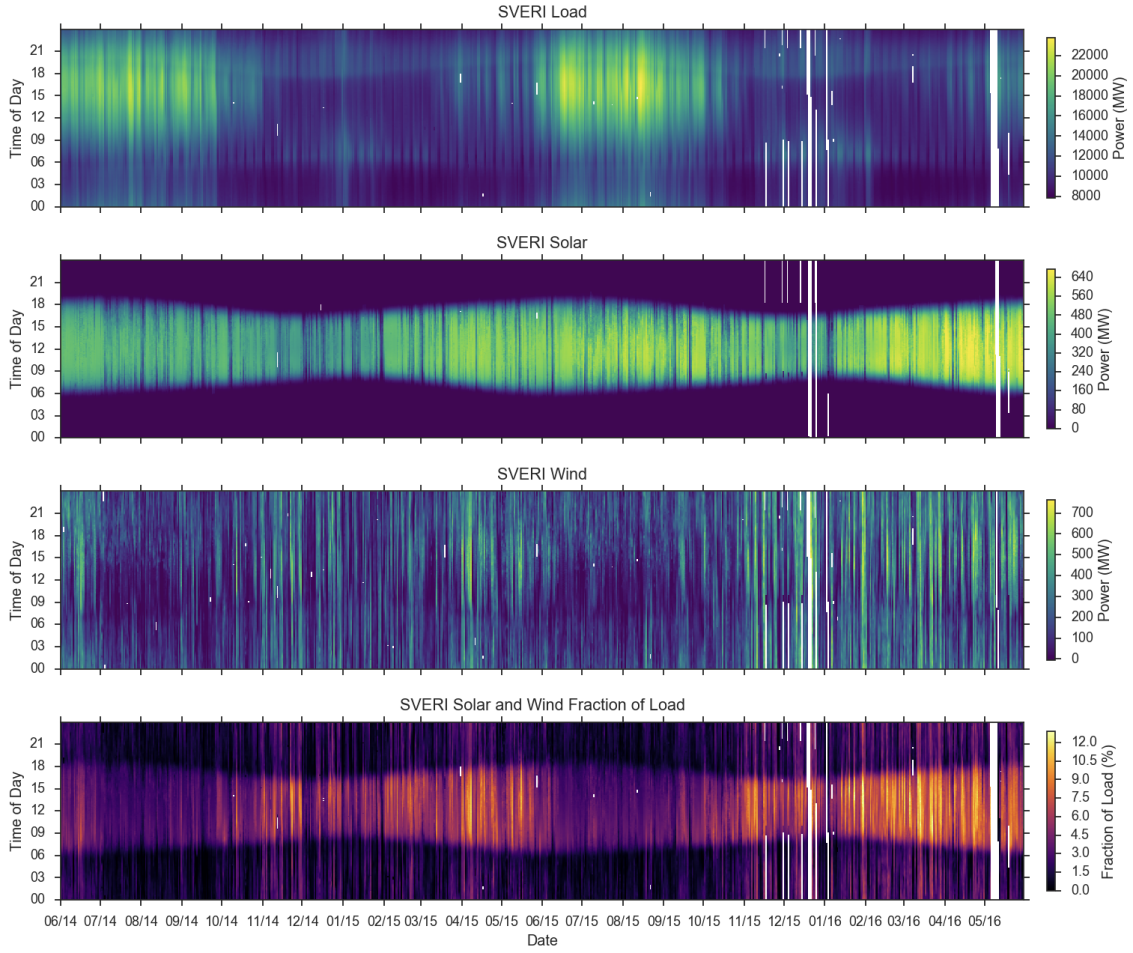


Figure 1.3: Time of day heatmaps of SVERI load, solar power generation, wind power generation, and the fraction of load served by solar and wind power. The heatmaps were generated with two years of data and the white areas indicate missing data. The diurnal cycle is clearly seen in the solar data, and can also be found in the wind and load. A weekly cycle is also evident in the load. At times in the spring when heating and cooling loads are low and their is high solar generation, wind and solar power can serve up to 12% of the load.

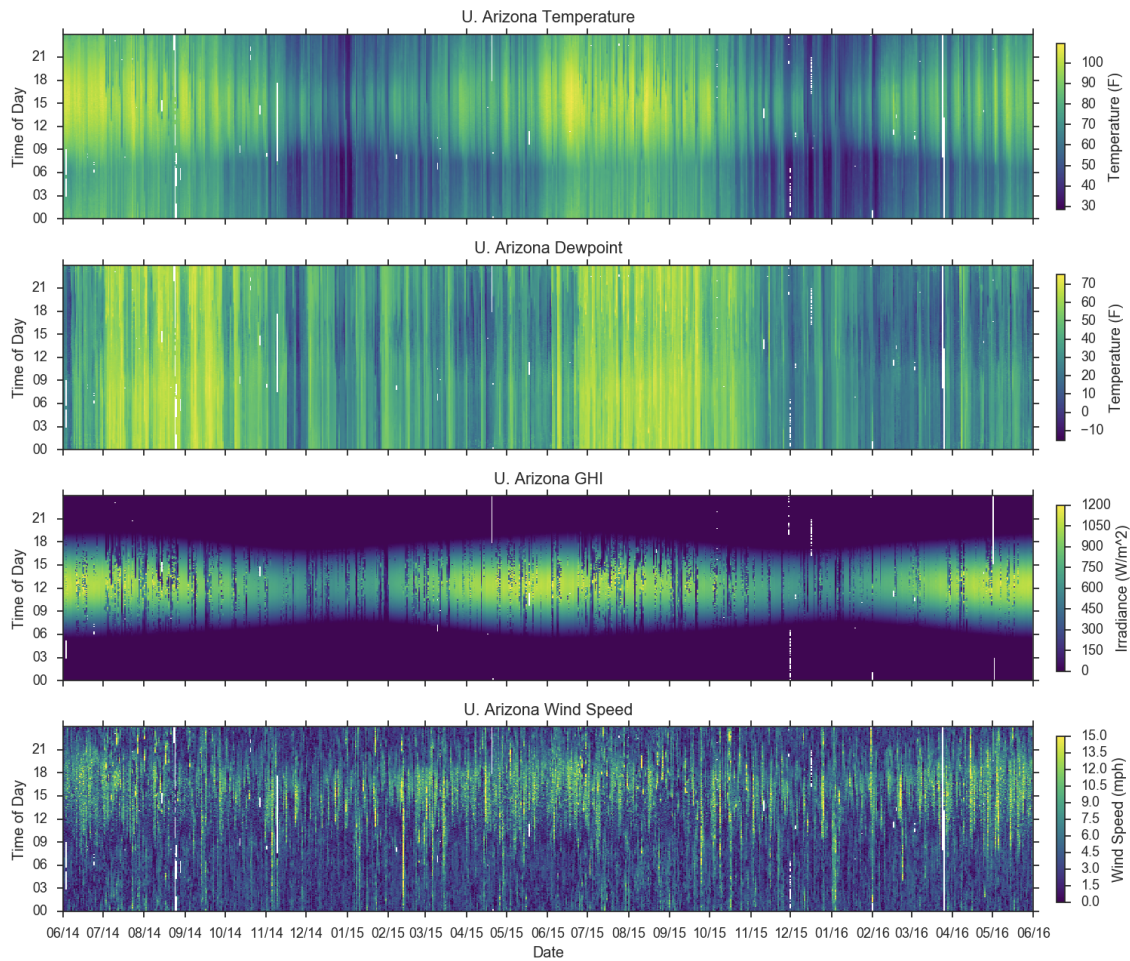


Figure 1.4: Time of day heatmaps for temperature, dewpoint, global horizontal irradiance (GHI), and wind speed all measured at the University of Arizona in Tucson. Notable features include the many clear days evident in the GHI heatmap and the beginning and end of the monsoon season (when moisture from the Gulf of California moves into Arizona) visible in the dewpoint heatmap.

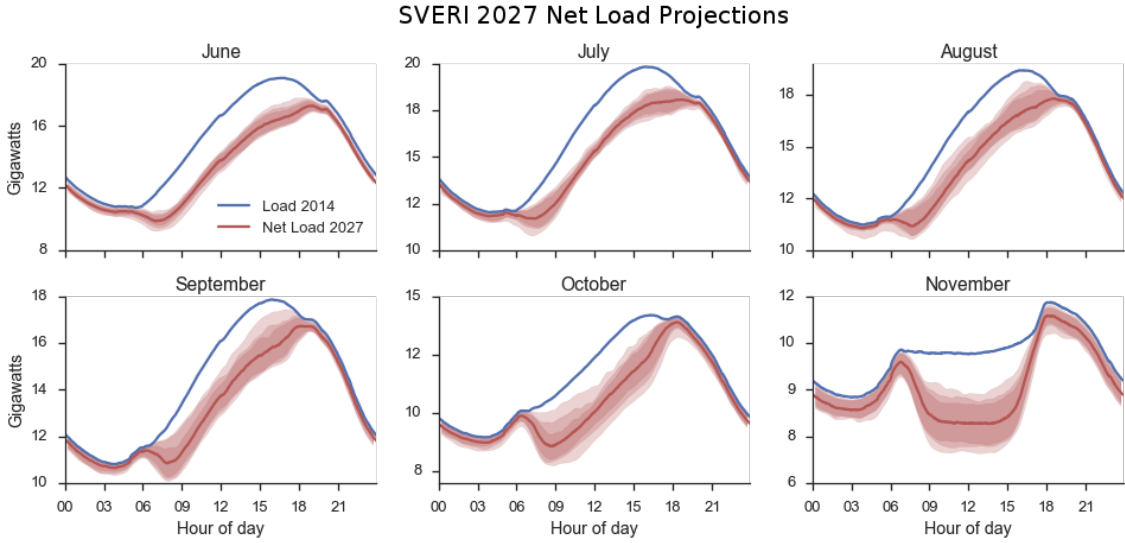


Figure 1.5: Net load (total load minus wind and solar generation) projections for SVERI in 2027 if utilities continue business as usual. The shape of the November net load is referred to as a duck curve. Forecasts along with storage and other policies will help utilities change how solar and wind power are controlled to avoid these multi-GW ramps. Figure produced as a part of the SVERI?? report?

The remainder of this dissertation will focus on the primary input to solar power plants: sunlight. We will specifically refer to solar irradiance or the amount of sunlight in a given area that can perform useful work.

1.2 Solar Irradiance Forecasting

As mentioned above, the solar irradiance that reaches the Earth's surface is variable. The first obvious source of variability is the diurnal cycle due to the movement of the sun through the sky. The second major source of variability is due to clouds blocking light from the sun from reaching the surface of the Earth. Aerosol, dust particles, and water vapor in the atmosphere can also reduce sunlight, although they often only account for a small reduction unless there is a dust storm or dense smog.

There are three primary classification of the radiation that reaches the Earth's surface as shown in ???. The first is the radiation that comes in a straight path directly from the sun called direct irradiance. The direct irradiance that strikes the

earth at a normal angle is called the direct normal irradiance (DNI). Light can also reach the surface by being scattered in the atmosphere by clouds or aerosols and is referred to as diffuse irradiance. The total diffuse irradiance that strikes a horizontal surface on the Earth is referred to as the diffuse horizontal irradiance (DHI). The sum of the direct and diffuse irradiance is referred to as the global irradiance, and the total direct and diffused irradiance on a horizontal surface is called the global horizontal irradiance (GHI).

The majority of solar power plants are non-concentrating systems that collect both direct and diffuse radiation, thus we will focus on techniques that forecast GHI. Furthermore, we are interested in producing forecasts that will, after being converted to solar power forecasts, be used to maintain grid reliability and for power market trading. Thus, we will focus on forecasts that forecast the irradiance now out to the irradiance a week from now.

Forecasting techniques are often compared based on the range of forecast horizons where they outperform a reference forecast as shown in Fig. 1.6. This reference can be a persistence forecast that assumes the irradiance in the future will be the same as it is currently or a forecast based on climatology.

Cloud camera forecasts have been shown to outperform persistence forecasts at time horizons from 1? minute to 30 minutes []. These forecasts are produced using estimates of cloud location and thickness from a camera with a fisheye lens pointed at the sky. A number of active forecasts

Statistical forecasts are those that rely on measured irradiance data. Many types of persistence forecasts fall into this category. Other techniques include ARIMA, ARMA, lasso, ANN, etc

Network forecasts are a type of statistical forecast that will be studied in depth in this dissertation. These forecasts depend data from a network of irradiance sensors deployed over a large area, and they outperform the reference persistence forecast for time horizons from 1 minute to 2 hours in the future. These forecasts are discussed further in Chapter 3.

Satellite forecasts are forecasts that rely on estimates of irradiance produced

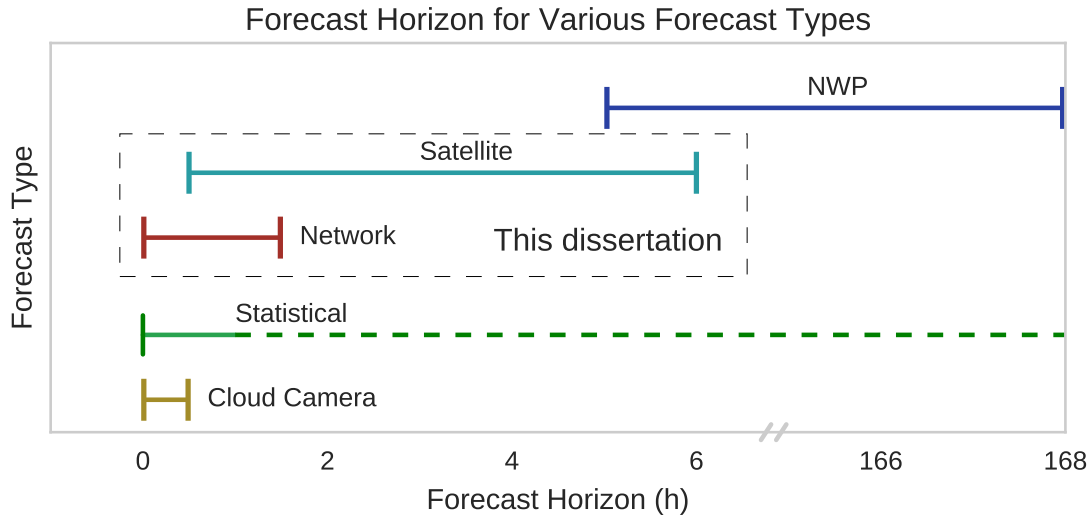


Figure 1.6: The optimal forecast horizons for various types of short-term forecasts. This dissertation will focus on network and satellite forecasts. NWP refers to numerical weather predictions.

from images taken by geostationary satellites. These estimates can be categorized into semi-empirical and physical models. Semi-empirical models rely on historical data from the satellite and ground sensors to find the function that translates from satellite image pixel to observed irradiance. Physical models try to use the satellite images to infer properties about the clouds which are then used in a radiative transfer model to predict the sunlight that reaches the surface. Improvements to these irradiance estimates using ground data and data assimilation will be explored in Chapter 4.

Forecasts that predict irradiance for time horizons greater than a few hours and up to about a week rely on numerical weather predictions (NWP). These are dynamic models of the atmosphere that must parameterize various processes. One benefit is that NWP forecasts cover a large area. We produce NWP forecasts using the Weather Research and Forecasting (WRF) [?] at the University of Arizona with customized settings for the Southwest. Example wind speed and GHI outputs from the UA-WRF model are shown in Fig. 1.7. Chapter 5 has discussion of possible improvements for UA-WRF forecasts.

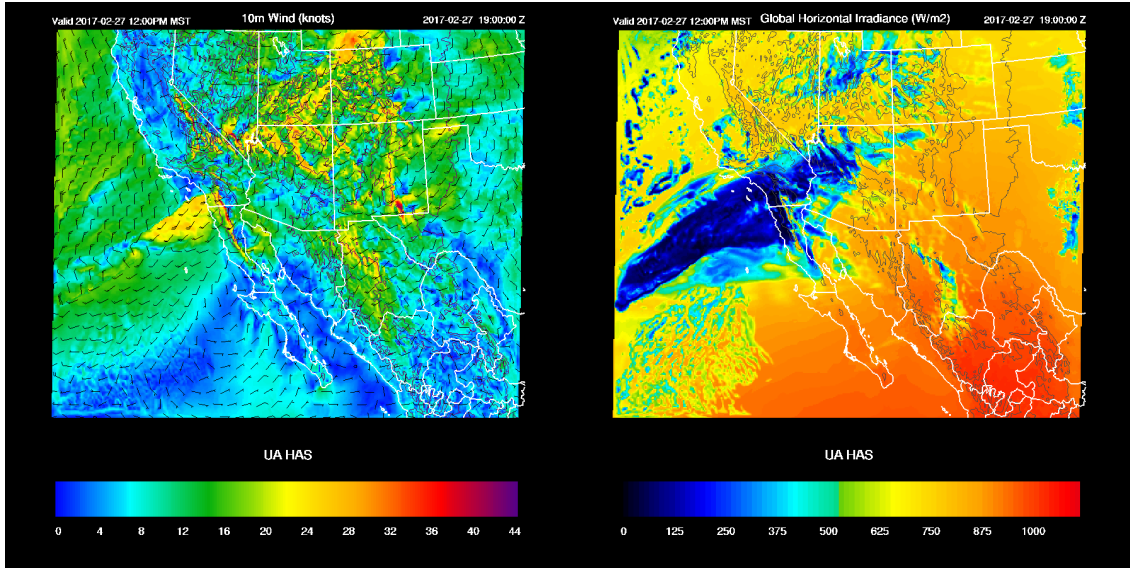


Figure 1.7: Example wind speed near the surface and GHI outputs from the WRF model run at the University of Arizona.

There is also active research in hybrid forecasts that combine different forecasting techniques to improve forecasts across horizons. citations

1.3 This Dissertation in Brief

Figure 1.8 shows speculative estimates of forecast errors as a function of forecast horizon created near the start of this dissertation work. This dissertation works to analyze forecasting methods and measure their errors as a function of forecast horizon in order to produce the best forecasts of solar irradiance in the Southwest. Figure 1.9 shows the culmination of this work.

The specific forecasting methods studied in this dissertation rely on a network of irradiance sensors. A network with sufficient density and time resolution did not exist in Tucson at the start of this dissertation work, so we set out to design and deploy inexpensive sensors. The design and deployment of the network is described in Chapter 2. For the period of April to July 2014, we collected data from about 50 custom sensors and rooftop PV systems to use in subsequent studies. All data was

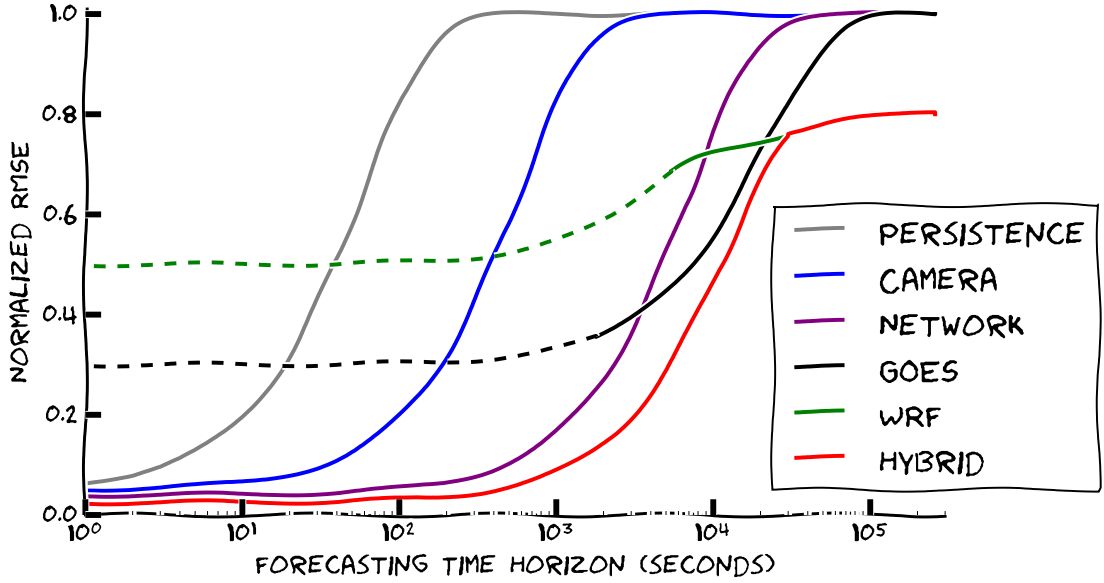


Figure 1.8: Speculative root mean squared errors (RMSE) for various types of forecasts.

detrended to clear-sky index using the expectation of the output of each sensor on a clear day.

With this irradiance network data, the first forecasting methodology we implemented and analyzed relies only on data from the network as described in Chapter 3. This forecast is labeled as network in Fig. 1.9.

The basic idea behind this type of forecast is depicted in Fig. 1.11 where the output of sensor 19 can predict what the output of sensor 31 will be in 8 minutes. To generate forecast in practice, we first collect data from the sensors and interpolate between them to produce a kind of cloud map as shown in Fig. 1.12. Then, using a vector representing the cloud motion, we can move this map to produce a forecast at any point. The errors for this type of forecast were studied in depth and a sample of those errors is shown in Table 1.1. While this method has many paths to improvement, forecasts produced in this way outperform a persistence forecast by 20% on average.

While analyzing this network forecast, we also carefully analyzed various types

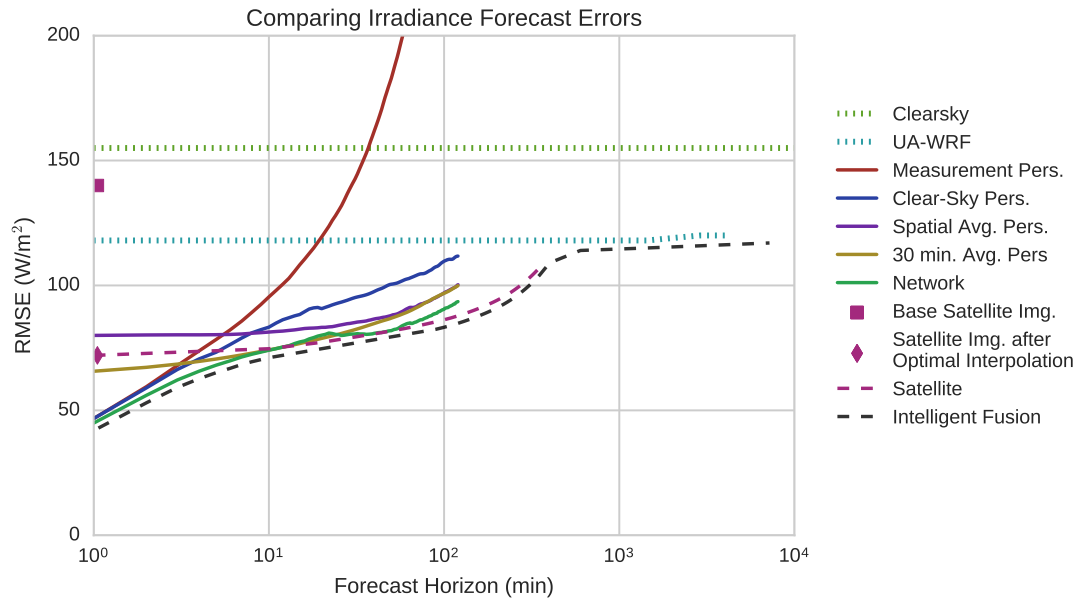


Figure 1.9: A comparison of irradiance forecast root-mean squared errors (RMSE) across many time horizons. Pers. refers to persistence, and UA-WRF refers to the numerical weather models generated at the UA using the Weather Research and Forecasting (WRF) model. The intelligent fusion is a theoretical combination of forecasts at different time horizons for the best forecast at all horizons. The solid lines (and points) indicate forecasts that will be studied in depth in this dissertation. Dotted lines are based on preliminary analysis, but have not been studied in depth. Dashed lines are forecasting techniques that will be studied in future work. The persistence and network forecasts will be discussed in Chapter 3 and the satellite image points will be discussed in Chapter 4.

Table 1.1: Summary of error statistics for network forecasts for the 46 days with clouds. Error statistics were calculated for the entire dataset at once. Only forecasts and data with solar zenith angle less than 75° were used. The mean irradiance was $\bar{y} = 662 \text{ W/m}^2$ and the mean clear-sky index was $\bar{k} = 0.92$.

FH	rMAE (%)	MAE (W/m ²)	MBE (W/m ²)	rRMSE (%)	RMSE (W/m ²)	Avg. skill (%)
1 min	4.96	30.97	-1.44	11.90	82.55	22.96
3 min	7.51	48.13	-1.39	15.89	110.46	23.09
5 min	9.29	59.59	-3.91	18.67	127.06	19.65
10 min	11.39	71.38	-8.59	22.11	141.44	18.63
20 min	13.23	82.39	-10.46	24.03	152.84	18.66
30 min	13.95	86.57	-7.52	24.49	154.15	21.21
60 min	15.45	95.59	-6.65	26.59	160.72	21.00
120 min	17.02	106.51	-2.01	29.20	172.45	19.58



Figure 1.10: Picture of a sensor deployment.

of persistence forecasts to understand how the network forecast works. Figure 1.13 shows that network forecasts do incorporate data from the sensors to improve errors, but at some times the errors in the network forecast closely resembles the errors of persistence forecasts. We found that smoother forecasts, or those with lower variance as compared to the observations, may seem to perform better than forecasts with higher variance when error metrics are considered in isolation. Using the Taylor diagram shown in Fig. 1.14, we show that network forecasts transition from matching the observation's variance to essentially becoming an area average persistence forecast after about 20 minutes. More details on how to interpret this diagram are described in Chapter 3. Thus, we claim that network forecasts are an improvement over spatial or time averaged persistence forecasts even if they may have similar RMSE values.

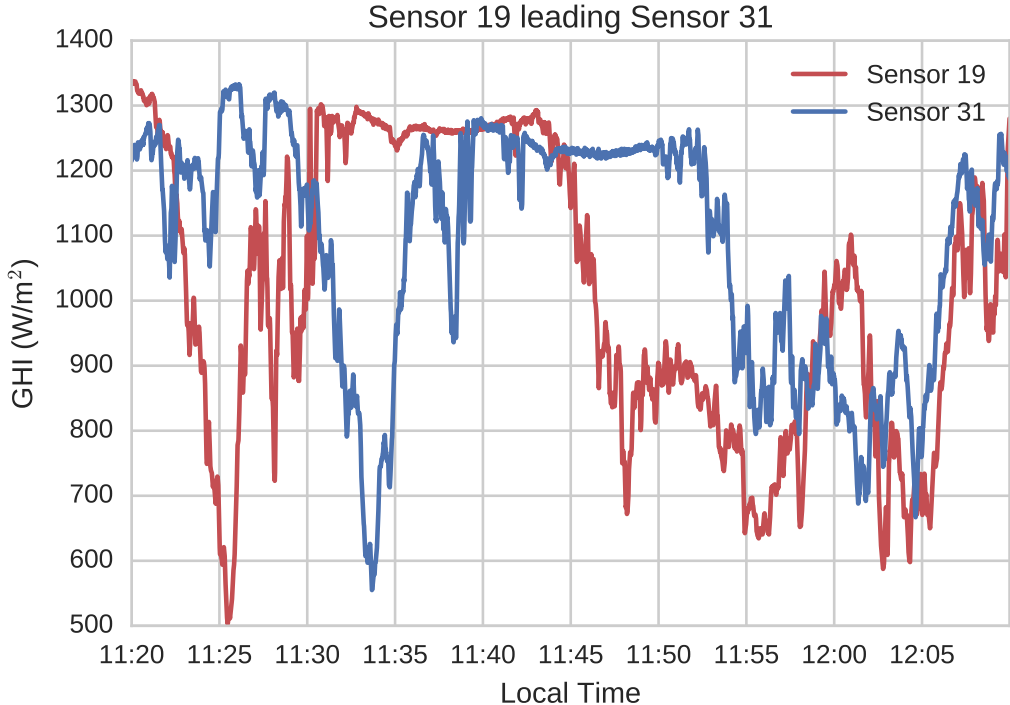


Figure 1.11: An example of the output of sensor 19 predicting the output of sensor 31 with a roughly 8 minute lead time. This type of correlation is the basis for the network forecasts.

With short-term forecasts covered by the network forecasts, we began studying forecasts derived from satellite images. A number of algorithms exist that convert images of the tops of clouds from geostationary satellites to images of irradiance on the ground. An example of such conversion is shown in Fig. 1.15. Naturally, this conversion from cloud top brightness to the amount of radiation that passes through clouds is error prone. We found that these satellite derived irradiance estimates from a current image (pink square on left axis of Fig. 1.9), before any forecasting is involved, had errors nearly as large as always assuming the sky were clear. It is unlikely that producing a forecast from such a nowcast would reduce errors, so satellite derived forecasts would quickly become worse than a clear-sky forecast, at least in terms of RMSE. Thus, in order to produce high quality forecasts from satellite derived irradiance images, we first improved the satellite derived irradiance

nowcasts.

Better satellite derived irradiance nowcasts were generated by again using data from the irradiance sensor network as described in Chapter 4. Using a data assimilation method known as optimal interpolation (OI), we combined the sensor data with the satellite derived irradiance based on the relative errors between them. We also parameterized the correlations between pixels in the satellite images in various ways. These correlations are responsible for spreading information from the sensor locations to other locations throughout the image. An example of improvements using OI is shown in Fig. 1.16.

Table 1.2: Error statistics for the NREL MIDC sensor on the University of Arizona campus. The analysis was computed with only the MIDC sensor withheld and averaged over the verification data set, and cloudiness covariance was used. Both the UASIBS and SE models show improvements and have a similar analysis RMSE. Units are W/m².

	MBE	MAE	RMSE
UASIBS Analysis	4.16	27.2	71.1
UASIBS Background	20.7	38.8	98.8
SE Analysis	11.2	36.0	72.7
SE Background	-86.1	107	140

We found significant improvements using this method after various complicating factors such as misalignment in the satellite image relative to the ground sensors were corrected. The improved nowcasts RMSE is shown as the pink diamond in Fig. 1.9 and in Table 1.2. We also found that this method to improve satellite irradiance nowcasts is applicable to a number of satellite to irradiance algorithms.

To produce forecasts of irradiance in future work, one might use a forecasting method that relies on only cloud advection. With a forecasting model in place, optimal interpolation can be extended to the Kalman filter with constantly incorporates new data into a forecast while also retaining information about past data. It is common in numerical weather prediction to use an ensemble of states to propagate and Kalman filter. An ensemble in this case also allows for each forecast to have a

different cloud motion field which may improve the final forecasts.

Satellite forecasts have been shown to perform well for forecast horizons up to 6 hours. For longer forecast horizons, numerical weather models are likely needed. We currently run the Weather Research and Forecasting (WRF) model with a custom configuration for Arizona. Improvements in the WRF model may come from assimilating satellite data, data from the sensor network, or studying WRF ensembles.

Finally, once high-quality forecasts are available for all forecast horizons, they can be intelligently fused to produce a single forecast that incorporates the best properties of each forecast methodology. Utilities and other stakeholders often need these fused forecasts to make decisions.

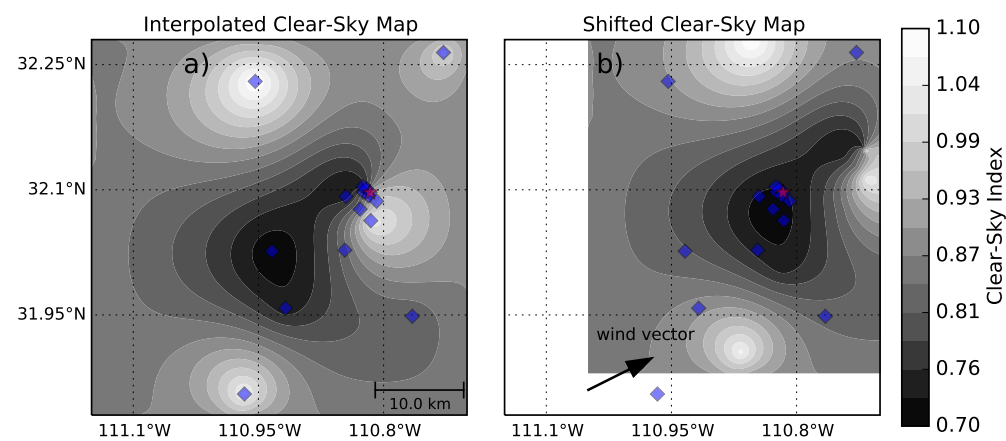


Figure 1.12: An example interpolated map produced from the sensor network data is shown in a). Using an estimated cloud motion vector, this map is shifted according to the lead forecast horizon as shown in b).

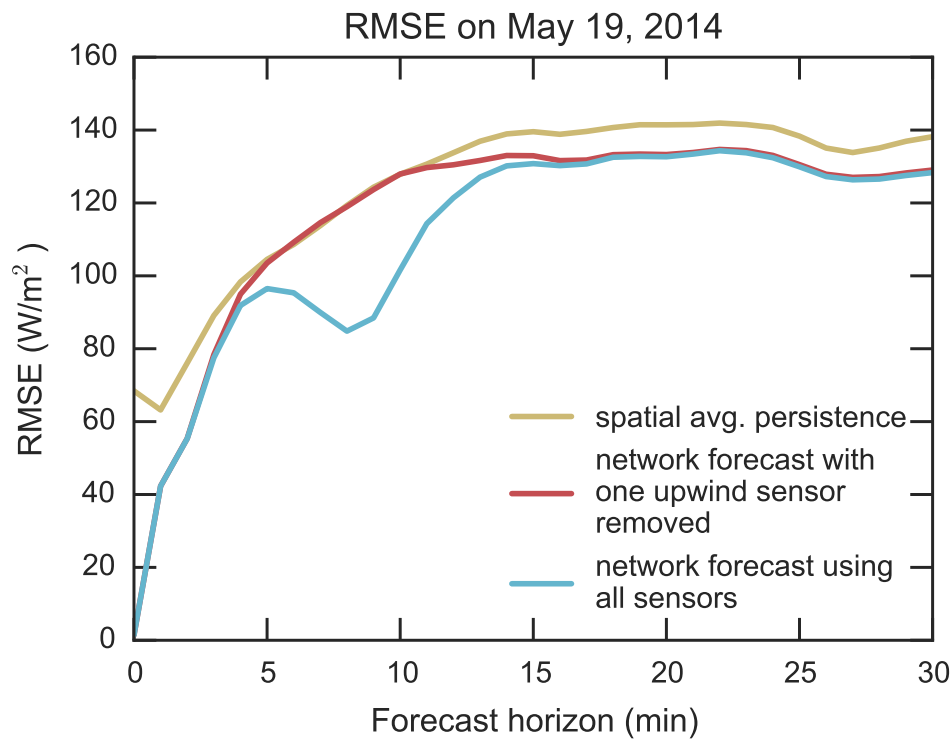


Figure 1.13: RMSE vs forecast horizon on May 19, 2014 for network forecasts made with all the sensors in the network (blue) and with one upwind sensor removed (red), along with a spatially-averaged persistence forecast (yellow). The dip at 7 min for the forecast using the full network illustrates that properly placed upstream sensors do improve forecasts over a simple spatial average.

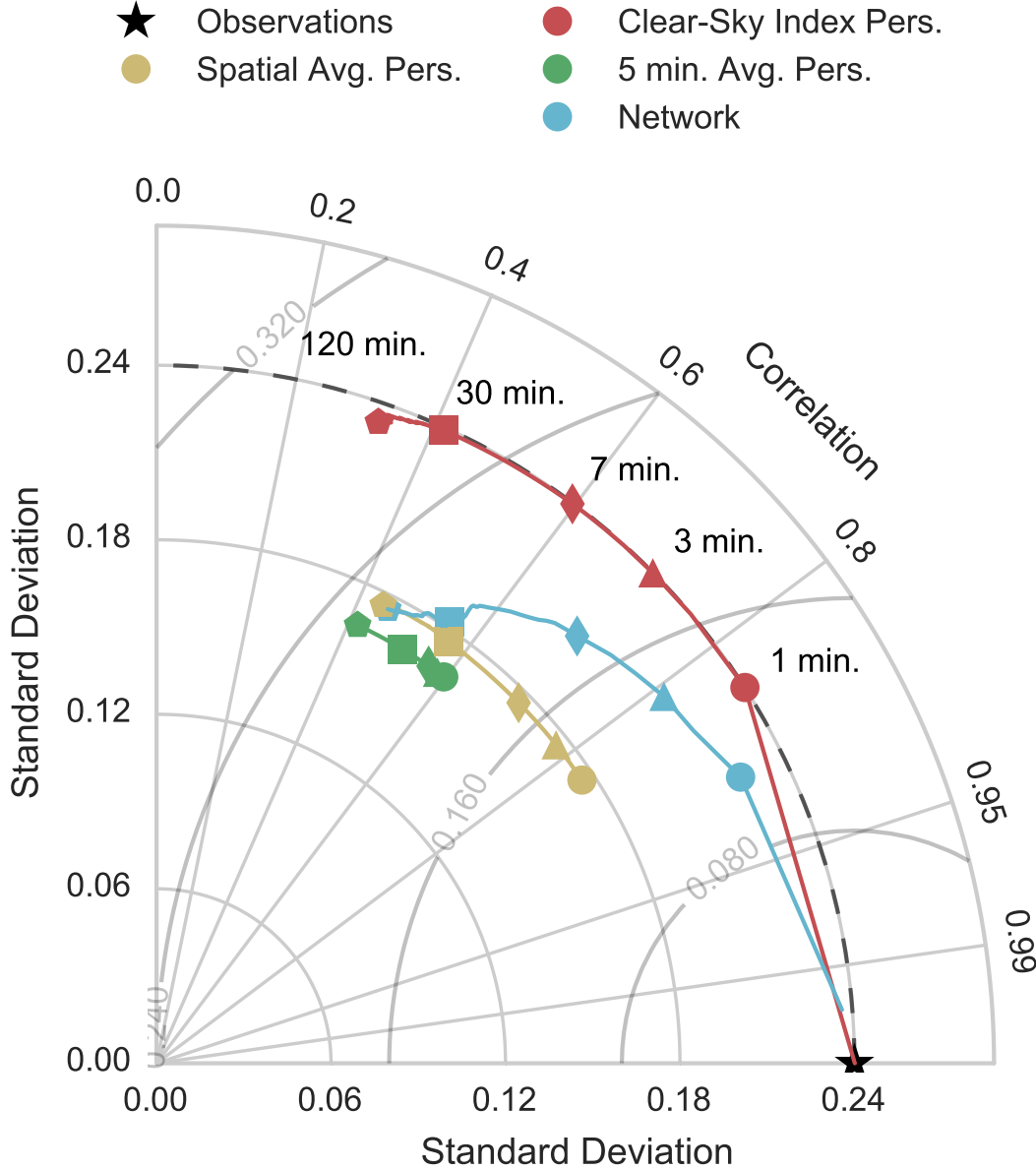


Figure 1.14: Taylor diagram for clear-sky index persistence (red), spatially-averaged persistence (yellow), 5-min time-averaged persistence (green), and network (light blue) forecasts for 1 min (circle), 3 min (triangle), 7 min (diamond), 30 min (square), and 120 min (pentagon) forecast horizons. The black dashed line indicates the standard deviation of the data. Solid contours around the observations point are lines of constant CRMSE. Forecasts for clear-sky index were used so all quantities are dimensionless. At the 120 min forecast horizon, the spatially-averaged persistence and network points overlap. Network forecasts start with a standard deviation near that of the measurements, but this decreases at longer time horizons as the network forecast begins to resemble spatially-averaged persistence.

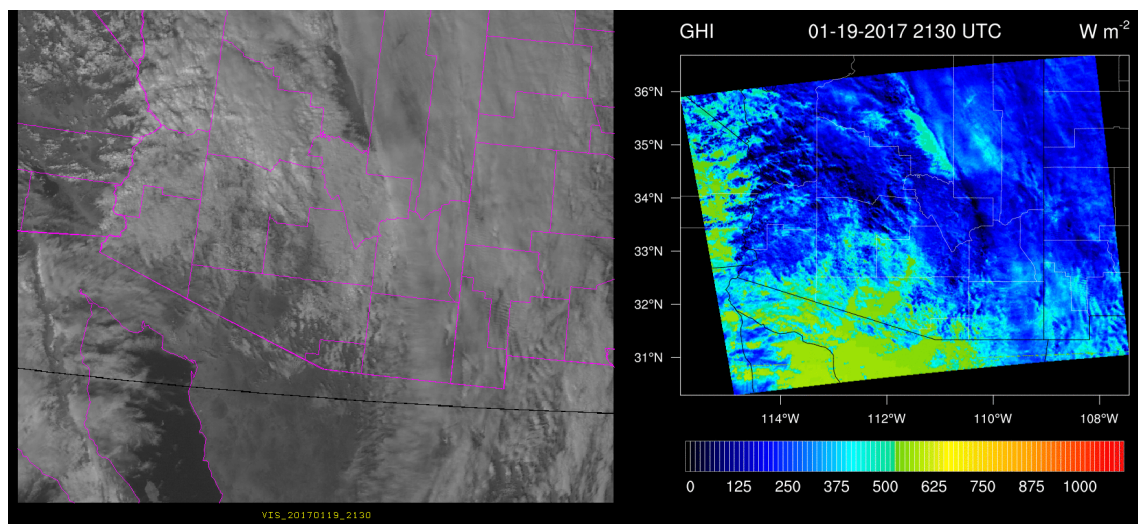


Figure 1.15: A satellite image captured by a geostationary satellite (left) and the GHI produced from this image (right).

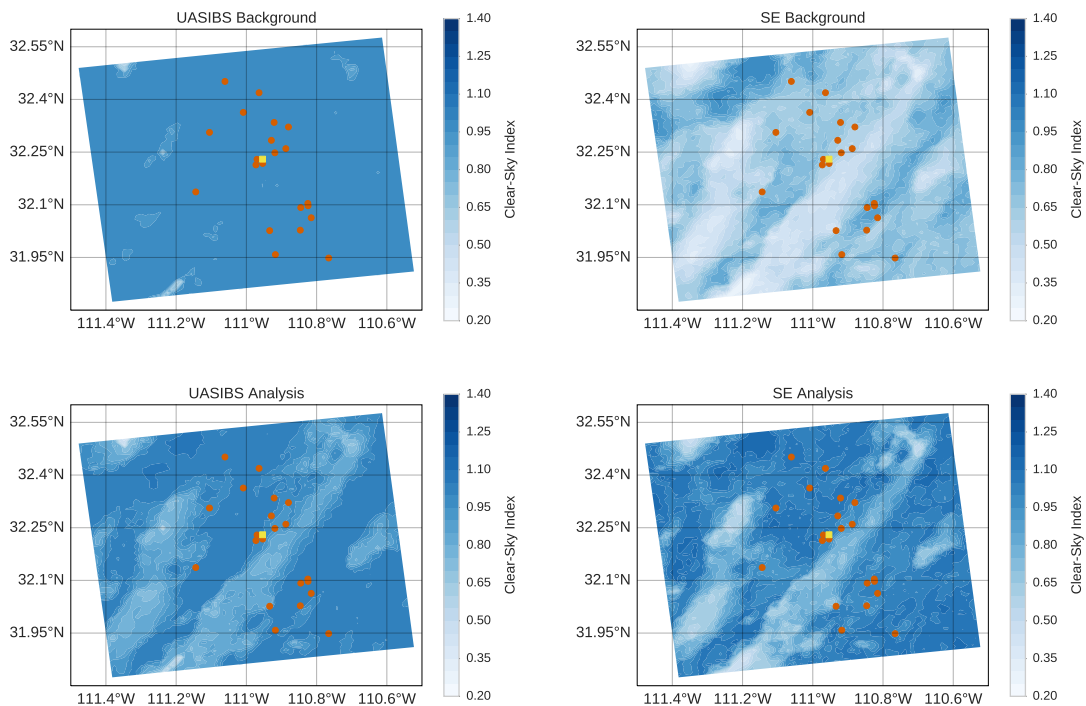


Figure 1.16: Example initial satellite estimate (known as the background) (top row) and analysis (bottom row) clear-sky index images using a physical (UASIBS, left column) and a semi-empirical (SE, right column) satellite image to ground irradiance models Note that in this case, UASIBS failed to produce many clouds. OI adds clouds to the analysis and also makes the darker, clear areas even more clear. In this case, the SE model overproduces clouds. OI reduces the cloud amount while keeping clouds in suitable locations.

CHAPTER 2

IRRADIANCE MONITORING NETWORK

Using historical data from 80 residential rooftop PV systems, Lonij *et al.* produced intra-hour solar power forecasts that showed skill over persistence forecasts [6]. The local electric utility, Tucson Electric Power (TEP), was interested in receiving these short-term forecasts in real-time. To generate real-time forecasts, data from sensors need to be gathered in real-time. Thus we set out building the irradiance monitoring network described in this chapter that would report values in near real-time. To accomplish this goal, we designed custom irradiance sensors that are deployed remotely and report data in real-time via cell model as described in Section 2.1. We also partnered with a local rooftop PV installer to gather power data from PV systems to act as proxies for irradiance, described in Section 2.2. This irradiance monitoring network, that was deployed in Tucson, AZ, is the basis for much of the forecasting work in this dissertation.

2.1 Design of Custom Sensors

This section describes the custom irradiance sensors that were developed to support the forecasting work in this dissertation. These sensors were custom designed based upon the lack of available, low-cost alternatives. The sensors as described cost around \$500 in raw materials when they were built in early 2014. This low cost allowed us to build and deploy many sensors to collect more data. The sensors were also designed to communicate data back in real-time so that the network could be used to produce operational forecasts for TEP.

2.1.1 Photodiode Sensor

A number of photodiodes were studied to determine a suitable, inexpensive replacement for a pyranometer to measure irradiance. We tested a clear domed photodiode which we sanded to better diffuse light, a thin sheet of Teflon glued on a photodiode to diffuse light, and a unmodified, flat photodiode, among others. We found that the flat photodiode (Osram BPW34) provided a reasonable signal level and cosine response, shown in Fig. 2.1. This photodiode is sufficient to detect deviations in the irradiance from clear-sky conditions, as a pyranometer would, which is the main way the network is used.

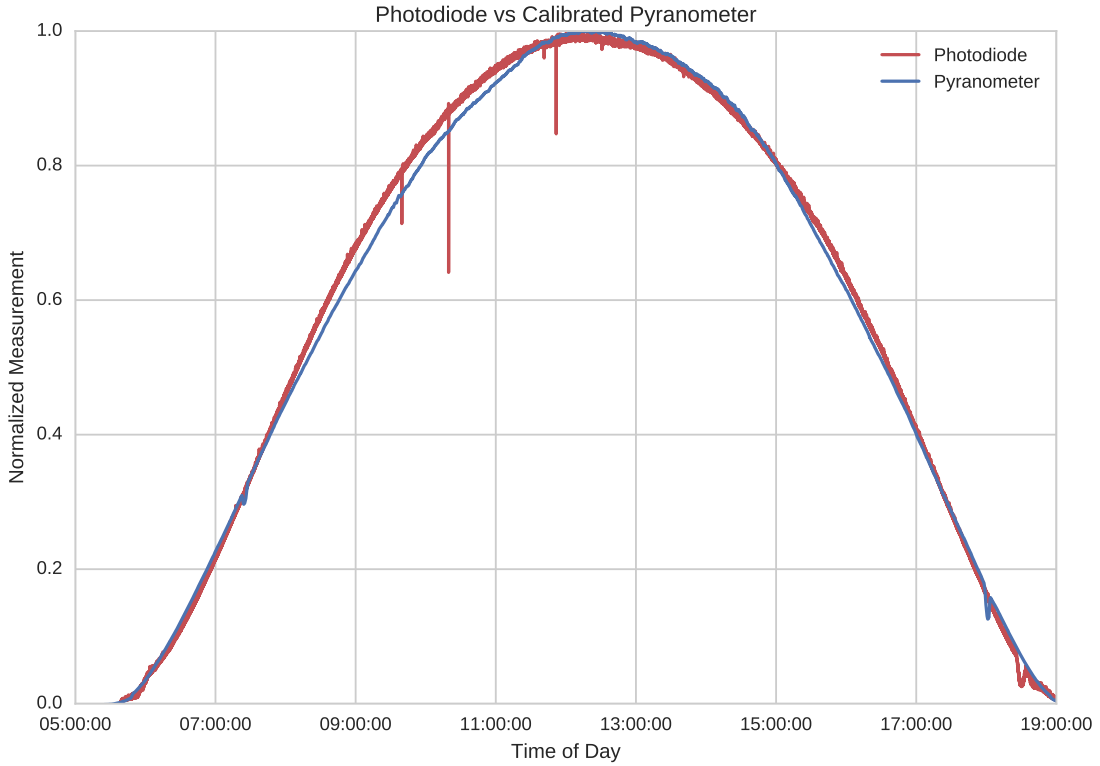


Figure 2.1: A comparison of the signal from a photodiode and a calibrated pyranometer. The photodiode does not exhibit a perfect cosine response with a wider peak that decays too quickly. However, the photodiode performs well for the main purpose of detecting changes in irradiance. Note that the noise in the measurement of the photodiode is about double the noise in the pyranometer measurement.

2.1.2 Hardware

A custom printed circuit board was designed for the components that store and send sensor data to a central server every minute. The circuit diagram for this board is shown in Fig. 2.2. Design files for the circuit board can be found online [7].

The custom sensors are developed around the Olimex iMX223-OLinuXino-MICRO board. The OLinuXino was chosen because it consumes little power ($< 1\text{W}$) and it runs a full Linux operating system which allows for development in any language that can be installed on Linux along with the usual suite of Linux tools (SSH, Bash, logs). It is also relatively inexpensive to purchase complete boards, and the plans are open-source if one desires to build the board themselves.

Data is communicated via GSM using a MULTITECH MTSMC-H5-U Socket-Modem. This modem accepts a standard SIM card that is registered with a cellular data provider. The modem is connected to the OLinuXino via USB. WvDial and PPPD are used to setup the connection to the modem and allow internet access.

Power to the system is provided by a 10W solar panel and a 6Ah lead-acid battery. A standard solar charge controller is used limit the current from the panel to the battery. The nominal 12V from the battery is routed to the circuit board with the OLinuXino and modem and converted to 5VDC with a circuit based on the LM2676 step-down regulator.

The sensor is designed to accept input from either a calibrated pyranometer (Apogee SP-212) or an inexpensive silicon photodiode (Osram BPW34) as discussed in Section 2.1.1. A trans-impedance amplifier (MCP602) with appropriate gain is used to convert the current from the photodiode into a measurable voltage.

The voltage from the sensor (or sensor + trans-impedance amplifier) is converted to a digital signal with the MCP3201 12-bit analog-to-digital converter (ADC). This digital signal is then read the OLinuXino at regular intervals from the GPIO pins. An additional 4 channel 12-bit ADC (MCP3204) is used to convert other values such as enclosure temperature (measured by an LM61) and battery voltage to be read on the OLinuXino GPIO pins for monitoring. A 4.096V voltage reference (MCP1541)

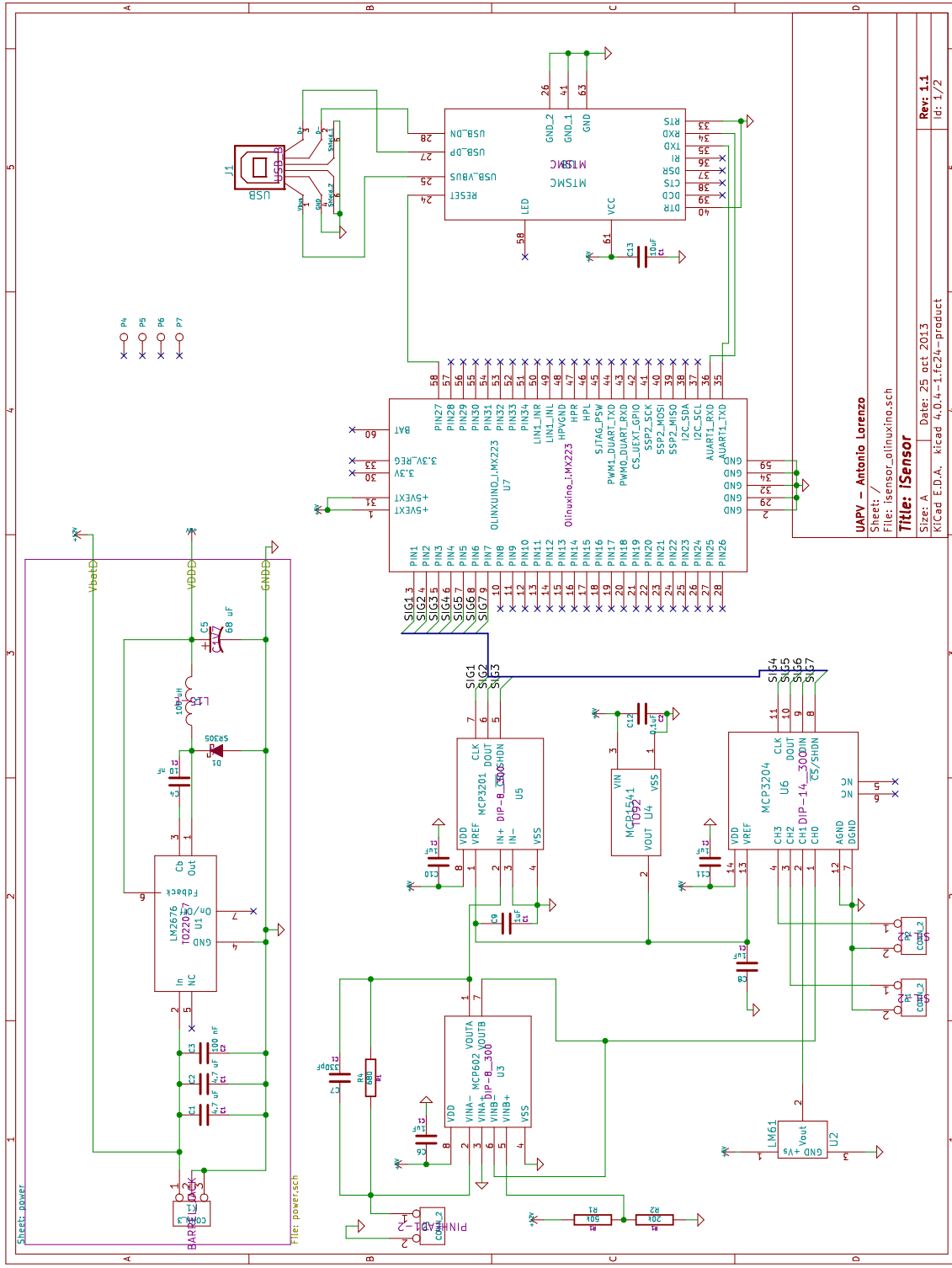


Figure 2.2: Circuit diagram for the custom, remote irradiance sensors. See Section 2.1.2 for a description of the components.

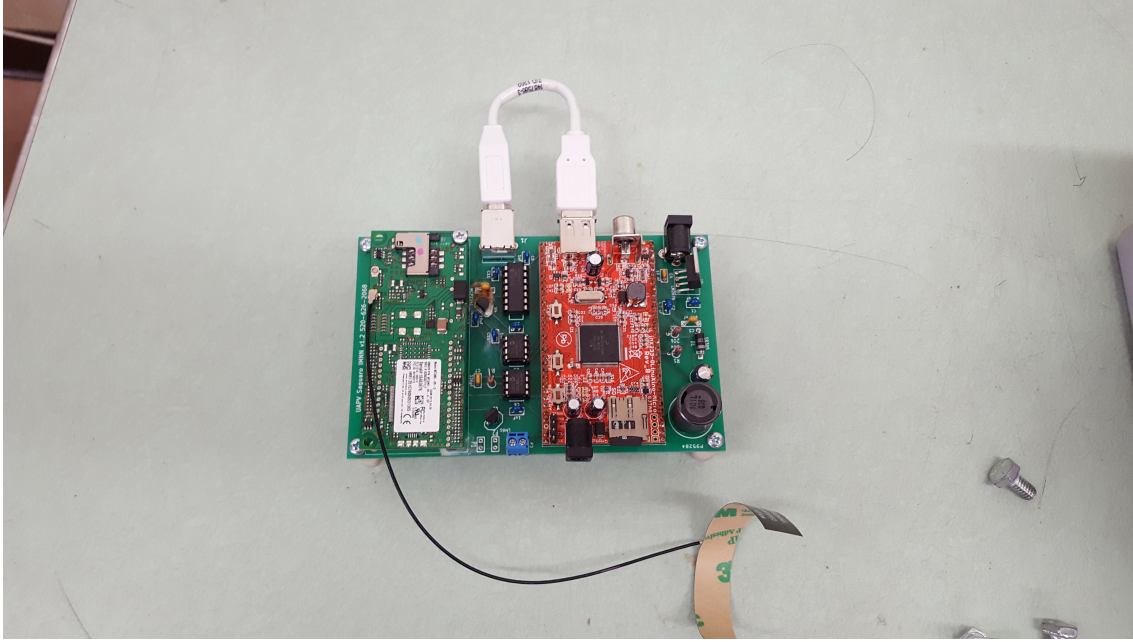


Figure 2.3: A fully assembled printed circuit board for a custom sensor. The red board is the OLInuXino and the green board on the left is the cell modem with a flexible antenna. Through hole components were chosen for easy soldering.

is used by both ADCs.

A fully assembled printed circuit board is shown in Fig. 2.3. The circuit board is housed in a waterproof box with an air snorkel and cable nipples to maintain water resistance. A metal extrusion serves as a mast to mount the photodiode or pyranometer. The solar panel and this mast are attached to the top of the waterproof box which can then be placed outside. A photo of the interior of the box with the circuit board and lead acid battery is shown in Fig. 2.4. An entire completed sensor undergoing testing is shown in Fig. 2.5.

2.1.3 Software

Here we document the approach we took to collect and send data from each sensor. We compiled a Linux kernel with options to take advantage of the GPIO and SPI capabilities of the OLInuXino board. With this kernel, we chose Arch Linux as the operating system and copied this base system onto an SD card with a unique system



Figure 2.4: A photo of the interior of the sensor enclosure. The air vent and waterproof cable nipples are visible on the right side of the box. The 6Ah 12V motorcycle battery is shown near the bottom.

identifier for each sensor. Upon first boot, the system checks with a centralized server to register itself.

Most scripts were written in Python which enabled fast prototyping. The main data collection script is started on boot and monitored via Supervisor to ensure it is restarted if it dies for some reason. This script pulls data from the connected ADCs at a configurable rate, time-stamps it, and stores it in files. This data is then uploaded to our central servers every minute where it can be imported into a database.

A separate script monitors the wireless connection to ensure the device maintains an internet connection. In addition to regularly sending the status of the battery and the board temperature for each sensor, each sensor also monitors a webpage that can instruct a sensor to connect to a central server via SSH and provide a reverse tunnel. This reverse tunnel allows us to remotely login to each sensor without knowledge of the sensor's IP address and avoiding firewall issues.

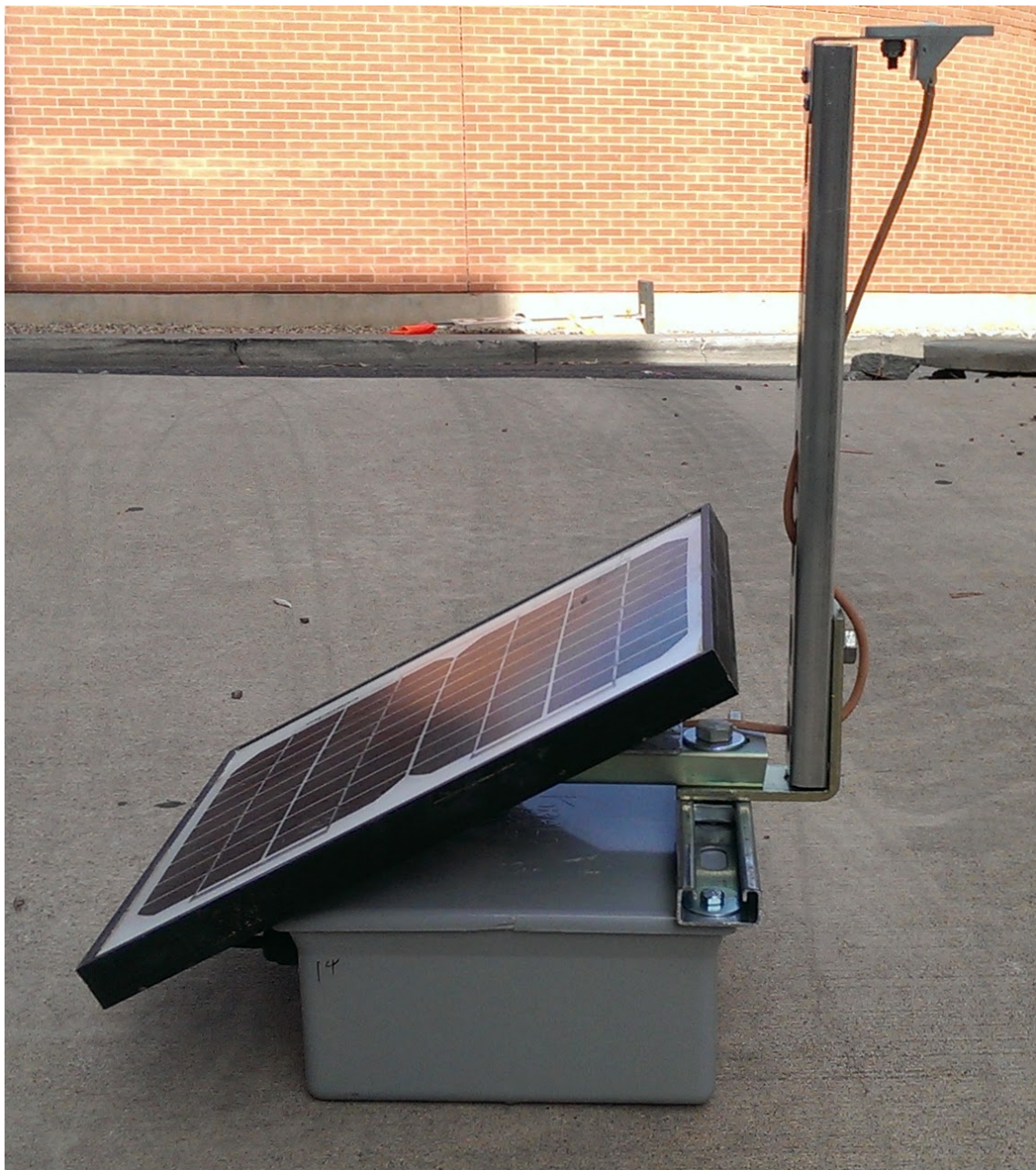


Figure 2.5: A photo of a complete custom irradiance sensor as it undergoes testing outside. The photodiode sensor can be seen mounted in the upper right of the image connected via a coax cable to the circuitry inside the box.

2.1.4 Possible Improvements

A number of improvements can be made to the sensor design presented in this section. First, most sensor failures were a result of the enclosure and mounting choice. Since the sensors were simply placed on the ground, they could be knocked over by animals, the cable to the sensor could be destroyed by rodents, or they could be flooded during the monsoon season. To mitigate issues like this, we recommend that sensors be mounted on a stake. While this would complicate deployment somewhat, it would likely prevent sensor failure due to orientation issues (where the solar panel is not in the sun to power the device) and some water damage.

In addition to a new enclosure and mounting design, a number of improvements in electronics have been made since the sensors were first developed. With the rise of the Internet of Things, there now exist numerous low-power computing devices that could replace the OLinuXino MICRO in our design. These new low-power devices now often come with an integrated lithium battery charge controller. Using lithium batteries instead of lead-acid will enable smaller, lighter sensors.

Finally, improvements can be made to the connection to a wireless network. A number of M2M devices have been released that enable wireless connectivity in low-power, integrated devices. For example, MULTITECH now manufactures a device that integrates a processor running Linux with the wireless network hardware. These devices may also include GPS receivers enabling precise location of sensor devices and more accurate time keeping.

2.2 Rooftop PV Systems as Sensors

One major challenge with using rooftop PV systems as sensors is that the data is often difficult to collect. One solution we employed is to use the built-in capabilities of some inverters to send data directly via FTP. With the help of a local PV system installer, Technicians for Sustainability, we are collecting 5 minute averaged power data from over 70 systems in the Tucson area in near real-time. Since many inverters connect to a home owners network, we also explored using cheap Linux devices

(Raspberry Pi) to communicate with inverters on the network and upload the data to a central server.

The electric utilities also have access to inverter data, although it may be delayed by days or weeks and aggregated to daily or longer values. With an increase in the installation of smart inverters, utilities are increasingly able to access inverter data in real-time. With an appropriate data transfer system in place, one can acquire the rooftop data from the utility, generate a forecast, and send the forecast back to the utility.

Since irradiance is the primary driver of PV output power, power data from rooftop PV systems can act as a proxy for irradiance. When analyzing both power and irradiance data, a units conversion is necessary. In our work, we choose to convert all irradiance proxy data to clear-sky index

$$k_n(t) = \frac{y_n(t)}{y_n^{clr}(t)} \quad (2.1)$$

where $y_n(t)$ is the measured time-series and $y_n^{clr}(t)$ the expected time-series for sensor n if the sky were clear. This approach accounts for differences in systems such as orientation, peak power, and shading. Furthermore, it detrends the diurnal cycle in the data. The clear-sky expectation should account for temperature and aerosol effects on a given sensor in some way to produce an unbiased clear-sky index.

2.3 Network Deployment

The locations of the sensors located in the Tucson, AZ, area are shown in Fig. 2.6. The blue circles denote the locations of rooftop PV systems that we receive data from as described in Section 2.2. The majority of these sensors are located in central and north Tucson where the majority of homes are located. We have no control over the placement of these sensors, but are grateful to Technicians for Sustainability for setting up the data transfer and to the homeowners that allow us to use the data. The time span that data is available depends on each individual system due to factors such as when it was installed and if the data transfer stopped for some

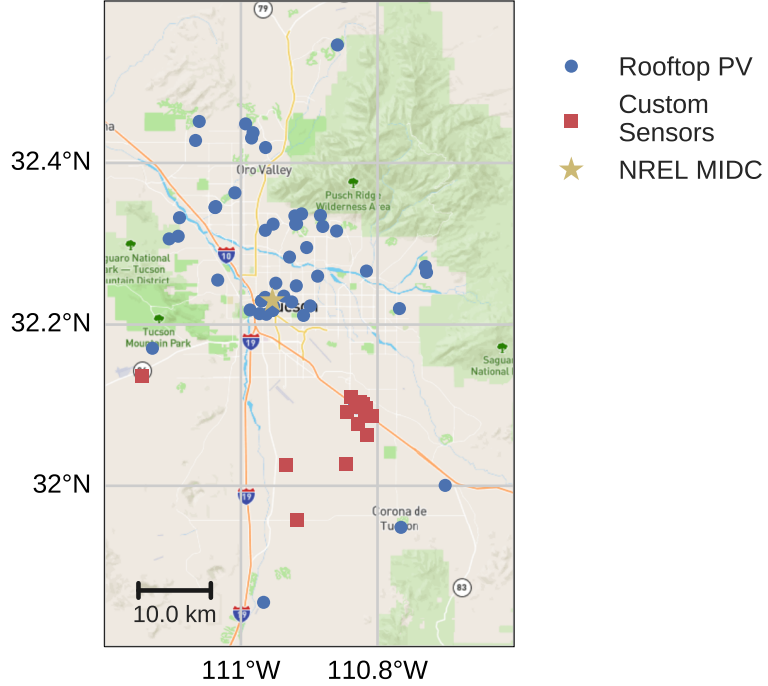


Figure 2.6: Map of Tucson, AZ, indicating the locations of custom and rooftop PV sensors. The NREL MIDC star refers to the calibrated and maintained irradiance sensor located at the University of Arizona.

reason.

The red squares denote the locations of the custom sensors described in Section 2.1. These sensors were placed south of Tucson where there is a lack of rooftop PV sensors. As described in Appendix A, the primary goal of this configuration was to study forecasts for a number of PV power plants located around 32.1° N and 110.8° W. The sensors are arranged as they are based on the analysis done in [6], the fact that the primary cloud direction in non-monsoon season is from the southwest, and the limited number of sensors available. The custom sensors shown in Fig. 2.6 were deployed in late March 2014. Data from these sensors is available from April to July 2014, when the sensors started failing due to monsoon rains and other causes mentioned in Section 2.1.4. A handful of sensors did survive for over two years before they died of unknown causes. While these sensors provided useful

information, the sensors, in their current form, are too time consuming to maintain beyond a proof of concept.

High-quality 10 second irradiance data has been continuously gathered from the National Renewable Energy Laboratory (NREL) MIDC OASIS sensor hosted at the University of Arizona. This suite of sensors (including GHI and DNI measurements) is part of the NREL Solar Resource & Meteorological Assessment Project (SOLRMAP) and is regularly maintained [8]. Data from this suite of sensors is publicly available at http://www.nrel.gov/midc/ua_oasis.

Data from select sensors in the network supporting [9, 10] is available online [11, 12].

CHAPTER 3

IRRADIANCE NETWORK FORECASTS

With data from the irradiance monitoring network described in Chapter 2, we studied a technique to produce forecasts for one minute to one hour in advance based on the work of [6]. We call this forecast technique a network forecast. Preliminary work on this is described in Appendix A and an in depth study of these types of forecasts is described in Appendix B.

The basic idea behind the network forecasts is that if a sensor records the irradiance at some point that sensor should have some predictive power of the irradiance for a sensor or PV power plant downstream. An illustration of this type of prediction is shown in Fig. 3.1 where the output of sensor 19 predicts the output of sensor 31 with an eight minute lead time.

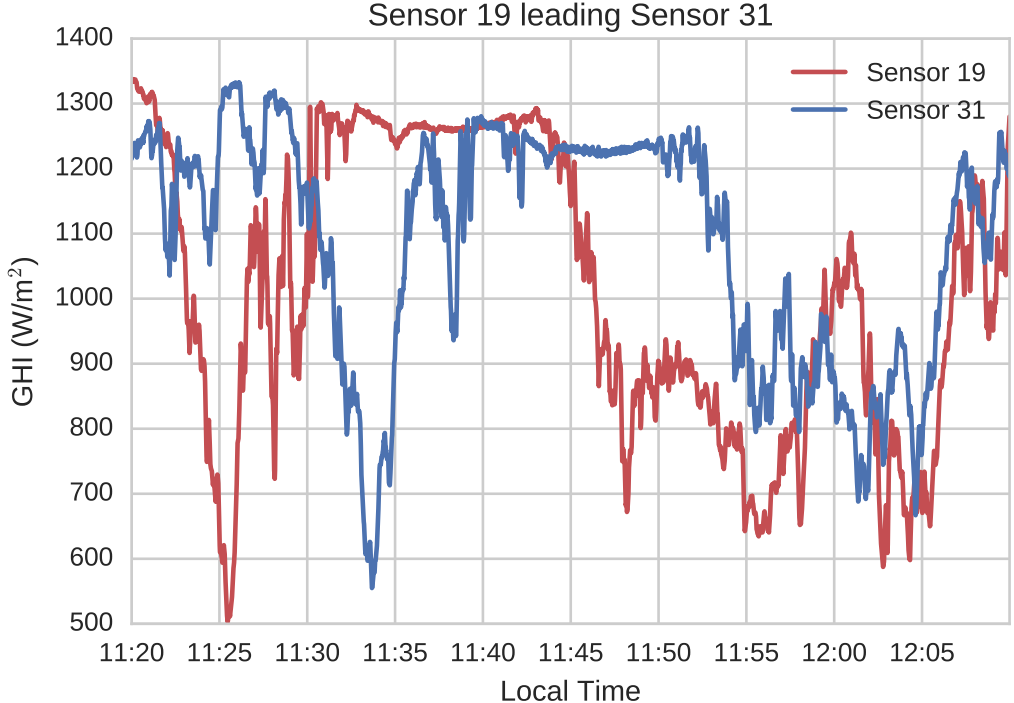


Figure 3.1: An example of the output of sensor 19 (red) predicting what the output of the upstream sensor 31 (blue) in roughly 8 minutes.

3.1 Irradiance Forecast Error Metrics

While studying and evaluating the forecasts described in Appendix B, we learned how important it is to understand forecast error metrics and their limitations. Here we present an examples of possibly misleading error metrics to warn those evaluating forecasts to be careful.

We will evaluate each metric on forecasts of clear-sky index to remove the time of day weighting that is implicit when computing errors for GHI. First, we will define the error metrics to be discussed. The most common metrics are mean bias error (MBE), mean absolute error (MAE), and root mean squared error (RMSE) that are defined as

$$\text{MBE} = \frac{1}{N} \sum_{i=0}^N (f_i - o_i), \quad (3.1)$$

$$\text{MAE} = \frac{1}{N} \sum_{i=0}^N |f_i - o_i|, \quad (3.2)$$

$$\text{RMSE} = \sqrt{\frac{1}{N} \sum_{i=0}^N (f_i - o_i)^2}, \quad (3.3)$$

where f_i is the forecast at time i and o_i is the observation of a sensor. MBE indicates the average bias of a forecast, and if it is not nearly zero, bias correction techniques may be applied to the forecast to reduce it further. MAE indicates the average magnitude of errors as does RMSE, but RMSE weights large errors more.

Other metrics include Pearson's correlation coefficient, the standard deviation of the errors, and the standard deviation of the forecasts as compared to the standard deviation of the observations. A number of other possible useful metrics are defined in [13]. We will also look at the ramp metrics defined in [14], the ramp detection index (RDI), false ramp index (FRI), and ramp magnitude forecast index (RMI).

3.1.1 Example Forecasts

Here we present forecasts for two days in Tucson, AZ, in 2014. The first day shown in Fig. 3.2 has thick but broken clouds. The second day shown in Fig. 3.3 has more scattered clouds. In each case, observations are averaged to five minutes, Forecast A is a five minute persistence forecast, Forecast B is a smoothing applied to the data, and Forecast C is a fraction of the clear-sky profile for that day.

Which forecast is best depends on how one plans to use the forecast. If one is concerned with quantities like average hourly production from a PV plant, perhaps the smoother Forecast B is best. If one is concerned with variability to, for example, schedule generation to back up solar power, Forecast A might be preferable. In most cases, Forecast A is considered the better forecast that better captures the nature of the observations.

Table 3.1 shows the values of some standard error metrics for forecasts on each day. For Day 1, Forecast A is clearly the best forecast with the lowest MAE and RMSE, and the highest correlation to the observations. It also performs better at

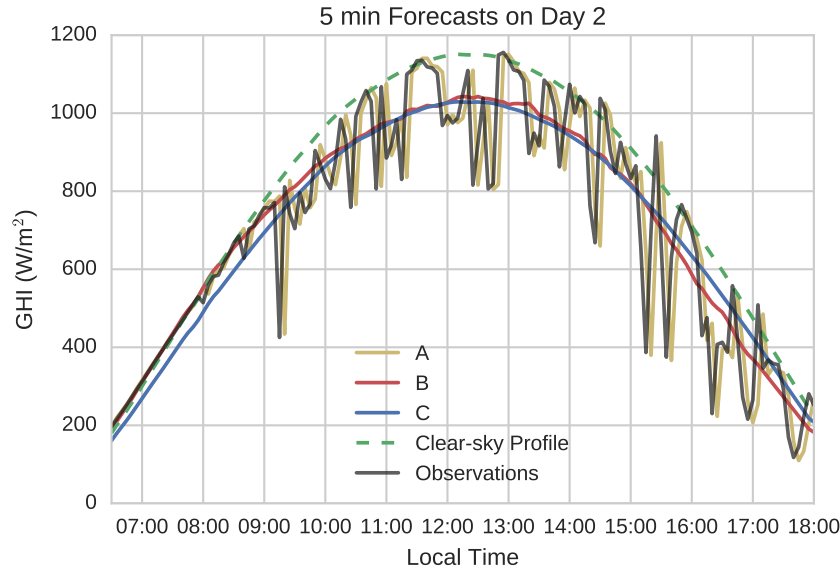
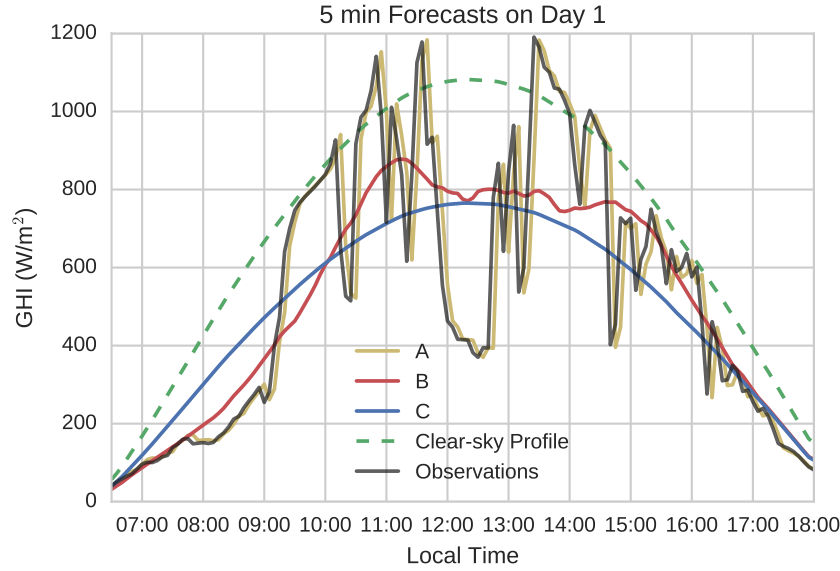


Figure 3.3: Five minute ahead forecasts for a day with scattered clouds. Forecast A is a persistence forecast that captures the variability of the observations, but offset by 5 minutes. Forecast B is a somewhat smoothed forecast, and Forecast C is simply a fraction of the clear-sky profile.

detecting ramp events. On Day 2, MAE and RMSE would suggest that Forecast B is the best. Furthermore, Forecast C has the same RMSE as Forecast A.

Table 3.1: Error metrics (in units of clear-sky index) for the forecasts on Day 1 shown in Fig. 3.2 and Day 2 shown in Fig. 3.3. Refer to the text of Section 3.1 for a description of each metric.

(a) Day 1			(b) Day 2			
	A	B	C	A	B	
MBE	0.00	-0.00	-0.00	0.00	0.02	0.01
MAE	0.09	0.16	0.22	0.10	0.09	0.12
RMSE	0.14	0.20	0.24	0.16	0.13	0.16
Correlation	0.85	0.60	NaN	0.49	0.53	NaN
Std. Dev.	0.24	0.13	0.00	0.15	0.07	0.00
RDI	0.80	0.51	0.57	0.62	0.55	0.50
FRI	0.25	0.59	0.88	0.28	0.23	0.37
RMI	0.42	0.29	0.22	0.21	0.26	0.19

If given Forecast B or C on Day 2, a user might consider it to be a forecast of a clear day, although with possibly more aerosols in the air reducing the irradiance slightly from the expected clear-sky profile. Forecast A is the only forecast to capture the variability that is also seen in the observations and is often most concerning to utilities. Thus, the metrics are somewhat misleading on Day 2.

3.1.2 Taylor Diagrams

The Taylor diagram is an excellent tool to summarize a number of metrics for many forecasts in a single figure [15]. Figures 3.4 and 3.5 are the Taylor diagrams for the forecasts on Day 1 and Day 2, respectively. For any forecast, the radius indicates the standard deviation of the forecast and the angle is the correlation of the forecast with the observations. The gray contours indicate lines of constant centered RMSE, or RMSE once any bias has been removed from the forecast. A perfect forecast would lie on the x-axis (correlation = 1) and have the same standard deviation as the observations.

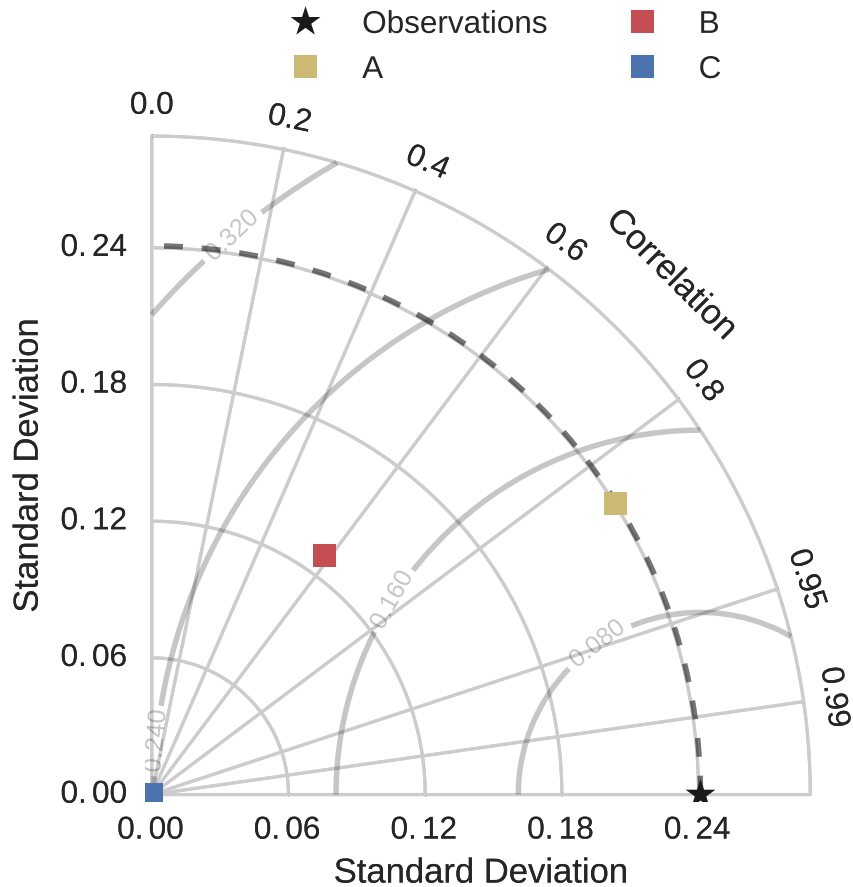


Figure 3.4: A Taylor diagram for the forecasts on Day 1 shown in Fig. 3.2. The light gray contours are lines of constant CRMSE. Forecast A has the lowest CRMSE in addition to having the same variability, as measured by the standard deviation, as the observations.

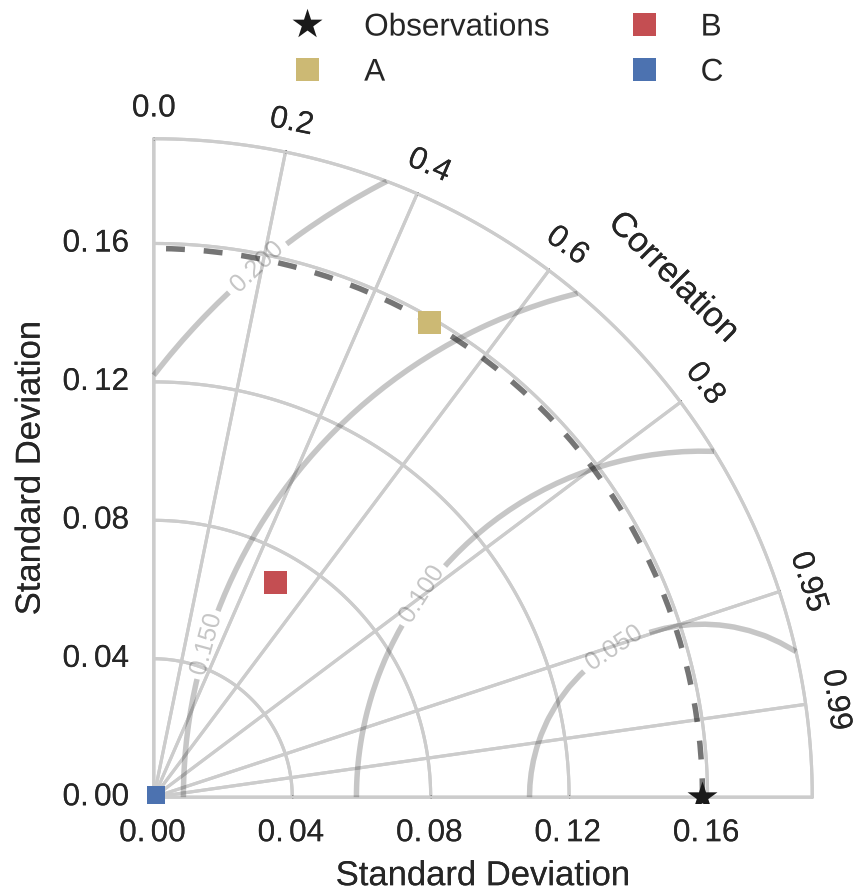


Figure 3.5: A Taylor diagram for the forecasts on Day 2 shown in Fig. 3.3. On this day, Forecast B has a smaller CRMSE and about the same correlation as Forecast A. However, Forecast A has similar variability to the observations as measured by the standard deviation. Depending on what the intended use of the forecast is, Forecast A may be the “better” forecast.

Figure 3.4 confirms our assessment that Forecast A is best on Day 1 since it has the lowest CRMSE, standard deviation equal to that of the observations, and the highest correlation to the observations. From Fig. 3.5, Forecast A is better than Forecast C since they have a similar CRMSE but Forecast A actually matches the variability observed in the observations. On the other hand, Forecast B has a lower CRMSE, but does not capture this variability. In this case, it depends on the use case to say whether Forecast A or Forecast B is best.

3.1.3 Suggestions

We have hopefully demonstrated why an understanding of the error metrics and careful application is important when evaluating forecasts. Evaluating forecasts on only a single or a couple of days may lead to conflicting results, so a longer time period with varied weather should be used when considering the overall performance of a forecast. Furthermore, a number of metrics should be calculated and compared to understand the differences in forecasts, and the Taylor diagram provides a good summary of some metrics. Finally, an examination of the actual forecast as compared to observations is useful to gain an intuitive sense of the forecast.

When comparing errors across studies, it is important to also consider the region that the forecast was made for. For example, the desert Southwest experiences fewer overcast days than locations in the Southeast. The Southwest also has a high number of clear days. A forecast with low errors in the Southeast may be better at forecasting overcast days with less skill on mostly clear days.

3.2 Future Work

One limitation to the network forecast methodology that we studied is that only a single velocity vector was used to transport the predicted clear-sky index map. Future work could explore using a number of vectors based on clouds at different heights and a proper advection scheme. One might also explore which domains this type of forecast performs best in order to switch between forecast methodologies for

different domains. Future work that may overcome the issue of clear-sky index maps generated in Appendix B not resembling reality by using satellite cloud estimates will be described in Chapter 5.

CHAPTER 4

OPTIMAL INTERPOLATION TO IMPROVE SATELLITE NOWCASTS WITH DATA

This chapter supplements the description of our work incorporating sensor network data with satellite irradiance estimates using optimal interpolation (OI) that is described in Appendix C and Appendix D. We describe the satellite image to ground irradiance algorithms we used for OI in more depth, show how the parameters for OI were chosen, and describe future work.

4.1 Satellite to Irradiance Algorithms for OI

In this section we will describe the satellite image to ground irradiance algorithms used in Appendix D and discuss other algorithms. One factor that affects how well OI performs for a given background image generated from some satellite to irradiance algorithm is the spatial resolution. OI as presented in Appendix D focuses on a relatively small, city scale area. This means that the background image must have sufficient density in this area for the deployed sensors to be of use in correcting the image. Furthermore, since our goal is to produce nowcasts, the algorithm should only rely on data present at the current time and take a reasonable amount of time to compute.

4.1.1 UASIBS Model

The University of Arizona Solar Irradiance Based on Satellite (UASIBS) model was developed at by Chang Ki Kim in 2015 [16]. This model relies on the infrared images of the GOES-W satellite to find completely overcast areas based on a comparison of the brightness temperature difference (difference between 10.7 and 3.9 μm images) to a reference calculated over the past few weeks. If the infrared channels do not

find an area to be overcast, the visible image is compared to a threshold image to determine if any of the 16 pixels in the $4\text{km} \times 4\text{km}$ box have a cloud. Once pixels are classified as cloudy or clear, a look-up table is employed to find the atmospheric transmittance and GHI on the ground for each pixel. A number of look-up tables are generated from using Goddard Space Flight Center Radiative Transfer Model: one for clear sky accounting for aerosols, one for high level clouds, one for mid level clouds, one for low clouds, and one for cumulus clouds.

The look-up table approach to calculate transmittance is limited. First, a number of climatological averages, specific to Tucson, are used in the calculations of the look-up tables including AOD and ozone. Instead, near real-time analysis and forecasts of AOD and ozone are available from Monitoring atmospheric composition and climate (MACC) project [17] and a ground truth measurement of AOD is available from the Tucson AERONET site [18]. Another limitation is that only ten values of the solar zenith angle are used which introduces artificial steps noticeable in the output GHI. With newer, fast radiative transfer codes, perhaps the look-up table approach can be replaced with a direct call to a radiative transfer code to avoid this issue.

The cloud detection methodology may also have issues when classifying clouds to use one of the look-up tables. This is illustrated in Fig. 4 of Appendix D reproduced in Fig. 4.1. There is a distinct lack of images with clear-sky index between 0.6 and 0.8 for UASIBS (blue \times s) that requires further investigation to determine if it is a problem with the look-up tables themselves or using the wrong look-up table. Removing the classification of cloud type and calculating the radiative transfer directly will likely solve this issue.

4.1.2 Semi-Empirical Model

The semi-empirical model used and described in Appendix D is based on what is commonly known as the SUNY model developed by Perez *et al.* [19]. This model was chosen because it is well known within the community and provides a good benchmark. The SUNY model was developed using ground truth sensors spread throughout the US with few in arid climates and no sensor in Arizona. Notably, Perez

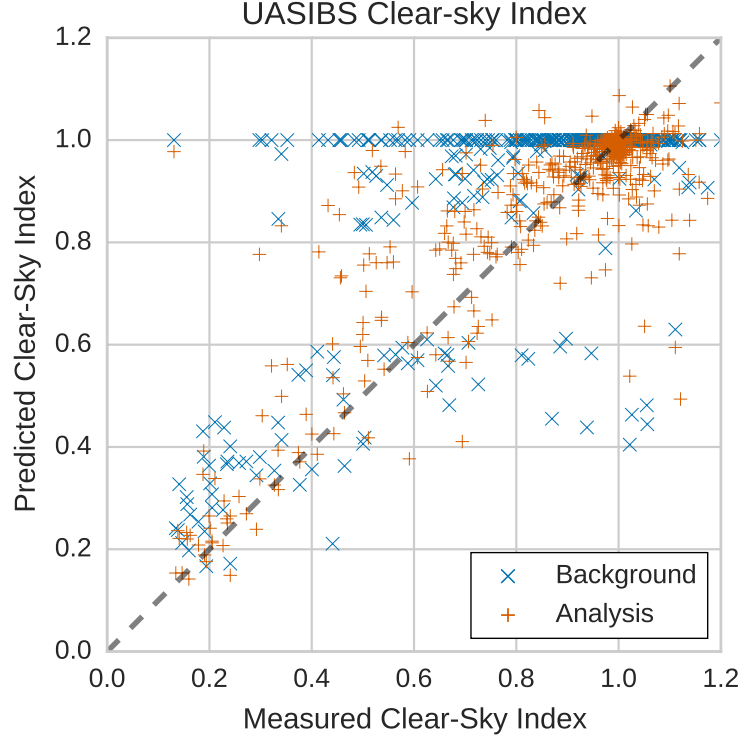


Figure 4.1: A scatterplot of the predicted vs measured clear-sky index for UASIBS before OI (blue) and after (orange). It is obvious there is some issue where UASIBS does not produce clear-sky indices between 0.6 and 0.8. OI helps correct this somewhat. (Reproduced from [10])

et al. recognized the deficiency in arid areas with high ground albedos and proposed a method to correct this issue [20]. The high ground albedo combined with the empirical coefficients developed for the US broadly likely lead to the overprediction of cloudy skies in Fig. 4.2.

A new, more strict test of OI in southern Arizona would be to recalculate the empirical coefficients used in the semi-empirical model for the area. This would likely improve the background errors of the semi-empirical errors and may also improve the final errors after performing OI.

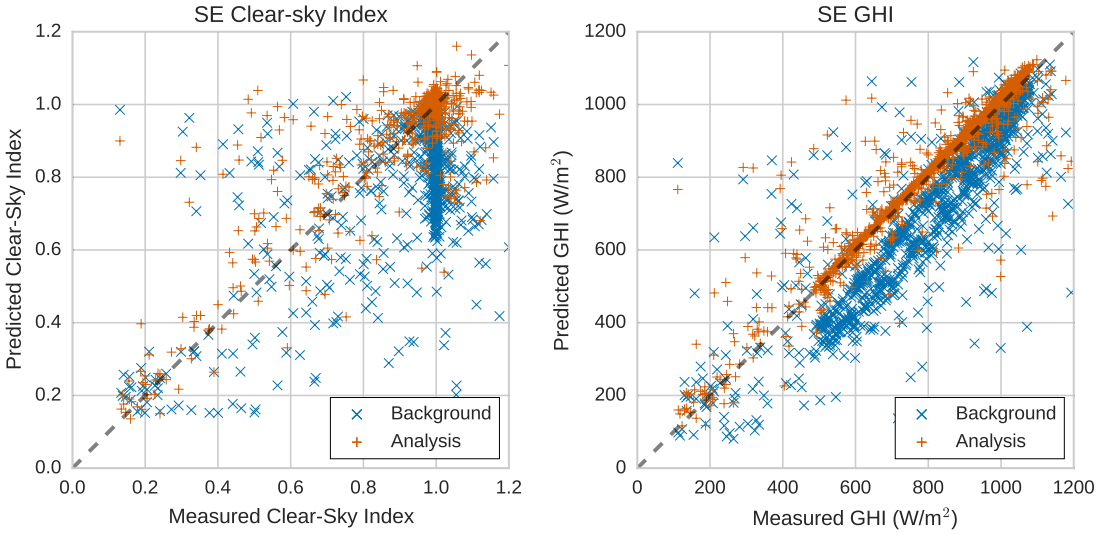


Figure 4.2: A scatterplot of the predicted vs measured clear-sky index for semi-empirical model before OI (blue) and after (orange). The semi-empirical model tends to overpredict clouds as shown in the clear-sky index scatterplot on the left. The splitting for the GHI in the right image is likely due to a time of day effect. (Reproduced from [10])

4.1.3 Other Models

There are numerous algorithms to convert satellite measured radiances to ground irradiance. A good overview of semi-empirical and physical methods can be found in [21, 22].

One publicly available dataset is the GOES Surface and Insolation Products (GSIP). GSIP provides hourly irradiance estimates at a resolution of 1/8 degree. OI is unlikely to perform well with this low spatial resolution ($\sim 14\text{km}$) where clouds are not well resolved and many sensors are contained in a single grid cell.

The National Renewable Energy Laboratory (NREL) is developing a new algorithm called the Physical Solar Model (PSM) that has been used to update the National Solar Radiation Database (NSRDB). NSRDB provides 30 minute 4km \times 4km data covering the US (and some other countries) from 1998 to 2015. One could explore how OI performs for an NSRDB background, but the low spatial resolution may prove limiting. Furthermore, the PSM algorithm is currently unpublished so it

cannot be used to make operational nowcasts which is the ultimate goal of OI.

4.2 Correlation Parameterization

Section 4 of Appendix D describes various correlation parameterizations we studied. The semi-empirical model is essentially a relationship between the cloudiness as measured by the satellite and the clearness observed on the ground. Therefore, one might expect that OI with the cloudiness correlation parameterization essentially modifies this cloudiness to clearness function. This is in fact the case as demonstrated in Figs. 4.3 and 4.4. These figures also show how the spatial and empirical correlation parameterizations tend to broaden the curve instead of changing it's shape.

An example of the same cloudiness to clearness graphs is shown in Fig. 4.5. The UASIBS algorithm is more complex and not a simple function fo the adjusted visible albedo, but each correlation parameterization changes this cloudiness to clearness mapping in a different way. Also note the undesirable “bullseye” like pattern in the spatial correlation analysis image that does not correspond with reality.

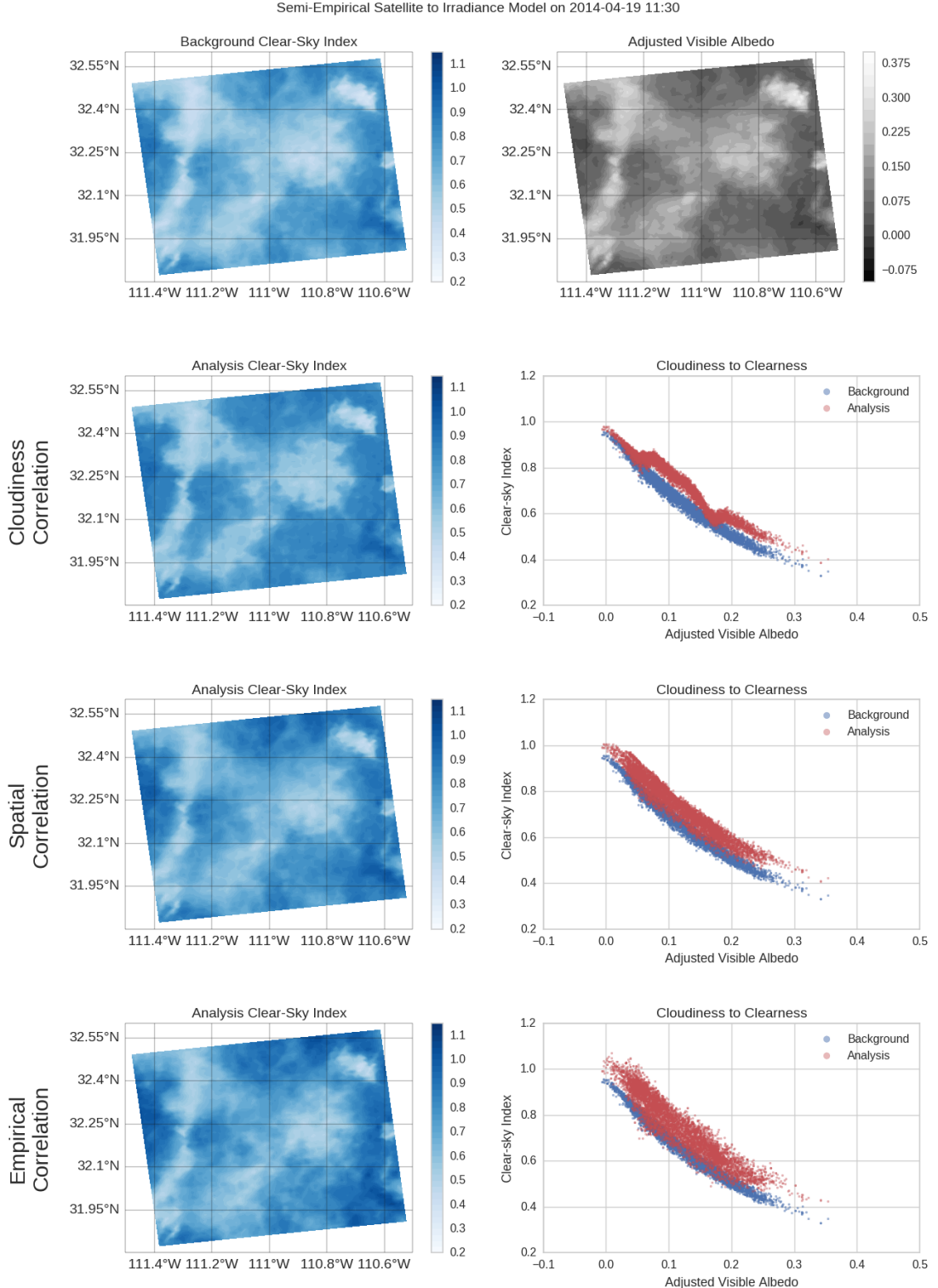


Figure 4.3: An example of the cloudiness (adjusted visible albedo) to clearness (clear-sky index) functions for the three correlation parameterizations for 2014-04-19 at 11:30 local time. Cloudiness correlation tends to reshape the curve whereas the other parameterizations broaden it.

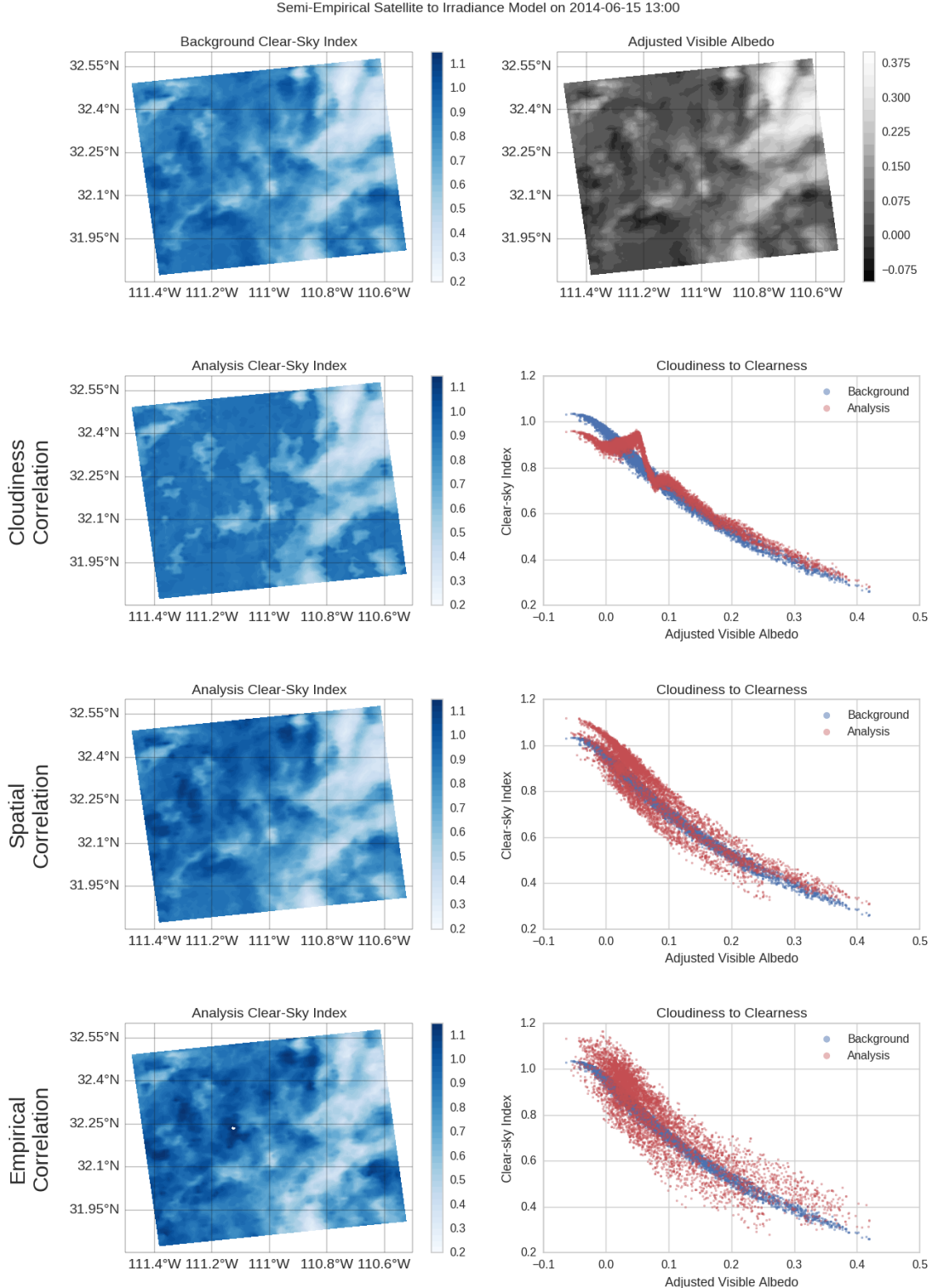


Figure 4.4: An example of the cloudiness (adjusted visible albedo) to clearness (clear-sky index) functions for the three correlation parameterizations for 2014-06-15 at 13:00 local time. Cloudiness correlation tends to reshape the curve whereas the other parameterizations broaden it.

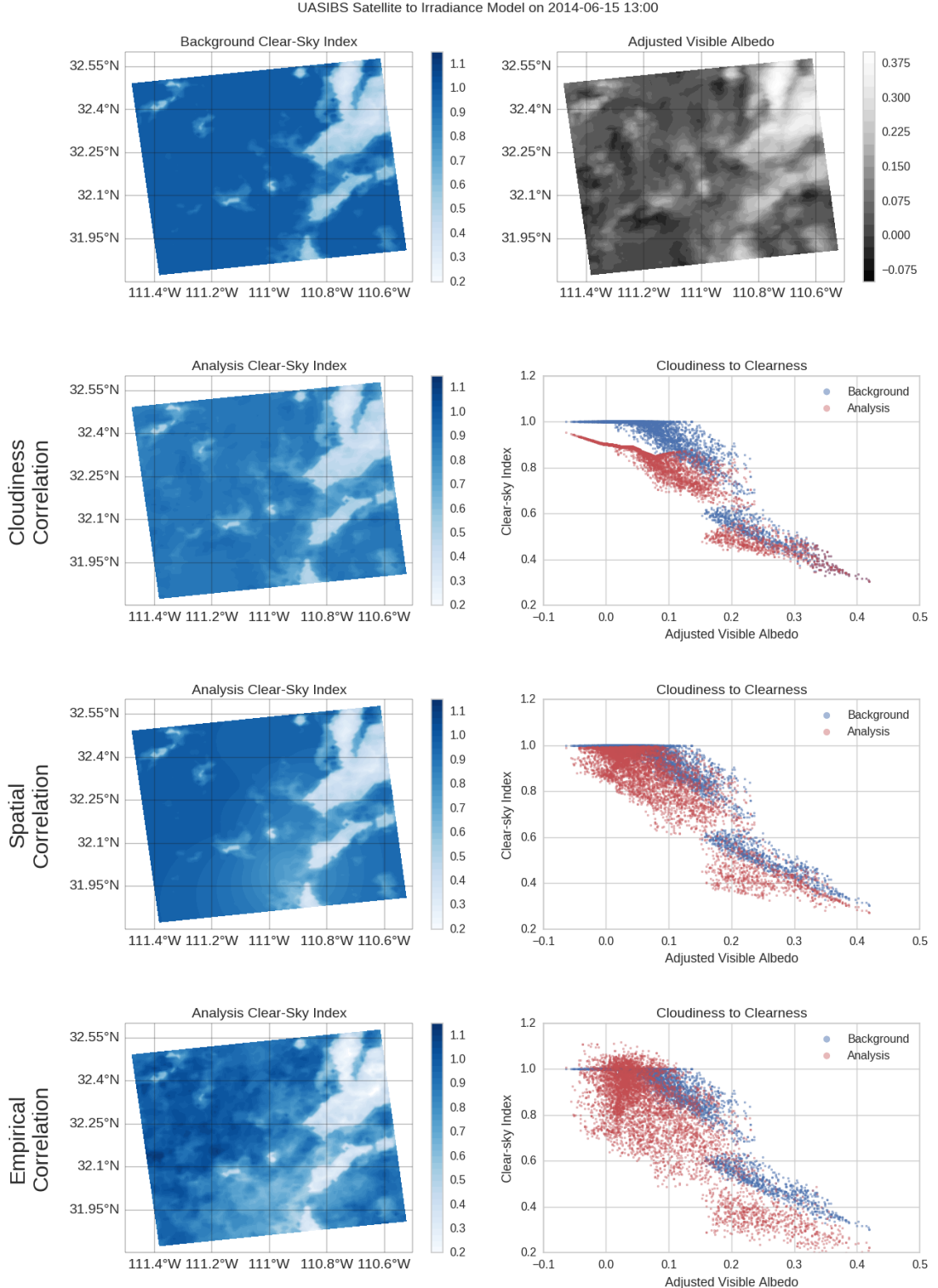


Figure 4.5: An example of the cloudiness (adjusted visible albedo) to clearness (clear-sky index) functions for the three correlation parameterizations for 2014-06-15 at 13:00 local time with the UASIBS model. Here the clear-sky index is not a relatively simple function of the adjusted visible albedo. However, the correlation parameterizations still adjust the cloudiness to clearness mapping in different ways.

4.3 Parameter Estimation

Section 6 of Appendix D discusses the tuning of OI for a specific location including the estimation of the parameters k, l, d by minimizing the mean-squared error (MSE) of the analysis over sensors withheld from OI. To perform this minimization a grid search over the parameters was performed and the resulting MSE for each set of parameters is shown in Fig. 4.6.

This figure clearly shows distinct minima in parameter space for the UASIBS satellite to irradiance model which indicates that OI is sensitive to the choice of parameters. On the other hand, the lack of distinct minima in parameter space for the semi-empirical model indicates that a wide range of parameters would give similar results after performing OI. If in the future the semi-empirical model is chosen as the background model for an OI based routine, a more thorough investigation into why OI is insensitive to these parameters is warranted.



Figure 4.6: Optimization surfaces for the parameters k , l , d of the optimal interpolation routine. The columns represent different choices of k , the rows distinguish between cloudiness and spatial correlation, the y-axis is l and the x-axis is $d^{1/2}$. The top figure shows surfaces for the UASIBS model and the bottom is for the semi-empirical model. Note, that for all choices of k and the correlation parameterization, the surfaces for the UASIBS model have a clear minimum. The surfaces for the semi-empirical model have less distinct minima indicating that optimal interpolation is not particularly sensitive to parameter choice for this model.

4.4 Image Position Errors

Section 5 of Appendix D describes how errors in the satellite image position relative to the ground sensors is corrected by minimizing the MSE of the OI analysis. These location errors primarily effect OI with the cloudiness correlation parameterization. This correction is not perfect and does not always work as intended. An example of a failure of this method for the semi-empirical model is shown in Fig. 4.7.

The cloudiness to clearness plots discussed in Section 4.2 may provide a method to detect when these location errors occur. The large positive slope in the cloudiness to clearness plot essentially indicates that a higher reflectivity as seen by the satellite indicates fewer clouds. This of course is highly unlikely and is an indication that the MSE location correction was insufficient. A better method to correct for position errors may take into account both the slope of the adjusted visible albedo to clear-sky index mapping and the MSE of the OI analysis.

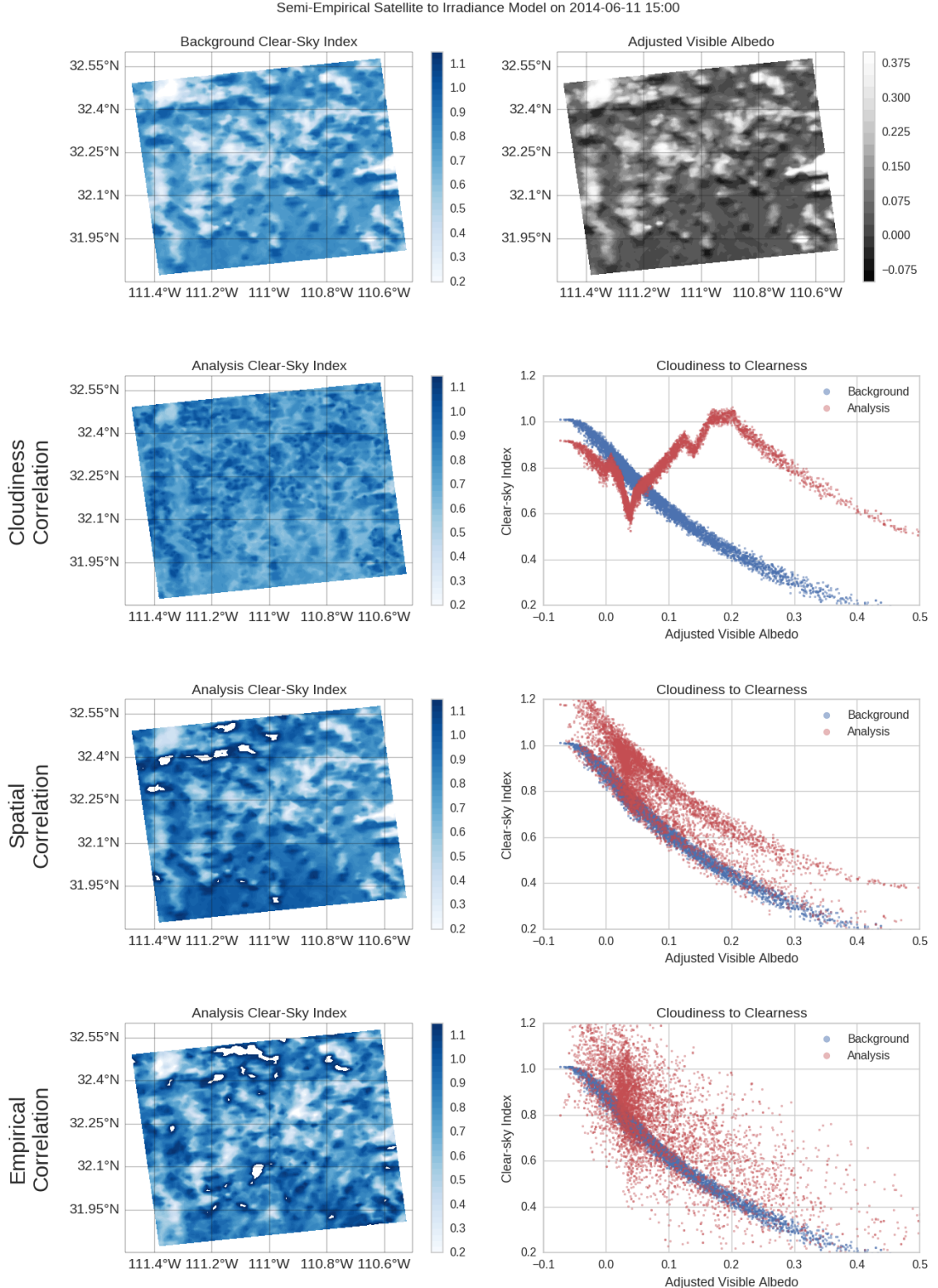


Figure 4.7: An example on 2014-06-11 at 15:00 where the geolocation correction for the cloudiness correlation parameterization and the semi-empirical model fails. The large, positive slope in the cloudiness to clearness graph is indicative of this failure since it does not make physical sense.

4.5 Future Work

Much can be done to extend the work in Appendix D. The first likely extension is to use these nowcasts of irradiance to produce a forecast as in Appendix B where the OI analysis replaces the interpolated map and is advected by some cloud wind. This can then be extended further with a better advection scheme and a more complex wind field.

One also could explore the valid range of OI, e.g. can information from sensors in Tucson be used to correct the background image over Phoenix 100 miles away? Perhaps other parameterizations will be necessary, such as a combination of cloudiness and spatial correlation, will be necessary for OI to perform well in this situation.

Another topic one could explore is distinguishing between cloud layers when performing OI. Say for example that sensor 1 is covered by a low cloud while sensor 2 is covered by a high cloud. It might be helpful to separate these layers so that sensor 1 provides information to correct the low clouds while sensor 2 provides information about the high clouds. In addition to possibly improving the OI result, knowledge of the cloud layers will also help with forecasting since each layer can and do move independently.

A natural extension of OI with a forecast is the Kalman filter. The Kalman filter would essentially perform OI, move the image according to some cloud advection scheme, and repeat with new data. Since the satellite takes a new image at least every 30 minutes, there are two sources of data that the update step should incorporate: the sensor data available every 5 minutes and the new satellite image every 30 minutes. A forecasting system using such a Kalman filter is described in Chapter 5.

CHAPTER 5

FUTURE WORK

5.1 Satellite Image Forecasts

Chapter 4 and Appendix D present a way in which a nowcast of irradiance can be improved using data assimilation techniques. Naturally, we want to extend this nowcast into a proper forecast initially using the technique of cloud motion vectors that produced forecasts in Chapter 3 and Appendix B. More complicated dynamics other than advection such as cloud formation and dissipation may be incorporated. Eventually, a full numerical weather model may be required to capture the dynamics of the system with the desired accuracy.

With a forecast model, it is natural to extend optimal interpolation to the well known Kalman filter where a forecast of the state is produced and constantly updated with new information. This has the added benefit of retaining information from all previous steps. Errors will be present in an estimation of the cloud velocity field, thus we will use an ensemble Kalman filter with an ensemble of velocity fields. An additional challenge will be integrating two types of observations into the state of the system: new observations from ground sensors and new satellite images.

In addition to introducing the forecast model and Kalman filter, we will also explore extending the area of analysis and the number of observations used. Figure 5.1 shows the locations of roughly 300 sensors that may provide useful information to this data assimilation problem. Some sensors such as the SURFRAD and NREL MIDC sites are regularly maintained, calibrated, and report high resolution data. Other sites such as those in the RAWs network provide hourly irradiance values and may lack routine maintainence.

With the launch of GOES-16 a number of groups are developing products and algorithms that make use of the new Advanced Baseline Imager (ABI) and will

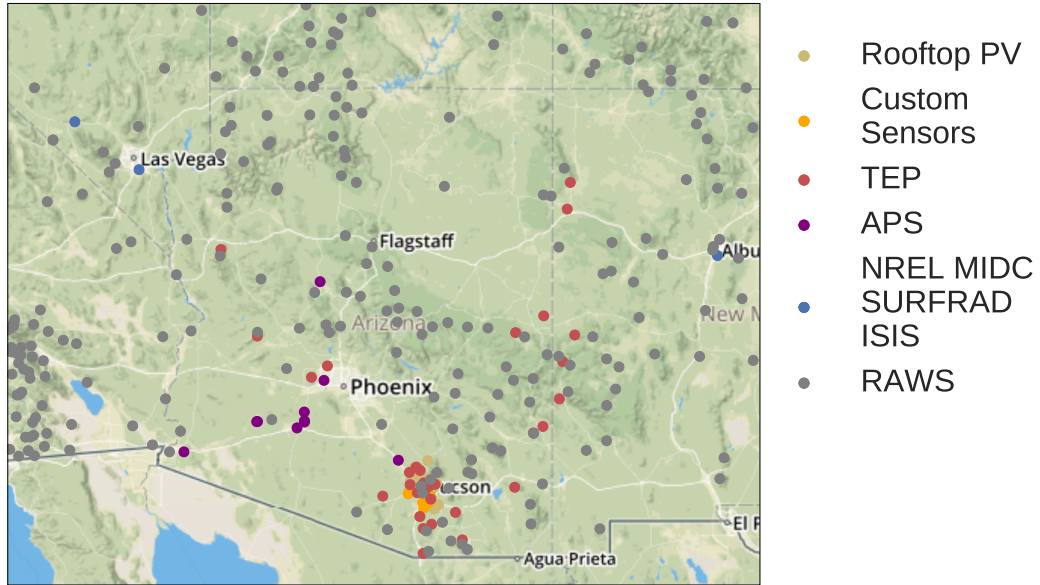


Figure 5.1: Map of all currently available irradiance sensors near Arizona. These sensors come from a number of networks with varying quality and time resolutions.

provide better background state estimates. The new ABI will image the continental US every five minutes with 16 spectral bands and resolutions as high as 0.5 km for the $0.64 \mu\text{m}$ visible band. Pictures of a comparison of the new GOES-16 and the current GOES-13 visible images in Fig. 5.2 and of a detailed image over California in Fig. 5.3 show the impressive capabilities of the instrument.

A forecast regenerated every 5 minutes for 5 minutes to 6 hours in advance covering a 300×300 km area over the state of Arizona with 0.5 km resolution satellite estimates and 300 sensors from a 50 member (or larger) ensemble is a computationally daunting task. Initial research into the local ensemble transform Kalman filter to reduce the computational demands is promising [23]. Still, producing these forecasts operationally will likely require use of a high performance computing cluster and specialized compute hardware such as GPUs or coprocessors.



Figure 5.2: A comparison of visible images created from the visible channels of the new GOES-16 satellite and the previous generation GOES-13. GOES-13 has only a single visible channel while GOES-16 has three. Image courtesy of NOAA.



Figure 5.3: A visible image of the western US from the new GOES-16 satellite. The improved resolution and spectral bands will improve satellite derived irradiance estimates compared to the current generation of satellite. Image courtesy of NOAA.

5.2 Cloud Data Assimilation in WRF

Forecasts produced by the Weather Research and Forecasting (WRF) numerical weather model at the University of Arizona tend to lack clouds. Given the large area coverage that satellite images provide, it is natural to consider assimilating clouds from satellite images into the WRF model. This is a nontrivial task because the model does not produce clouds directly and the errors in cloud properties derived from satellite images can be difficult to estimate. Previous work has had some success by comparing the WRF cloud fields and satellite imagery to modify the water vapor variable in WRF [24]. This is a good starting point for future work, but ideally other properties of the cloud such as the ice and water content, depth, etc. would be accounted for.

5.3 Ensemble WRF Forecasting

An ensemble of WRF forecasts, similar to the ensemble of satellite forecasts discussed in Section 5.1, may produce better forecasts by spanning more of the solution space. This is regularly done at operation forecasting centers. Currently, UA-WRF is run about six times a day with different initial conditions based on the 0Z, 6Z, and 12Z GFS and NAM forecasts. This produces a multi-physics, time-lagged ensemble. Additional ensemble members can be produced by varying the various parameterizations in the model such as the microphysics and planetary boundary layer schemes. This will require study of model performance differences with different schemes to ensure ensemble members have a resonable spread to avoid wasting computation on members that always produce the same forecast.

5.4 Intelligent Forecast Fusion

As mentioned in Chapter 1, one eventual goal is to combine different types of forecasts taking into account their relative accuracies at different time horizons into one unified forecast. This unified forecast would predict future vales from one minute in

the future out to seven days combining persistence, network, satellite, and numerical weather forecasts. The main challenges to acheiving this goal are deciding the time horizon where one forecast ends and another begins and ensuring the forecast is consistent over this transition.

One technique to produce this fused forecast is compute a weighted sum of all the forecasts where the weights are dependent on the forecast horizon. Then the challenge becomes choosing the weights. Ideally, these weights would be based on the errors in the forecasts at different time horizons. The errors can be calculated using a year of past data and forecasts, but the errors will vary depending on the weather and season. One way to account for this may be to establish categories such as clear days, days with high thin clouds, etc. and compute errors for each category. Then, one just determines the category for the day and applies the weights based on the category. In some sense, this is an analog method. Another option may be to use machine learning techniques to determine the weights between forecasts.

CHAPTER 6

SOFTWARE

- operational system - large part of work - list of scripts and what they do - design of file interface, nabu - speedy - operation -; research gets used

CHAPTER 7

CONCLUSIONS

7.1 Future Work

- blending horizons
 - wrf ensemble
 - probabilistic stuff
 - full dynamics of wrf + data assimilation covering all time horizons

REFERENCES

- [1] GTM Research/SEIA, “U.S. Solar Market Insight Q4 2016: Executive Summary,” GTM Research, SEIA, Tech. Rep., 2016. [Online]. Available: <https://www.greentechmedia.com/research/subscription/u.s.-solar-market-insight>
- [2] P. L. Joskow, “Comparing the Costs of Intermittent and Dispatchable Electricity Generating Technologies,” *American Economic Review*, vol. 101, no. 3, pp. 238–241, may 2011. [Online]. Available: <http://dx.doi.org/10.1257/aer.101.3.238>
- [3] J. Kleissl, Ed., *Solar Energy Forecasting and Resource Assessment*, 1st ed. Oxford: Elsevier, 2013. [Online]. Available: <http://dx.doi.org/10.1016/B978-0-12-397177-7.18001-5>
- [4] R. H. Inman, H. T. Pedro, and C. F. Coimbra, “Solar forecasting methods for renewable energy integration,” *Progress in Energy and Combustion Science*, vol. 39, no. 6, pp. 535–576, dec 2013. [Online]. Available: <http://dx.doi.org/10.1016/j.pecs.2013.06.002>
- [5] D. Cormode, “Large and Small Photovoltaic Powerplants,” PhD Dissertation, University of Arizona, 2015.
- [6] V. P. Lonij, A. E. Brooks, A. D. Cronin, M. Leuthold, and K. Koch, “Intra-hour forecasts of solar power production using measurements from a network of irradiance sensors,” *Solar Energy*, vol. 97, pp. 58–66, nov 2013. [Online]. Available: <http://dx.doi.org/10.1016/j.solener.2013.08.002>
- [7] A. T. Lorenzo, “alorenzo175/remote_irradiance_sensor_design: Proven Prototype,” 2017. [Online]. Available: <http://doi.org/10.5281/zenodo.290244>
- [8] S. Wilcox and A. Andreas, “Solar Resource & Meteorological Assessment Project (SOLRMAP): Observed Atmospheric and Solar Information System (OASIS); Tucson, Arizona (Data),” 2010. [Online]. Available: <http://dx.doi.org/10.7799/1052226>
- [9] A. T. Lorenzo, W. F. Holmgren, and A. D. Cronin, “Irradiance forecasts based on an irradiance monitoring network , cloud motion , and spatial averaging,” *Solar Energy*, vol. 122, pp. 1158–1169, 2015. [Online]. Available: <http://dx.doi.org/10.1016/j.solener.2015.10.038>

- [10] A. T. Lorenzo, M. Morzfeld, W. F. Holmgren, and A. D. Cronin, “Optimal interpolation of satellite and ground data for irradiance nowcasting at city scales,” *Solar Energy*, vol. 144, pp. 466–474, 2017. [Online]. Available: <http://dx.doi.org/10.1016/j.solener.2017.01.038>
- [11] A. T. Lorenzo, A. D. Cronin, and W. F. Holmgren, “Irradiance monitoring network data and wind motion vectors,” aug 2015. [Online]. Available: <http://zenodo.org/record/29070>
- [12] A. T. Lorenzo and A. D. Cronin, “Irradiance measurements, satellite images, and clear-sky expectations for Spring 2014 in Tucson, AZ.” 2016. [Online]. Available: <http://doi.org/10.5281/zenodo.166769>
- [13] J. Zhang, A. Florita, B.-M. Hodge, S. Lu, H. F. Hamann, V. Banunarayanan, and A. M. Brockway, “A suite of metrics for assessing the performance of solar power forecasting,” *Solar Energy*, vol. 111, pp. 157–175, jan 2015. [Online]. Available: <http://dx.doi.org/10.1016/j.solener.2014.10.016>
- [14] Y. Chu, H. T. C. Pedro, M. Li, and C. F. M. Coimbra, “Real-time forecasting of solar irradiance ramps with smart image processing,” *Solar Energy*, vol. 114, pp. 91–104, 2015. [Online]. Available: <http://dx.doi.org/10.1016/j.solener.2015.01.024>
- [15] K. E. Taylor, “Summarizing multiple aspects of model performance in a single diagram,” *Journal of Geophysical Research: Atmospheres*, vol. 106, no. D7, pp. 7183–7192, 2001. [Online]. Available: <http://dx.doi.org/10.1029/2000JD900719>
- [16] C. K. Kim, W. F. Holmgren, M. Stovern, and E. A. Betterton, “Toward Improved Solar Irradiance Forecasts: Derivation of Downwelling Surface Shortwave Radiation in Arizona from Satellite,” *Pure and Applied Geophysics*, 2016. [Online]. Available: <http://dx.doi.org/10.1007/s00024-016-1302-3>
- [17] J.-J. Morcrette, O. Boucher, L. Jones, D. Salmond, P. Bechtold, A. Beljaars, A. Benedetti, A. Bonet, J. W. Kaiser, M. Razinger, M. Schulz, S. Serrar, A. J. Simmons, M. Sofiev, M. Suttie, A. M. Tompkins, and A. Untch, “Aerosol analysis and forecast in the European Centre for Medium-Range Weather Forecasts Integrated Forecast System: Forward modeling,” *Journal of Geophysical Research*, vol. 114, no. D6, p. D06206, mar 2009. [Online]. Available: <http://doi.wiley.com/10.1029/2008JD011235>
- [18] B. Holben, T. Eck, I. Slutsker, D. Tanré, J. Buis, A. Setzer, E. Vermote, J. Reagan, Y. Kaufman, T. Nakajima, F. Lavenu, I. Jankowiak, and A. Smirnov, “AERONETA Federated Instrument Network and Data Archive for Aerosol

- Characterization," *Remote Sensing of Environment*, vol. 66, no. 1, pp. 1–16, 1998. [Online]. Available: [http://dx.doi.org/10.1016/S0034-4257\(98\)00031-5](http://dx.doi.org/10.1016/S0034-4257(98)00031-5)
- [19] R. Perez, P. Ineichen, K. Moore, M. Kmiecik, C. Chain, R. George, and F. Vignola, "A new operational model for satellite-derived irradiances: description and validation," *Solar Energy*, vol. 73, no. 5, pp. 307–317, 2002. [Online]. Available: [http://dx.doi.org/10.1016/S0038-092X\(02\)00122-6](http://dx.doi.org/10.1016/S0038-092X(02)00122-6)
- [20] R. Perez, P. Ineichen, M. Kmiecik, K. Moore, D. Renne, and R. George, "Producing satellite-derived irradiances in complex arid terrain," *Solar Energy*, vol. 77, no. 4, pp. 367–371, oct 2004. [Online]. Available: <http://www.sciencedirect.com/science/article/pii/S0038092X03004687>
- [21] R. Perez, T. Cebecauer, and M. Šúri, "Semi-Empirical Satellite Methods," in *Solar Energy Forecasting and Resource Assessment*, J. Kleissl, Ed. Elsevier, 2013, ch. 2, pp. 21–48. [Online]. Available: <http://www.sciencedirect.com/science/article/pii/B9780123971777000024>
- [22] S. D. Miller, A. K. Heidinger, and M. Sengupta, "Physically Based Satellite Methods," in *Solar Energy Forecasting and Resource Assessment*, J. Kleissl, Ed. Elsevier, 2013, ch. 3, pp. 49–79. [Online]. Available: <http://www.sciencedirect.com/science/article/pii/B9780123971777000036>
- [23] B. R. Hunt, E. J. Kostelich, and I. Szunyogh, "Efficient data assimilation for spatiotemporal chaos: A local ensemble transform Kalman filter," *Physica D: Nonlinear Phenomena*, vol. 230, no. 1-2, pp. 112–126, 2007.
- [24] P. Mathiesen, C. Collier, and J. Kleissl, "A high-resolution, cloud-assimilating numerical weather prediction model for solar irradiance forecasting," *Solar Energy*, vol. 92, pp. 47–61, jun 2013. [Online]. Available: <http://dx.doi.org/10.1016/j.solener.2013.02.018>

APPENDIX A

REPRINT: SHORT-TERM PV POWER FORECASTS BASED ON A
REAL-TIME IRRADIANCE MONITORING NETWORK

The following manuscript was published in the proceedings of the 2014 IEEE 40th Photovoltaic Specialist Conference (PVSC). Further background material is presented in Chapter 3 of this dissertation. The manuscript is reprinted with permission from IEEE. Copyright (2014) by IEEE. Original reference: A. T. Lorenzo, W. F. Holmgren, M. Leuthold, C. K. Kim, A. D. Cronin and E. A. Betterton, "Short-term PV power forecasts based on a real-time irradiance monitoring network," 2014 IEEE 40th Photovoltaic Specialist Conference (PVSC), Denver, CO, 2014, pp. 0075–0079.
doi: 10.1109/PVSC.2014.6925212

Short-Term PV Power Forecasts Based on a Real-Time Irradiance Monitoring Network

Antonio T. Lorenzo*, William F. Holmgren†, Michael Leuthold‡,
Chang Ki Kim‡, Alexander D. Cronin†, Eric A. Betterton‡

*College of Optical Sciences, University of Arizona, Tucson, AZ, United States

†Department of Physics, University of Arizona, Tucson, AZ, United States

‡Department of Atmospheric Sciences, University of Arizona, Tucson, AZ, United States

Abstract—We built an irradiance sensor network that we are now using to make operational, real-time, intra-hour forecasts of solar power at key locations. We developed reliable irradiance sensor hardware platforms to enable these sensor network forecasts. Using 19 of the 55 irradiance sensors we have throughout Tucson, we make retrospective forecasts of 26 days in April and evaluate their performance. We find that our network forecasts outperform a persistence model for 1 to 28 minute time horizons as measured by the root mean squared error. The sensor hardware, our network forecasting method, error statistics, and future improvements to our forecasts are discussed.

Index Terms—data analysis, forecasting, real-time systems, sensors, solar energy.

I. INTRODUCTION

The demand for high accuracy solar power forecasting services is increasing as electric utilities and independent service operators add more variable and potentially destabilizing solar power generation. Numerous forecasting methods are being actively developed including those based on artificial neural networks [1], total sky imagers [2]–[5], irradiance sensor networks [6], [7], satellite derived irradiance [8], numerical weather models [9], and hybrid methods [10]. Each method has an optimal forecasting horizon; often, total sky imagers and irradiance sensor network forecasts perform best for very short (5–30 minutes) time horizons, satellite forecasts perform best for short- to mid-term horizons (1–4 hours), and numerical weather models perform best for longer horizons (>4 hours). The optimal horizon for neural networks and hybrid methods varies.

In our 2013 study [6], we made retrospective forecasts using 15 minute data from rooftop PV systems that performed optimally for 45 minute time horizons. In this paper, we describe our *operational* forecasts that are made using an improved sensor network that reports in real-time. We evaluate forecasts from 26 days in April that were made retrospectively. Our network forecasts outperform a persistence forecast for 1 to 28 minute time horizons. We attribute differences in performance compared to our earlier study to the smaller network and finer (1 minute) time resolution of the real-time sensors used in the present study.

In Section II, we describe our irradiance monitoring network and the sensors we developed. Then, we explain our method to generate irradiance network forecasts in Section III. Error

statistics are presented in Section IV, and conclusions and future work are discussed in Section V.

II. IRRADIANCE MONITORING NETWORK

A major barrier to making irradiance network based PV power forecasts is obtaining irradiance data in near real-time with high spatial and temporal resolution. We currently have a network of 55 sensors throughout the Tucson region that we use to make operational network forecasts. In this concentrated study, we use a subset of 19 sensors near the University of Arizona Science and Technology Park (UASTP). Our sensors are made up of irradiance network nodes (INNs) that we developed, rooftop PV system power data direct from monitoring equipment, and utility-scale PV power data. We now describe the INN hardware we developed to make network forecasts, the central database where all irradiance data is stored, and the network used in this study.

A. Sensor Hardware

To make high-quality network forecasts, we need reliable sensor hardware that reports in nearly real-time. We chose to design our own hardware after researching existing solutions in the market and finding them unsuitable or too expensive. Our sensor hardware is relatively cheap, uses reliable Linux microcomputers, and requires minimal maintenance. Our current sensors are not meant to be accurate global irradiance sensors, although with careful mounting and a suitable pyranometer, they can be. A summary of the sensor hardware is presented in Table I.

TABLE I
SUMMARY OF IRRADIANCE NETWORK NODES

Model	Comms. Backend	Sensor Type	Processing Unit	Collection Period
Saguaro	Cellular data network	Pyranometer or photodiode	iMX233- OLinuXino- MICRO	1 second
Prickly Pear	Ethernet internet connection	Rooftop PV power mea- surement	Raspberry Pi	10 seconds
Yucca	Ethernet internet connection	Pyranometer or photodiode	Raspberry Pi	1 second



Fig. 1. Picture of the Saguaro INN. The solar panel that provides power to the unit and the sensor attached to the stalk are visible.

The Saguaro INN is designed to be placed in remote locations and communicate via cellular data networks. We use either a calibrated pyranometer (Apogee SP-212) or a cheap silicon photodiode (Osram BPW34) to monitor the irradiance at the location of the sensor. We use a trans-impedance amplifier to convert the current from the photodiode to a measurable voltage. Voltage data from the sensor is read every second from a program running on an Olimex iMX233-OLinuXino-MICRO via an analog to digital converter. This data is sent every minute via a cellular modem (Multi-Tech MTSMC-H5) to our central database. This hardware is co-located on a custom PCB along with a DC-DC switching power supply, a board temperature monitor, and a battery voltage monitor. A 10W solar panel, 6Ah, 12V lead acid battery, and solar charge controller provide power to the hardware that consumes less than 1W of power on average. A picture of the Saguaro INN is shown in Fig. 1.

The Prickly Pear and Yucca INNs both send data over the internet using a Raspberry Pi, but use different sensors. The Prickly Pear INN communicates over Ethernet to a rooftop PV system's monitoring hardware (e.g. SMA Sunny WebBox) to use PV power as a proxy for irradiance. The Yucca INN uses a pyranometer or photodiode, like the Saguaro INN, that is read via an Arduino FIO placed in the sun and transferred via XBee radio to the central unit.

All three INNs use the Arch Linux operating system with custom kernels. Most programs are written in Python. Data is time-stamped on each INN, and the INN clock is synced

via NTP. We currently use SFTP to transfer the data from the sensor to our central database every minute. In the future we will use the messaging service ZeroMQ to transfer data with lower latency. We can update the software remotely using Fabric, and we use SSH to remotely log-in to a sensor if needed. We also have scripts on the Saguaro INN that monitor the cellular data connection, the board temperature, and the battery voltage. The INNs only send data during the day (as calculated by ephemeris code for each day) to save power and network bandwidth.

B. Central Database

As soon as data is sent to our central server via SFTP or ZeroMQ, a script loads the raw data into a MySQL database. The data is identified by a sensor ID number, epoch time stamp, and measurement. We also keep a MySQL table to store metadata for each sensor including location, sensor type, etc., and a table to store battery charge levels and temperatures for Saguaro INNs.

C. Network Used in this Study

A map of the 19 sensors used in this focused study is shown in Fig. 2. Most of the sensors are Saguaro INNs, although some are 5-minute data from rooftop PV systems, and 2-second power data from utility-scale installations. Forecasts were analyzed for locations at the UASTP, shown in Fig. 2b. We use a higher density of sensors to the southwest of the UASTP because the primary wind direction is from the southwest.

III. SENSOR NETWORK FORECASTS

Here we describe how we generate our network forecasts, which is similar to our previous method described in [6]. First, we generate clear-sky expectations for each sensor using data from clear days. Operationally, these are generated weekly and checked visually. This data driven approach captures shading due to obstacles, orientation, and other system specific parameters. At each specified time step t (every 1 minute in this study), we calculate the clearness index for each sensor n as

$$K_n(t) = \frac{g_n(t)}{g_{n,clear}(t)} \quad (1)$$

where $g_n(t)$ is the measured data at time t and $g_{n,clear}(t)$ is the clear-sky expectation at time t . In this study, the measured data is the average of the data collected over the previous one minute. Once the clearness is calculated for each sensor, we use bi-variate interpolation to make an interpolated clearness map similar to Fig. 3. We set the boundary of this map using the average clearness of all sensors for the previous minute. We can also use satellite images or numerical weather models to set this boundary. Then, we forecast the clearness for a sensor or arbitrary location by propagating this clearness map using an assumed cloud motion vector. There are several ways we can estimate this cloud motion vectors, and we describe some methods we will explore in future work in Section V. Here, we use the hourly outputs of a custom, high-resolution Weather

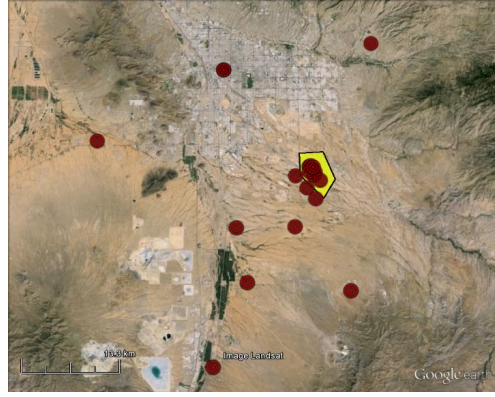


Fig. 2. Map of sensors used in this study throughout the Tucson area. A more detailed map of the UA Science and Technology Park (UASTP) highlighted in (a) is shown in (b).

Research and Forecasting (WRF) model that are produced earlier in the day to determine the cloud motion vector at each time t . To make this determination, we find the most likely cloud base height and then use the wind speed and direction at this height as the cloud motion vector. Finally, we calculate the quantity of interest (power or irradiance) with this forecasted clearness and the clear-sky expectation. We repeat this procedure for each forecast horizon.

For this study, we generated forecasts every minute, and the forecasts include predictions for GHI at a given location out to 30 minutes in advance. An example of a single forecast, showing predicted GHI for the next 30 minutes, is shown in Fig. 4. A full day of 10-minute ahead forecasts is shown in Fig. 5.

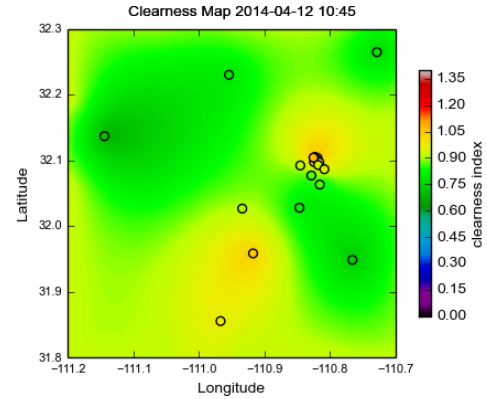


Fig. 3. Example interpolated clearness map.

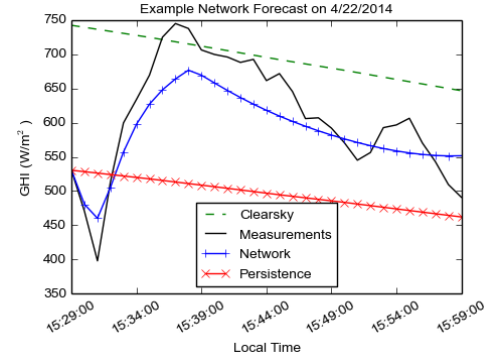


Fig. 4. Example forecasts made for a 30 minute period on 4/22/2014. The network forecast, clearness persistence forecast, clear-sky expectation, and measured data are shown. Forecasts shown are made at 15:29.

IV. ERROR STATISTICS

We now present error statistics for GHI forecasts made for 26 days in April. Of these days, 10 days had completely clear skies, 8 days were variable due to high, thin cirrus clouds, 2 days were overcast, and the remaining 6 days were highly variable, likely due to small cumulus clouds. Data used to calculate and evaluate the forecasts were binned into 1 minute averages. Forecasts were calculated and evaluated for each minute of the day for forecast horizons from 0 to 30 minutes. Forecast error metrics were calculated for each day and then averaged for the month. Only daylight hours were considered. In addition to evaluating our network forecasts, we also evaluate a clear-sky model and two persistence models: a clearness based persistence model that assumes the clearness

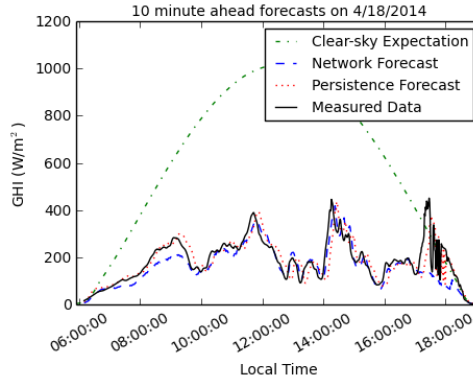


Fig. 5. Example 10 minute ahead forecasts made on 4/18/2014. The network forecast, clearness persistence forecast, clear-sky expectation, and measured data are shown. The forecasts for 10 minutes in the future are made every minute.

is constant and a measurement based persistence model that assumes the measured irradiance will be constant for the next 30 minutes. As expected, the measurement persistence model has larger errors than a clearness persistence model as forecast horizon increases because it does not account for the diurnal cycle. For comparison, the clear-sky forecast model simply assumes that any future irradiance will be the same as the clear-sky expectation. We also evaluated MAE and RMSE error statistics for WRF forecasts that are generated 2 to 20 hours in advance.

Table II and Figs. 6-7 present error statistics for a single irradiance sensor in the UASTP. The mean absolute error (MAE) and root mean squared error (RMSE) (using the standard definitions as found in [11]) at forecast horizons in multiples of 5 minutes are shown in Table II. A plot of MAE vs forecast time horizon is shown in Fig. 6 and a plot of RMSE vs forecast time horizon is shown in Fig. 7. The clearness persistence MAE and RMSE at the 0 minute forecast horizon is not identically zero because we limit the clearness to a maximum of 1.1 and errors in the clear-sky expectation in the early morning and late evening occasionally result in a calculated clearness in excess of this 1.1 limit. We then use this 1.1 clearness to calculate the expected irradiance, leading to small errors at zero time horizon. The network forecast is similarly affected by this clipping, but the larger error at the 0 minute horizon is mainly due to the interpolation we use to make clearness maps. Since this interpolation is smoothed for interpolation stability, the calculated clearness does not always match the measured clearness. Despite these errors, it is encouraging that our irradiance network based forecasts outperform the persistence model for the days studied for 1 to 28 minutes as measured by RMSE and 2 to 17 minutes as measured by MAE.

TABLE II
ERROR STATISTICS FOR 26 DAYS IN APRIL FOR PERSISTENCE AND NETWORK FORECASTS. BOLD FONT INDICATES WHEN THE NETWORK FORECAST OUTPERFORMS PERSISTENCE FORECASTS.

Forecast Horizon	Clearness Persistence	Network Forecast		
	MAE (W/m ²)	RMSE (W/m ²)	MAE (W/m ²)	RMSE (W/m ²)
0 min	0.166	1.23	3.26	11.3
5 min	30.4	58.6	27.6	48.1
10 min	38.7	69.1	36.6	60.0
15 min	43.6	74.8	43.0	67.9
20 min	47.7	79.0	50.0	74.7
25 min	50.6	81.3	54.1	78.6
30 min	52.9	83.2	60.1	85.4

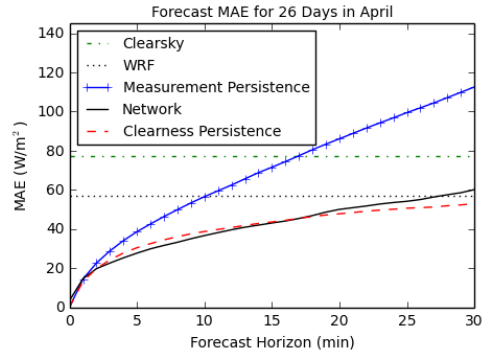


Fig. 6. Mean absolute error as a function of forecast horizon for a single sensor calculated each day and averaged over 26 days in April.

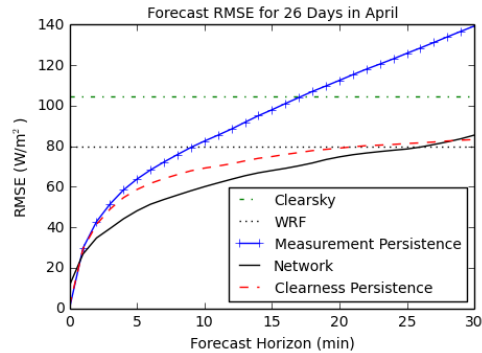


Fig. 7. Root mean squared error as a function of forecast horizon for a single sensor calculated each day and averaged over 26 days in April.

As mentioned above, we make operational forecasts of PV power. An example 10 minute ahead power forecast is shown in Fig. 8. The MAE for the 10 minute ahead network forecast on the day shown is 0.0908 MW or 2.7% of capacity, and the RMSE is 0.140 MW or 4.1% of capacity. We do not present more detailed error statistics of our power forecasts as we did for irradiance above because the data we currently have for the UASTP is so coarse, often with 5 minutes between measurements. For the purposes of forecast comparison, it is also more useful to compare irradiance forecasts to remove the extra step of converting irradiance to power.

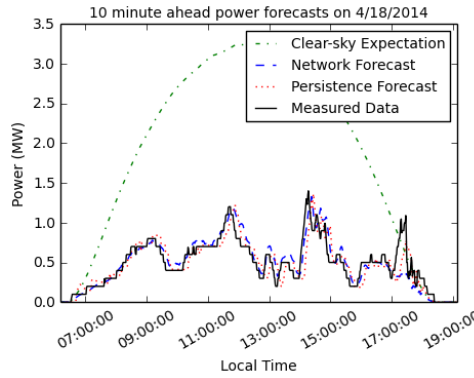


Fig. 8. Example 10 minute ahead power forecasts made on 4/18/2014. The network forecast, clearness persistence forecast, clear-sky expectation, and measured data are shown.

V. CONCLUSIONS

We designed and built low-cost irradiance sensors in order to make irradiance network forecasts. Using this network, we have been making operational forecasts since the beginning of 2014. A retrospective analysis for 26 days in April shows that our forecasts often perform better than a persistence model. When comparing forecasts, one must remember that our error statistics were calculated for irradiance and not clearness. This essentially weights our MAE and RMSE by the time of day. In the near future, we will re-evaluate our forecasts to make a more direct comparison with other work. We will also calculate numerous metrics that are described in [11] and [12] for further comparison with other techniques.

While our results of intra-hour forecasts with a network of irradiance sensors are encouraging, there are still many improvements to be made. We are satisfied with the operation of our custom INNs, but we need to deploy more throughout the Tucson region for higher quality forecasts that perform better at forecast horizons approaching one hour. There are also numerous improvements that we can explore for our forecasting algorithm including:

- 1) More accurate cloud motion vectors from ground sensor correlations, upper-air soundings, WRF forecasts, artificial neural networks, or some combination
- 2) Improved clearness map boundaries that incorporate satellite derived irradiance
- 3) Clearness map interpolation techniques that use previous measurements more wisely to fill in gaps.

We expect that these improvements will noticeably reduce our errors and extend the time horizons at which we can outperform persistence models.

REFERENCES

- [1] L. Ciabattoni, M. Grisostomi, G. Ippoliti, S. Longhi, and E. Mainardi, "Online tuned neural networks for PV plant production forecasting," in *Photovoltaic Specialists Conference (PVSC), 2012 38th IEEE*. IEEE, 2012, pp. 002916-002921. [Online]. Available: http://ieeexplore.ieee.org/xpls/abs_all.jsp?arnumber=6318197
- [2] C. W. Chow, B. Urquhart, M. Lave, A. Dominguez, J. Kleissl, J. Shields, and B. Washom, "Intra-hour forecasting with a total sky imager at the UC San Diego solar energy testbed," *Solar Energy*, vol. 85, no. 11, pp. 2881–2893, 2011. [Online]. Available: <http://www.sciencedirect.com/science/article/pii/S0038092X11002982>
- [3] R. Marquez and C. F. Coimbra, "Intra-hour DNI forecasting based on cloud tracking image analysis," *Solar Energy*, vol. 91, pp. 327–336, 2013. [Online]. Available: <http://www.sciencedirect.com/science/article/pii/S0038092X1200343X>
- [4] H. Yang, B. Kurtz, D. Nguyen, B. Urquhart, C. W. Chow, M. Ghonima, and J. Kleissl, "Solar irradiance forecasting using a ground-based sky imager developed at UC San Diego," *Solar Energy*, vol. 103, pp. 502–524, 2014. [Online]. Available: <http://www.sciencedirect.com/science/article/pii/S0038092X14001327>
- [5] S. Quesada-Ruiz, Y. Chu, J. Tovar-Pescador, H. Pedro, and C. Coimbra, "Cloud-tracking methodology for intra-hour DNI forecasting," *Solar Energy*, vol. 102, pp. 267–275, 2014. [Online]. Available: <http://www.sciencedirect.com/science/article/pii/S0038092X14000486>
- [6] V. Lonij, A. E. Brooks, A. D. Cronin, M. Leuthold, and K. Koch, "Intra-hour forecasts of solar power production using measurements from a network of irradiance sensors," *Solar Energy*, vol. 97, pp. 58–66, 2013. [Online]. Available: <http://www.sciencedirect.com/science/article/pii/S0038092X13003125>
- [7] D. Yang, Z. Dong, T. Reindl, P. Jirutitijaroen, and W. M. Walsh, "Solar irradiance forecasting using spatio-temporal empirical kriging and vector autoregressive models with parameter shrinkage," *Solar Energy*, vol. 103, pp. 550–562, 2014. [Online]. Available: <http://www.sciencedirect.com/science/article/pii/S0038092X14000425>
- [8] R. Perez, S. Kivalov, J. Schlemmer, K. Hemker Jr, D. Renné, and T. E. Hoff, "Validation of short and medium term operational solar radiation forecasts in the US," *Solar Energy*, vol. 84, no. 12, pp. 2161–2172, 2010. [Online]. Available: <http://www.sciencedirect.com/science/article/pii/S0038092X10002823>
- [9] P. Mathiesen and J. Kleissl, "Evaluation of numerical weather prediction for intra-day solar forecasting in the continental united states," *Solar Energy*, vol. 85, no. 5, pp. 967–977, 2011. [Online]. Available: <http://www.sciencedirect.com/science/article/pii/S0038092X11000570>
- [10] Y. Chu, H. T. Pedro, and C. F. Coimbra, "Hybrid intra-hour DNI forecasts with sky image processing enhanced by stochastic learning," *Solar Energy*, vol. 98, pp. 592–603, 2013. [Online]. Available: <http://www.sciencedirect.com/science/article/pii/S0038092X13004325>
- [11] J. Zhang, B.-M. Hodge, A. Florita, S. Lu, H. F. Hamann, and V. Banumarayanan, "Metrics for evaluating the accuracy of solar power forecasting," in *3rd International Workshop on Integration of Solar Power into Power Systems*, London, England, October 2013. [Online]. Available: <http://www.nrel.gov/docs/fy14osti/60142.pdf>
- [12] R. Marquez and C. F. Coimbra, "Proposed metric for evaluation of solar forecasting models," *Journal of Solar Energy Engineering*, vol. 135, no. 1, p. 011016, 2013. [Online]. Available: <http://solarenergyengineering.asmedigitalcollection.asme.org/article.aspx?articleid=1662255>

APPENDIX B

REPRINT: IRRADIANCE FORECASTS BASED ON AN IRRADIANCE
MONITORING NETWORK, CLOUD MOTION, AND SPATIAL AVERAGING

The following manuscript was published as a peer-reviewed article in Solar Energy. Further background material is presented in Chapter 3 of this dissertation. The manuscript is reprinted with permission from Elsevier. Copyright (2015) by Elsevier. Original reference: A. T. Lorenzo, W. F. Holmgren, and A. D. Cronin, "Irradiance forecasts based on an irradiance monitoring network, cloud motion, and spatial averaging," Sol. Energy, vol. 122, pp. 1158-1169, 2015. doi: 10.1016/j.solener.2015.10.038



Available online at www.sciencedirect.com

ScienceDirect

[Solar Energy 122 \(2015\) 1158–1169](http://Solar Energy 122 (2015) 1158–1169)

**SOLAR
ENERGY**

www.elsevier.com/locate/solener

Irradiance forecasts based on an irradiance monitoring network, cloud motion, and spatial averaging

Antonio T. Lorenzo ^{a,*}, William F. Holmgren ^b, Alexander D. Cronin ^{c,a}

^a University of Arizona, College of Optical Sciences, 1630 E. University Blvd., Tucson, AZ 85721, United States

^b University of Arizona, Department of Atmospheric Sciences, 1118 E. 4th Street, Tucson, AZ 85721, United States

^c University of Arizona, Department of Physics, 1118 E. 4th Street, Tucson, AZ 85721, United States

Received 2 July 2015; received in revised form 29 September 2015; accepted 10 October 2015

Communicated by: Associate Editor Jan Kleissl

Abstract

We describe and evaluate forecasts of solar irradiance using real-time measurements from a network of irradiance sensors. A forecast method using cloud motion vectors obtained from a numerical weather model shows significant skill over a standard persistence model for forecast horizons from 1 min to over 2 h, although the skill metric may be misleading. To explain this finding, we define and compare several different persistence methods, including persistence methods informed by an instantaneous spatial average of irradiance sensor output and persistence forecasts informed by a time-average of recent irradiance measurements. We show that spatial- or temporal-averaging reduces the forecast RMS errors primarily because these forecasts are smoother (have smaller variance). We use a Taylor diagram, which shows correlation, RMSE, and variance, to more accurately compare several different types of forecasts. Using this diagram, we show that forecasts using the network of sensors have meaningful skill up to 30 min time horizons after which the skill is primarily due to smoothing.

© 2015 Elsevier Ltd. All rights reserved.

Keywords: Solar forecasting; Solar irradiance; Sensor network

1. Introduction

The intermittency of solar power causes a cost to utilities and, ultimately, rate payers (Joskow, 2011). Solar power forecasts (Kleissl, 2013; Inman et al., 2013) may reduce these costs by enabling utilities to manage the variability of solar power in a number of ways. For example, forecasts can be used in conjunction with battery storage systems to control ramp-rates or provide frequency support (Hill et al., 2012; Cormode, 2015). Additionally, forecasts will provide utility grid operators with a prediction of

the expected photovoltaic (PV) output so they can more efficiently schedule backup generators.

A number of different techniques are used to forecast global horizontal irradiance (GHI). For forecast horizons in the intra-minute to a few minute range, techniques with input data from several ground sensors are often used (Achleitner et al., 2014; Elsinga and van Sark, 2014; Yang et al., 2015; Lipperheide et al., 2015).

For longer (intra-hour) forecast horizons, methods based on irradiance sensor networks (Lonij et al., 2013), machine learning techniques (Chu et al., 2015b), and sky imagers (Yang et al., 2014; Chu et al., 2015a) are being actively studied. Satellite image based forecasts are useful for 1-h to many hours in advance (Perez et al., 2010;

* Corresponding author.

E-mail address: atlorenzo@email.arizona.edu (A.T. Lorenzo).

Bilionis et al., 2014). For time horizons from several hours to up to a week in advance, numerical weather models often give the best predictions (Mathiesen and Kleissl, 2011; Diagne et al., 2014; Perez et al., 2013). Combinations of techniques are also being studied to extend the useful time horizon of a forecast (Marquez et al., 2013; Lauret et al., 2014).

Networks of irradiance sensors overcome some challenges typically associated with sky imagers or satellite images. For example, data from networks of irradiance sensors do not have the issue of converting pixel brightness to irradiance as sky imagers and satellite image methods have. Sky imagers and satellite images have the additional challenge of estimating cloud height to correctly project irradiance at cloud height to a location on the ground.

In this paper, we describe GHI forecasts that utilize a network of sensors placed throughout Tucson, AZ for April, May, and June 2014. The ideas behind this work are similar to those of Lonij et al. (2013), however the data sources and implementation are different. The rooftop PV network in Lonij et al. (2013) was limited to historical reports of 15 min average power, whereas the irradiance sensors used in the present research report 1 s resolution data with 1 min latency. This allows us to make higher resolution and, as we will see, more accurate forecasts.

We will show that our sensor network based forecasting method has significant skill when compared to a clear-sky index persistence forecast from 1 min to beyond 2 h time horizons. While the limited area and density of the network likely limits the skill and forecast horizon of our network-based forecasting method, the geographic diversity of measurements provide several advantages including improved persistence estimations. We will also explore why the forecasts exhibit such significant skill and explain this result is due to smoothing after 30 min forecast horizons.

First, we describe our network of irradiance sensors. Then, we describe how we use the network to make forecasts. A discussion of different types of persistence forecasts follows. Finally, we present and discuss our results and offer a concluding summary.

2. Irradiance sensor network forecasts

Our forecasting method relies on a network of sensors that sample the global horizontal irradiance at a number of locations. Our network consists of 12 irradiance sensors we developed, plus three rooftop PV power systems and one calibrated, commercial sensor. The calibrated sensor is part of a National Renewable Energy Laboratory (NREL) Solar Resource and Meteorological Assessment Project (SOLRMAP) site at the Univ. of Arizona (Wilcox and Andreas, 2010). Converting the data to clear-sky indices using an expected clear-sky profile for each sensor allows us to combine sensors that measure different quantities to make forecasts. These sensors are distributed throughout Tucson as shown in Fig. 1. The irradiance sensors we developed collect 1 s data and transmit

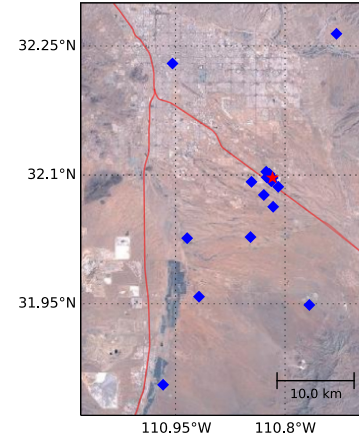


Fig. 1. Map of irradiance sensors used for this study in Tucson, AZ. The red star indicates the position of the sensor that was used to evaluate forecasts in Section 5. The sensor was chosen because of its proximity to 25 MW of installed PV power in and around the University of Arizona Science and Technology Park Solar Zone. The forecast area extends from 31.83° N to 32.28° N and 110.7° W to 111.15° W. (For interpretation of the references to color in this figure legend, the reader is referred to the web version of this article.)

it to a database every minute via cellular data networks (Lorenzo et al., 2014). Some use commercial pyranometers while others use photodiodes. Since we use clear-sky indices with data driven clear-sky profiles, the absolute error of the sensor is not a concern. However, the sensor used to evaluate the forecasted irradiance is a commercial sensor (Apogee SP-212) and agrees with the calibrated sensor to within 2% on average on clear days. The data were plotted for each day and for each sensor and verified by eye to provide some measure of quality control. See Lorenzo et al. (2015) for access to the dataset that was used in this study.

The first step in making our forecasts is to convert irradiance and PV power data to clear-sky index data. The clear-sky index for a sensor n at time t is defined as

$$k_n(t) = \frac{y_n(t)}{y_n^{clr}(t)}, \quad (1)$$

where $y_n(t)$ is the measured data and $y_n^{clr}(t)$ is the clear-sky expectation. Clear-sky expectations for each sensor are generated by fitting the measured data on a clear day in the recent past. An advantage of using this data-driven method of generating clear-sky expectations rather than a clear-sky model, such as the REST2 model (Guemard, 2008) or Ineichen model (Ineichen and Perez, 2002), is that the data-driven method inherently accounts for sensor orientation, permanent obstacles, and sensor calibration errors. Furthermore, because our forecasting method relies on forecasting clear-sky index and then converting back to

irradiance as a final step, the changes in atmospheric conditions between clear-sky days are not a major source of error in our final forecasts.

Next, we use the clear-sky indices to interpolate the scattered data onto a 1400 km^2 clear-sky index map for the Tucson region. To generate a clear-sky index map, we first create a 0.001° grid (with grid points approximately every 100 m) and add the sparse data from our network to the grid. We then set points along each boundary of the grid to the average of the clear-sky index values obtained from all the sensors. As we will see in Sections 4.4 and 5, this boundary condition helps to maintain forecast skill at longer time horizons.

Next, we fill all points in the grid with interpolated values as shown in Fig. 2. We chose to use multiquadric interpolation because it performs well at interpolating scattered geospatial data (Franke, 1982; Nuss and Titley, 1994), and it was more robust with our sparse data. We did not use a kriging method, even though kriging is often used to interpolate geospatial data, because we lack sufficient data to adequately estimate the variogram (Webster and Oliver, 1993; Sirayanone, 1988). We also explored inverse distance weighted interpolation, but found the output to be similar to multiquadric interpolation with insignificant differences in forecast errors (typically $<3 \text{ W/m}^2$ difference in the root mean square error for all forecast horizons).

Then, we translate this interpolated clear-sky map a distance determined by the cloud motion vectors (which may vary in time). The translation in the x direction, with the y translation being analogous, is given by

$$\Delta x(t_i, t) = \int_{t_i}^t v_x(t') dt', \quad (2)$$

where t_i is the time at which the forecast is being made, $t - t_i$ is the forecast horizon, and $v_x(t)$ is the x component of the time-varying cloud motion vector. Any grid points

that are missing data after the translation are filled with the average clear-sky index for all the sensors. Fig. 2 shows an example of an interpolated clear-sky index map and a map that has been shifted along the estimated cloud motion vector. Finally, we sample from this translated map at the desired forecast locations to obtain a forecasted clear-sky index which can be multiplied by the clear-sky expectation for that location to obtain an irradiance forecast. As we will discuss, for sufficiently long forecast horizons this procedure makes our network based forecasts indistinguishable from spatially-average persistence forecasts.

Forecasts out to 2 h in advance with 1 min time resolutions were made every 1 min for this analysis. As an example, one hour's worth of 5 min ahead forecasts along with measurements are shown in Fig. 3. This time-series is a composite showing snapshots (individual points) from 120 different forecasts that were each made 5 min in advance on a rolling basis. Concatenating points from different forecasts this way for several months lets us evaluate errors for forecasts with a 5 min horizon. Furthermore, updating forecasts every 1 min is valuable since 1 s data is constantly streaming into our database and each forecast has some new information that will likely improve the prediction for a specific time in the future. Later, we discuss errors as function of forecast horizon.

For estimating cloud motion velocity vector components (v_x, v_y), several techniques have been discussed including sensor correlations (Fung et al., 2014; Bosch et al., 2013), predictions from NWP (Lave and Kleissl, 2013; Lonij et al., 2013), analysis of aircraft communications addressing and reporting system (ACARS) or rawinsonde data, scaling of measured ground velocity, analysis of sky camera images (Urquhart et al., 2013), and analysis of satellite images (Hammer et al., 1999). For our analysis, we used modeled soundings (atmospheric temperature and

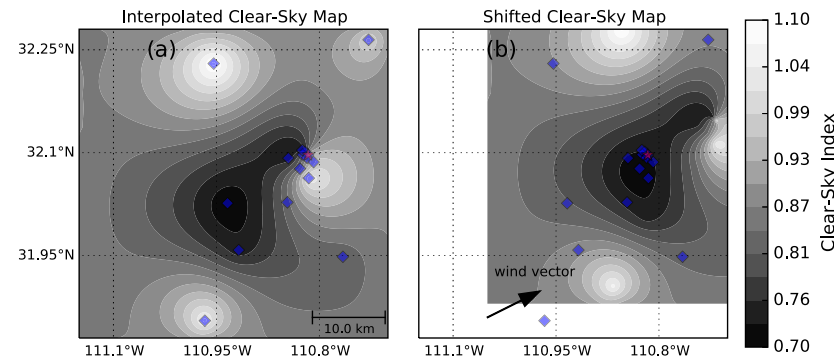


Fig. 2. An example interpolated map of clear-sky index on 5/19/14 near noon is shown in (a). Using the estimated cloud motion vectors this map is shifted according to desired forecast horizon as shown in (b). Then, samples from this shifted map are taken to as the forecasted clear-sky index for a particular location. The white space at bottom and left of (b) is filled in with the average clear-sky index of all sensors at the time the forecast is generated. The red star indicates the sensor that was used to evaluate forecasts. (For interpretation of the references to color in this figure legend, the reader is referred to the web version of this article.)

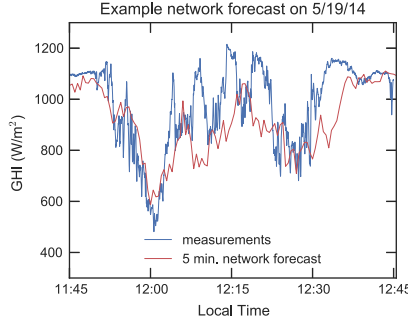


Fig. 3. An example of a 5 min ahead network forecast compared to measured data. Forecasts were generated every 1 min and the forecast for 5 min in the future is shown. The forecast and measurements at 12:00 show excellent agreement. For reference, the MAE for this entire period is 105 W/m^2 and the RMSE is 140 W/m^2 , and for 11:45 to 12:00 the MAE is 68 W/m^2 and the RMSE is 82 W/m^2 .

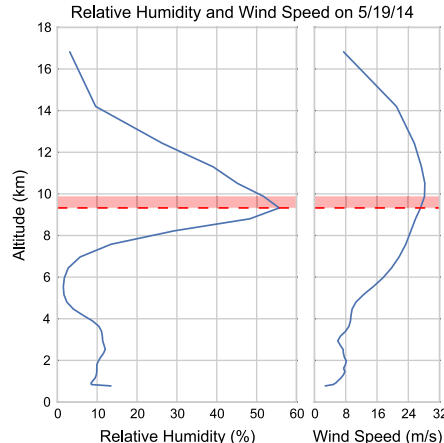


Fig. 4. Example vertical profiles of relative humidity and wind speed made by a numerical weather model on 5/19/14 at noon. To find the altitude at which clouds are most likely to form, we find the height with the greatest relative humidity (red dashed line). The winds at this height and heights within 90% of the maximum relative humidity (red shaded area) are averaged to produce an estimate of the cloud motion vector. (For interpretation of the references to color in this figure legend, the reader is referred to the web version of this article.)

dewpoint as a function of altitude/pressure) from the Weather Research and Forecasting (WRF) model run by the Univ. of Arizona, Dept. of Atmospheric Sciences (Leuthold, 2015). First, we compute a profile of relative humidity as a function of altitude averaged over the Tucson area from the WRF model. To estimate the cloud motion vectors, we find the altitude at which relative humidity is greatest (dashed line in Fig. 4), similar to Lave and Kleissl (2013). We then find all nearby heights

that have a relative humidity that is within 90% of the maximum (shaded area in Fig. 4). The wind speed and direction is then averaged for these altitudes and over the entire Tucson area to provide an estimated cloud motion vector. A new cloud motion vector is estimated in this way from each hourly output of the WRF model and then interpolated to 1 min time resolution. This simple estimation method has a number of limitations including only recognizing a single cloud layer and possibly selecting the wrong layer of the atmosphere i.e. one in which there are no clouds. This cloud motion estimation method along with the modest size and density of our network likely limits the overall accuracy of the network based forecasts presented here. Still, this network based method produces forecasts with lower errors than several standard persistence methods, as we discuss next.

3. Error metrics

We assessed the accuracy of forecasts using standard error metrics that are defined in Zhang et al. (2015). Each error metric is computed for forecast horizons, FH , ranging from 1 min to 30 min ($FH = 0, 1, \dots, 30$) by comparing forecasts, $y^{FH}(t_i)$, to subsequent instantaneous measurements, $y(t_i)$, of a single irradiance sensor. Errors were only computed when the solar zenith angle was less than 75° . Unless otherwise noted, only the 46 cloudy days in the study period were used to calculate error metrics and each metric is computed over this entire cloudy data set. Data and forecasts for a sensor (star in Fig. 1) in the middle of the network and near many large PV installations were used. Comparisons are always made with an instantaneous measurement, not averaged data, even when the forecast uses averaging.

In addition to root-mean squared error (RMSE) and mean absolute error (MAE), we also compute the centered root-mean squared error (CRMSE) for irradiance

$$\text{CRMSE}(FH) = \left(\frac{1}{N} \sum_{i=1}^N [(y^{FH}(t_i) - \bar{y}^{FH}) - (y(t_i) - \bar{y})]^2 \right)^{1/2}, \quad (3)$$

where an overbar indicates the sample mean of the quantity (Taylor, 2001). The CRMSE removes forecast bias and will become important later.

We also compute errors for forecasted clear-sky indices. This is valuable because, as opposed to irradiance, clear-sky index errors are not weighted based on the position of the sun in the sky.

We also define *relative* metrics in terms of clear-sky indices in order to present errors in percentages. The relative RMSE is

$$\text{rRMSE}(FH) = \bar{k}^{-1} \left(\frac{1}{N} \sum_{i=1}^N (k^{FH}(t_i) - k(t_i))^2 \right)^{1/2}. \quad (4)$$

Relative MAE is similarly defined as

$$\text{rMAE}(FH) = \bar{k}^{-1} \frac{1}{N} \sum_{i=1}^N |k^{FH}(t_i) - k(t_i)|. \quad (5)$$

Following the method of Marquez and Coimbra (2012), we can approximate forecast skill s as

$$s(FH) \approx 1 - \frac{\text{RMSE}(FH)}{\text{RMSE}_p(FH)}, \quad (6)$$

where RMSE_p is the RMSE for a clear-sky persistence forecast, described in Section 4.2. To estimate the average skill over many days, the ratio $\frac{\text{RMSE}}{\text{RMSE}_p}$ is estimated by the slope of the regression fit of daily RMSE vs RMSE_p . The average skill is then $\langle s \rangle = 1 - \text{slope}$. Examples of these plots and regressions are presented in Fig. 11.

4. Persistence forecasts

Persistence forecasts are the simplest type of forecast to implement and are often the most accurate at very short time horizons, making them a standard to compare with other methods. In this section we describe and compare the persistence forecasts we use for irradiance forecasting.

Before describing the various types of persistence, we first define the terminology we will use. The measured quantity of sensor n (e.g. irradiance) at time t will be denoted by $y_n(t)$. The forecast of sensor n at some time $t + FH$ in the future will be denoted by $y_n^*(t + FH)$. As mentioned in Section 3, we call FH the forecast horizon. The clear-sky expectation for a particular sensor will be denoted y_n^{clr} and the value of the clear-sky expectation at time t is $y_n^{clr}(t)$.

4.1. Measurement persistence

We call one of the simplest persistence methods “measurement persistence.” A measurement persistence forecast simply assumes that the irradiance at a future time will be the same as it is at the current time. Measurement persistence is defined by

$$y_n^*(t + FH) = y_n(t). \quad (7)$$

This type of persistence is useful for short time horizons, but it does not account for the diurnal cycle of irradiance due to changing solar position and this leads to large errors at longer time horizons as shown in Fig. 5.

4.2. Clear-sky index persistence

In this method, the clear-sky index is calculated at the current time and persisted into the future. A forecast of irradiance is obtained by multiplying this clear-sky index by the value of the clear-sky expectation at the forecast time. The equation for clear-sky index persistence is

$$y_n^*(t + FH) = \frac{y_n^{clr}(t + FH)}{y_n^{clr}(t)} \times y_n(t). \quad (8)$$

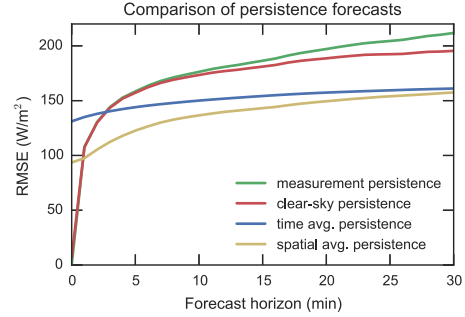


Fig. 5. Comparison of different types of persistence forecasts. RMSE, plotted as a function of forecast horizons, was computed for each type of forecast using data from the 46 cloudy days as described in Section 3. Spatially-averaged persistence has the lowest RMSE for all but the very shortest forecast horizons.

This method performs better than measurement persistence because it takes into account the diurnal cycle of irradiance, but it does require that a clear-sky expectation for the sensor, $y_n^{clr}(t)$, be known or modeled appropriately.

4.3. Time-averaged persistence

At time horizons greater than a few minutes, it can be beneficial to first average the measured clear-sky index over some time period defined by N time steps, each with period Δt , ending at some past time t_0 . This average clear-sky index is then multiplied by the clear-sky expectation of the target sensor to compute a forecast. Time-averaged persistence is thus computed as

$$y_n^*(t + FH) = y_n^{clr}(t + FH) \times \frac{1}{N} \sum_{i=0}^{N-1} \frac{y_n(t - t_0 - i\Delta t)}{y_n^{clr}(t - t_0 - i\Delta t)}. \quad (9)$$

Often, a rolling averaged is used so $t_0 = 0$, Δt is the time resolution of the measured data, and N is chosen so $(N - 1)\Delta t$ gives the desired averaging time. The total averaging time does not limit the frequency with which forecasts can be made. For example, a 5 min rolling average persistence can be recomputed every 1 min and still provide a useful forecast since new data is incorporated every time a forecast is made. An example of time-averaged persistence error with different averaging times using a rolling average is shown in Fig. 6.

4.4. Spatially-averaged persistence

If multiple measurements of irradiance are available in an area, one can make a persistence forecast based on the average clear-sky index of all the sensors. We refer to this method as spatially-averaged persistence. To make these forecasts, the measurements of multiple sensors are first converted to clear-sky indices using clear-sky expectations for each sensor. Then, these clear-sky indices are averaged

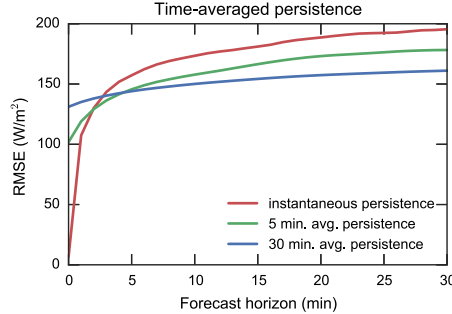


Fig. 6. Comparison of time-averaged persistence forecasts with different averaging times. The averages shown are made via a rolling average ($t_0 = 1$) with $\Delta t = 1$ s and N adjusted for each curve to give the appropriate total averaging time as described in Section 4.3. Longer time averages reduce errors at longer time horizons.

together. This average clear-sky index is then multiplied by the clear-sky expectation of the target sensor to produce a forecast for that sensor. Using N sensors, the spatially-averaged persistence for sensor n is

$$y_n^*(t + FH) = y_n^{clr}(t + FH) \times \frac{1}{N} \sum_{m=1}^N \frac{y_m(t)}{y_m^{clr}(t)}. \quad (10)$$

This method does not perform as well as clear-sky index persistence or measurement persistence at time horizons under a few minutes, as shown in Fig. 5, but it is more accurate (according the RMSE metric) than other persistence methods discussed here at longer (2–30 min) forecast horizons.

One could also imagine replacing the simple mean in Eq. (10) with a weighted mean by, for example, using the lasso (Yang et al., 2015) or some other shrinkage and selection method. Time and spatial averaging can also be combined as discussed in Section 5.1.

5. Results

We now present the results of the network and persistence forecasts using metrics defined in Zhang et al. (2015) and Section 3 for the study period of April, May, and June 2014. First, we evaluate persistence forecasts. Then, we study network forecast errors in depth. Finally, we compare network forecasts to other irradiance forecasting methods.

5.1. Persistence forecast results

Root-mean squared errors from the four types of persistence forecasts described above are plotted in Fig. 5. We see that for the 46 cloudy days we studied in Tucson, AZ., the two types of input averaging, spatial and temporal, both improve forecasts compared to clear-sky index persistence after time horizons of a few minutes. The cross-

over time depends on the weather. As expected, clear-sky index persistence performs better than measurement persistence because it accounts for the diurnal cycle.

Though Fig. 5 shows spatially-averaged persistence outperforming time-averaged persistence, the averaging time and number of sensors averaged can change these curves significantly. Figs. 6 and 7 show various averaging times and number of sensors in the average, respectively. We see that longer averaging times reduce errors at time horizons greater than 5 min but are worse at shorter time horizons. The common auto-regressive moving average (ARMA) model similarly weights previous values and/or errors to produce a forecast. We also see that adding more sensors to a spatially-averaged persistence reduces errors except at time horizons shorter than a few minutes.

One explanation for our finding that spatially-averaged persistence performs better than time-averaged persistence is related to the number of dimensions in each average. Using kinematics ($x = vt$) we can map the time series $y_i(t)$ onto a one-dimensional transect in space downwind from the sensor. In comparison, the spatial average uses data from locations that are distributed in two dimensions including some locations that are upwind of the location of interest. By averaging over two dimensions, not one, spatial average persistence effectively uses more independent samples of the cloud field. This theory assumes that all sensors are subject to the same cloud field, which is reasonable for the size of our network.

When we average the input data over both space and time, as shown as the green line in Fig. 8, we find the RMSE is lower at longer time horizons.

5.2. Network forecast results

We now compare our network forecasts to a clear sky ($k_n^*(t) = 1$) forecast, measurement persistence, clear-sky index persistence, and spatially averaged persistence (using the same 16 sensors which were used to make the network forecast). Fig. 9 shows the MAE for these methods for only

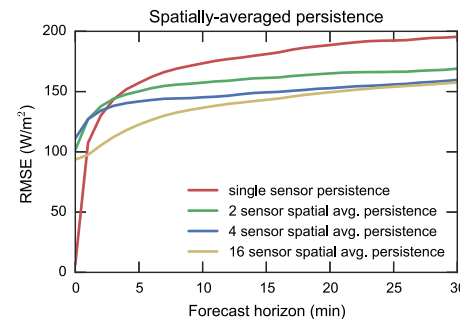


Fig. 7. Comparison of spatially-average persistence forecasts with a varying number of sensors averaged. Adding more sensors to the spatial average improves the forecast RMSE.

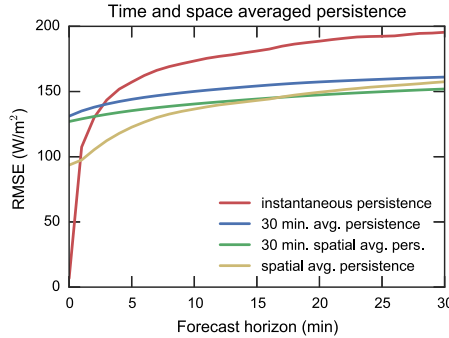


Fig. 8. Comparison of a persistence forecast made by first averaging over space and then averaging over time (green line) to other persistence methods. Averaging in time and space marginally improves forecasts at longer time horizons. (For interpretation of the references to color in this figure legend, the reader is referred to the web version of this article.)

cloudy days while Fig. 10 shows the RMSE. Plots of CRMSE show similar trends. Note that network forecasts have nonzero error at zero forecast horizons because of the smoothing applied when making the interpolated clear-sky index map and due to limiting the maximum forecasted clear-sky index to 1.25. We see that network forecasts have lower MAE than other methods for time horizons from 1 min to 30 min. We only graph up to 30 min forecast horizons because the 30 min to 2 h errors are similar and uninteresting. Fig. 10 shows that the network forecasts have lower RMS errors than the other methods at forecast horizons less than about 4 min and then have slightly higher RMSE values than spatially-averaged persistence. This difference between RMSE and MAE suggests that network forecasts have fewer small errors but more large errors than spatially-averaged persistence forecasts. For completeness, we also present error metrics for all 91 days in the study period in Appendix A. Clear days show similar trends

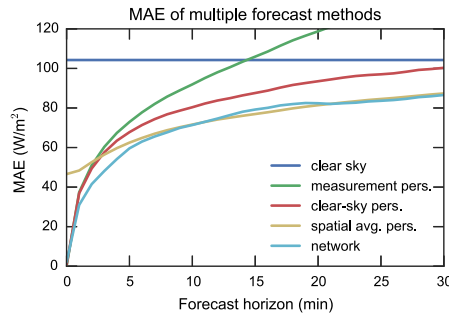


Fig. 9. MAE of many types of forecasts averaged over 46 cloudy days. Clear sky refers to a forecast where one assumes the sky is always clear ($k_n^*(t) = 1$). Network forecasts have the lowest MAE at all time horizons shown.

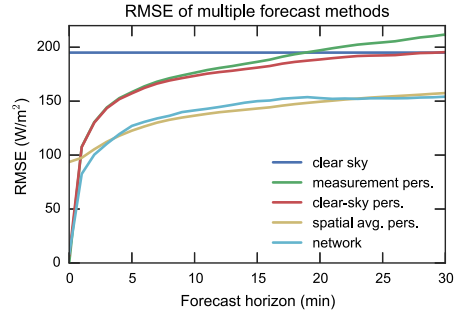


Fig. 10. RMSE of many types of forecasts averaged over 46 cloudy days. Clear sky refers to a forecast where one assumes the sky is always clear ($k_n^*(t) = 1$).

but with smaller errors which lowers the 91 day average RMSE by 40–50% depending on the time horizon.

We also compute forecast skill as defined by Marquez and Coimbra (2012). Fig. 11 illustrates the regressions used to calculate the average skill of our forecasts. At low clear-sky index persistence RMSE values (e.g. clear days), we see that the skill is negative (network RMSE > clear-sky index persistence RMSE). For days with larger clear-sky index persistence RMSE values, we see that our network forecasts have positive skill. The average skill found from regressions, typically 20%, is plotted in Fig. 12 as a function of forecast horizon.

5.3. Exploration of forecast errors

The forecast skill of the network-based forecasts remains at a surprising +20% at time horizons through 2 h. This was unexpected because the finite domain of the network is usually transited by clouds in 10–20 min. To explain this finding, we revisited the underlying statistics of forecast skill. The root mean squared error can be written as

$$\text{RMSE} = \sqrt{\sigma_f^2 + \sigma_o^2 - 2\sigma_f\sigma_o\rho + \text{MBE}^2}, \quad (11)$$

where σ_f is the forecast standard deviation, σ_o is the measurement standard deviation, ρ is the correlation coefficient, and MBE is the mean bias error (Taylor, 2001). When correlations and biases are small, the RMSE reduces to a sum in quadrature of the observation and measurement standard deviations. Under these conditions, a smoother forecast will have a lower RMSE, and thus a more positive forecast skill, than a more variable forecast. Of course, this does not mean that the smoother forecast is more skillful under most definitions of the word.

As an alternative means of understanding the relative merits of our forecast methods, we turned to Taylor diagrams (Taylor, 2001). The Taylor diagram in Fig. 13 shows the CRMSE, correlation coefficient, and standard

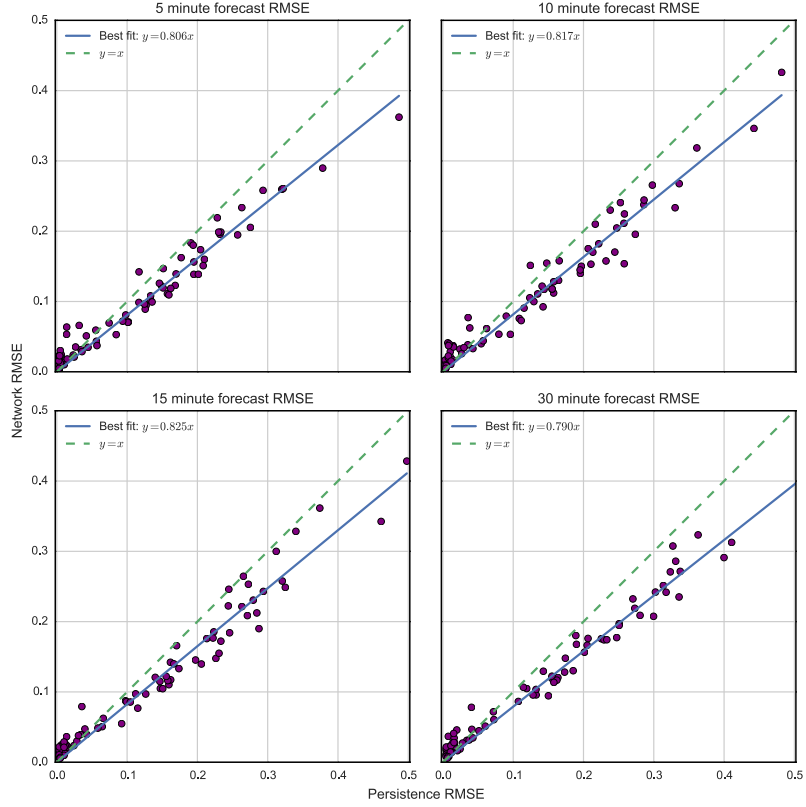


Fig. 11. Network RMSE vs clear-sky index persistence RMSE for all days and 5, 10, 15, and 30 min forecast horizons calculated for clear-sky indices. The slope of the best fit line is used to approximate the skill of the forecasts. Each point represents one day of data and forecasts. The forecast skill is positive for any point below the $y = x$ line. The plots illustrate that network forecasts may have negative skill for days that are nearly clear. Furthermore, they show a consistent positive skill for cloudier days with few outliers.

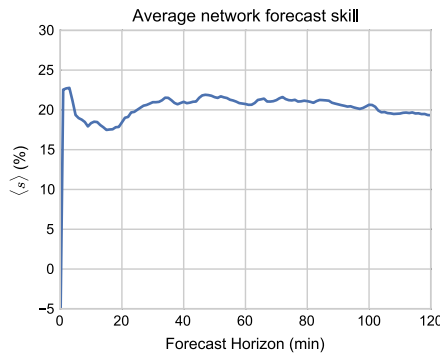


Fig. 12. Average skill of our network forecasts for the study period of April, May, and June 2014.

deviations of clear-sky index forecasts for each forecast method. Here, we analyzed forecasts of clear-sky index instead of irradiance so all values are dimensionless. The solid contour lines are lines of constant CRMSE. We see that network forecasts have correlations greater than or approximately equal to spatially-averaged persistence but with higher standard deviation. This means network forecasts capture more variability. Network forecast standard deviation transitions from performing like clear-sky index persistence forecasts at short time horizons to approaching spatially-averaged persistence, analogous to the transitions for MAE and RMSE in Figs. 9 and 10. At roughly 30 min forecast horizons, network forecasts behave about the same as spatially-averaged persistence forecasts as we expect based on the method used and average cloud velocities. Hence, we say that our network forecasts are more useful than simple spatial averaging for forecast horizons

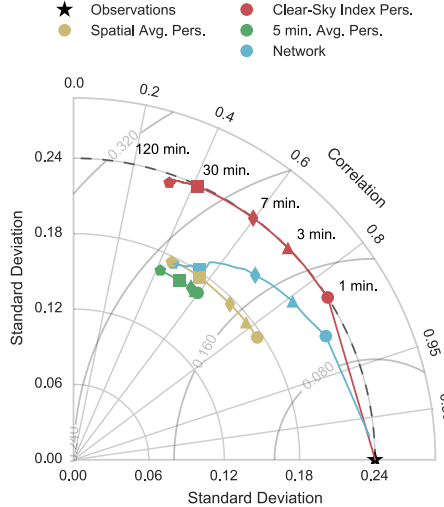


Fig. 13. Taylor diagram for clear-sky index persistence (red), spatially-averaged persistence (yellow), 5-min time-averaged persistence (green), and network (light blue) forecasts for 1 min (circle), 3 min (triangle), 7 min (diamond), 30 min (square), and 120 min (pentagon) forecast horizons. The black dashed line indicates the standard deviation of the data. Solid contours around the observations point are lines of constant CRMSE. Forecasts for clear-sky index were used so all quantities are dimensionless. At the 120 min forecast horizon, the spatially-averaged persistence and network points overlap. Network forecasts start with a standard deviation near that of the measurements, but this decreases at longer time horizons as the network forecast begins to resemble spatially-averaged persistence. (For interpretation of the references to color in this figure legend, the reader is referred to the web version of this article.)

less than 30 min. Regardless of their forecast skill metric scores, assessing the utility of network and spatial-average persistence forecasts past 30 min is challenging. We therefore suggest that researchers restrict their use of forecast skill to methods which have similar mean bias errors and standard deviations.

Fig. 13 also shows how network and spatially-averaged persistence forecasts always have lower RMSE than clear-sky index persistence after a certain horizon. This is a result of the combination of lower standard deviation and higher correlation for the network and spatially-averaged persistence forecasts. This trend holds for even longer forecast horizons. Unfortunately, Eq. (11) does not simplify for the forecasts and data shown here so both correlation and standard deviation need to be considered to understand RMSE.

5.4. Limitations and comparisons to other work

One limitation of the current network algorithm is that it does not account for multiple cloud layers. Satellite images from many of the studied days confirm that multiple cloud layers were moving in different directions. We

also studied incorporating data from times in the past appropriately shifted by cloud motion vectors but found no noticeable improvement, likely due to this complex motion.

On a day with a single cloud layer coming from the southwest shown in Fig. 14, we see that a single upstream sensor greatly improves network forecasts at around the 7 min forecast horizon. This demonstrates that the network method can perform quite well if the velocity of the clouds is well defined and the sensors are appropriately located.

Another limitation is the size of the irradiance network. Depending on the wind motion vectors clouds can pass from the edge of the network to the center in 10 min. Since the boundary is set to the spatial average of sensors, network forecasts converge to spatially averaged persistence.

Still, our current method of network forecasting performs as well as or better than both clear-sky index and spatially-averaged persistence. Error statistics for network forecasts for cloudy days are presented in Table 1.

When we compared our current network method and high resolution data with the previous work of Lonij et al. (2013), we see that our new method performs favorably. Lonij et al. use a network of 80 rooftop PV systems in the Tucson area with 15 min averaged power data to make short-term forecasts of power. Their method uses a similar cloud translation method as this work, but wind vectors are obtained from NOAA forecasts, via optimization of the wind vector to minimize RMS forecast errors, or via a Kalman filter applied to optimized vectors. At 15 and 30 min forecast horizons, the best forecasts of Lonij et al. had skills of -8.0% and 2.4%, respectively, while our new method has skills of 17.7% and 21.2%. Even compared to the optimized “forecasts” (which were not true forecasts) with skills of 1.6% and 34.5% at 15 and

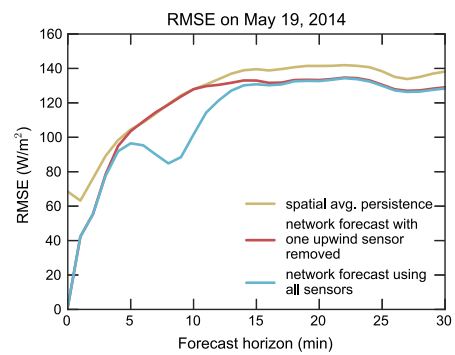


Fig. 14. RMSE vs forecast horizon on May 19, 2014 for network forecasts made with all the sensors in the network (blue) and with one upwind sensor removed (red), along with a spatially-averaged persistence forecast (yellow). The dip at 7 min for the forecast using the full network illustrates that properly placed upstream sensors do improve forecasts over a simple spatial average. (For interpretation of the references to color in this figure legend, the reader is referred to the web version of this article.)

Table 1

Summary of error statistics for network forecasts for the 46 days with clouds. Error statistics were calculated for the entire dataset at once. Only forecasts and data with solar zenith angle less than 75° were used. The mean irradiance was $\bar{y} = 662 \text{ W/m}^2$ and the mean clear-sky index was $k = 0.92$.

FH (min)	rMAE (%)	MAE (W/m^2)	MBE (W/m^2)	rRMSE (%)	RMSE (W/m^2)	Avg. skill (%)
1	4.96	30.97	-1.44	11.90	82.55	22.96
3	7.51	48.13	-1.39	15.89	110.46	23.09
5	9.29	59.59	-3.91	18.67	127.06	19.65
10	11.39	71.38	-8.59	22.11	141.44	18.63
20	13.23	82.39	-10.46	24.03	152.84	18.66
30	13.95	86.57	-7.52	24.49	154.15	21.21
60	15.45	95.59	-6.65	26.59	160.72	21.00
120	17.02	106.51	-2.01	29.20	172.45	19.58

30 min, our new method performs well. We only used 3 months of data from our real-time network while Lonij et al. used one year of data.

Chu et al. (2015b) produced a cloud tracking forecast of PV power with an ANN applied to a deterministic forecast using a sky imager at a site near the Nevada/Arizona border. The initial deterministic forecast model does not perform well compared to persistence, with negative skills at 5, 10, and 15 min forecast horizons. However, the reforecast using an ANN technique improves the result with skills of 15.1%, 21.8%, and 26.2% at forecast horizons of 5, 10, and 15 min respectively, which are comparable to our technique. Similar optimization could be applied to our deterministic network forecasts to further improve skill. A Taylor diagram of both the initial deterministic forecast and ANN re-forecast would be useful as another method to assess the forecasts.

Compared to the regression methods in Yang et al. (2015), our forecasts perform comparably at the 5 min forecast horizon. Yang et al. used 1 s irradiance data from Oahu and applied the lasso and ordinary least squares regression methods to make very short term (< 5 min) forecasts. At shorter horizons, both methods can outperform the reference persistence forecast. Since our forecasts approach the clear-sky index persistence model, regression methods are likely a better choice if sub-five minute time horizons forecasts are needed, at least for the region studied here.

6. Conclusion

We presented a deterministic method to forecast irradiance that uses data from a network of irradiance sensors as the primary input. This method can combine the benefits of clear-sky index persistence and spatially-averaged persistence into one forecast. It outperforms a reference clear-sky index persistence model for 1–120 min forecast horizons. Much of this improvement is due to spatial averaging, which shows surprising utility for the region and time period studied. However, network forecasts still exhibit more variability than spatially-averaged persistence, thus we claim network forecasts are better at forecasts horizons less than 30 min. The results presented here used numerical weather model winds at a single layer of the

atmosphere to perform cloud advection, so complex cloud movement or incorrect cloud motion vectors likely limited the accuracy. The limited size and density of the network also limits the accuracy of network forecasts.

We showed that forecast skill can be a misleading metric, and we instead used a Taylor diagram to better understand the differences among forecast methods. This lead us to reinterpret our finding that network forecasts show significant skill to 2 h forecast horizons so now we make a more informed claim that network forecasts show meaningful skill out to 30 min forecast horizons. We encourage other authors to make use of Taylor diagrams when assessing the quality of forecasts.

While the method presented may have a limited useful maximum forecast horizon, the irradiance sensor network will be a valuable asset to make other types of forecasts. For instance, regression methods using a network can improve very short time horizon forecasts (Yang et al., 2015). In the future, we could use the network of sensors to improve satellite image forecasts similar to Marquez et al. (2013) and to validate numerical weather model forecasts. We may also study how different interpolation methods affect the results of our network-based forecasting method in a detailed comparison.

Acknowledgments

This work was supported by Tucson Electric Power (TEP). We thank Mike Leuthold from the University of Arizona Department of Atmospheric Sciences for providing WRF data, and the University of Arizona Renewable Energy Network (UAREN) for institutional support. We also thank Technicians for Sustainability, a local solar PV installer, for providing data from rooftop PV systems in near real-time for forecasting and analysis. WFH thanks the Department of Energy (DOE) Office of Energy Efficiency and Renewable Energy (EERE) Postdoctoral Research Award for support.

Appendix A. Analysis for both clear and cloudy days

Table A.2 presents error statistics calculated over all 91 days in the study period. As expected, the magnitude of errors is smaller when more clear days are included.

Table A.2

Summary of error statistics for network forecasts for all 91 days. Error statistics were calculated for the entire dataset at once. Only forecasts and data with solar zenith angle less than 75° were used. The mean irradiance was $\bar{y} = 694 \text{ W/m}^2$ and the mean clear-sky index was $\bar{k} = 0.96$.

FH (min)	rMAE (%)	MAE (W/m^2)	MBE (W/m^2)	rRMSE (%)	RMSE (W/m^2)	Avg. skill (%)
1	2.92	18.40	-0.97	8.84	61.67	22.54
3	4.40	28.31	-1.69	11.71	81.31	22.77
5	5.43	35.09	-4.05	13.70	93.09	19.36
10	6.76	42.90	-8.48	16.19	103.53	18.33
20	7.78	49.06	-9.79	17.58	111.76	18.43
30	8.16	51.35	-8.43	17.91	112.73	20.97
60	8.97	56.41	-7.88	19.44	117.55	20.74
120	9.89	62.72	-4.75	21.34	126.16	19.33

Appendix B. Supplementary material

Location metadata, measurements, clear-sky expectations, and cloud motion vectors used in this study have been released online under the CC-BY-NC 4.0 license (Lorenzo et al., 2015).

References

- Achleitner, S., Kamthe, A., Liu, T., Cerpa, A.E., 2014. SIPS: solar irradiance prediction system. In: IPSN-14 Proceedings of the 13th International Symposium on Information Processing in Sensor Networks, pp. 225–236. <http://dx.doi.org/10.1109/IPSN.2014.6846755>.
- Bilionis, I., Constantinescu, E.M., Anitescu, M., 2014. Data-driven model for solar irradiation based on satellite observations. Sol. Energy 110, 22–38. <http://dx.doi.org/10.1016/j.solener.2014.09.009>.
- Bosch, J., Zheng, Y., Kleissl, J., 2013. Deriving cloud velocity from an array of solar radiation measurements. Sol. Energy 87, 196–203. <http://dx.doi.org/10.1016/j.solener.2012.10.020>.
- Chu, Y., Pedro, H.T., Li, M., Coimbra, C.F., 2015a. Real-time forecasting of solar irradiance ramps with smart image processing. Sol. Energy 114, 91–104. <http://dx.doi.org/10.1016/j.solener.2015.01.024>.
- Chu, Y., Urquhart, B., Gohari, S.M., Pedro, H.T., Kleissl, J., Coimbra, C. F., 2015b. Short-term reforecasting of power output from a 48 MW solar PV plant. Sol. Energy 112, 68–77. <http://dx.doi.org/10.1016/j.solener.2014.11.017>.
- Cormode, D., 2015. Large and Small Photovoltaic Powerplants. Phd Dissertation. University of Arizona.
- Diagne, M., David, M., Boland, J., Schmutz, N., Lauret, P., 2014. Post-processing of solar irradiance forecasts from WRF model at Reunion Island. Sol. Energy 105, 99–108. <http://dx.doi.org/10.1016/j.solener.2014.03.016>.
- Elsinga, B., van Sark, W.G., 2014. Inter-system time lag due to clouds in an urban PV ensemble. In: 2014 IEEE 40th Photovoltaic Specialist Conference (PVSC). No. 4, pp. 0754–0758. <http://dx.doi.org/10.1109/PVSC.2014.6925029>.
- Franke, R., 1982. Scattered data interpolation: tests of some methods. Math. Comput. 38 (157), 181–200. <http://dx.doi.org/10.1090/S0025-5718-1982-0637296-4>.
- Fung, V., Bosch, J.L., Roberts, S.W., Kleissl, J., 2014. Cloud shadow speed sensor. Atmos. Meas. Tech. 7 (6), 1693–1700. <http://dx.doi.org/10.5194/amt-7-1693-2014>.
- Guemard, C.A., 2008. REST2: high-performance solar radiation model for cloudless-sky irradiance, illuminance, and photosynthetically active radiation validation with a benchmark dataset. Sol. Energy 82 (3), 272–285. <http://dx.doi.org/10.1016/j.solener.2007.04.008>.
- Hammer, A., Heinemann, D., Lorenz, E., Lückebe, B., 1999. Short-term forecasting of solar radiation: a statistical approach using satellite data. Sol. Energy 67 (1–3), 139–150. [http://dx.doi.org/10.1016/S0038-092X\(00\)00038-4](http://dx.doi.org/10.1016/S0038-092X(00)00038-4).
- Hill, C.A., Such, M.C., Chen, D., Gonzalez, J., Grady, W.M., 2012. Battery energy storage for enabling integration of distributed solar power generation. IEEE Trans. Smart Grid 3 (2), 850–857. <http://dx.doi.org/10.1109/TSG.2012.2190113>.
- Ineichen, P., Perez, R., 2002. A new airmass independent formulation for the Linke turbidity coefficient. Sol. Energy 73 (3), 151–157. [http://dx.doi.org/10.1016/S0038-092X\(02\)00045-2](http://dx.doi.org/10.1016/S0038-092X(02)00045-2).
- Iman, R.H., Pedro, H.T., Coimbra, C.F., 2013. Solar forecasting methods for renewable energy integration. Prog. Energy Combust. Sci. 39 (6), 535–576. <http://dx.doi.org/10.1016/j.pecs.2013.06.002>.
- Joskow, P.L., 2011. Comparing the costs of intermittent and dispatchable electricity generating technologies. Am. Econ. Rev. 101 (3), 238–241. <http://dx.doi.org/10.1257/aer.101.3.238>.
- Kleissl, J. (Ed.), 2013. Solar Energy Forecasting and Resource Assessment, first ed. Elsevier, Oxford. <http://dx.doi.org/10.1016/B978-0-12-397177-7.18001-5>.
- Lauret, P., Diagne, M., David, M., 2014. A neural network post-processing approach to improving NWP solar radiation forecasts. Energy Procedia 57, 1044–1052. <http://dx.doi.org/10.1016/j.egypro.2014.10.089>.
- Lave, M., Kleissl, J., 2013. Cloud speed impact on solar variability scaling application to the wavelet variability model. Sol. Energy 91, 11–21. <http://dx.doi.org/10.1016/j.solener.2013.01.023>.
- Leuthold, M., 2015. The University of Arizona Department of Atmospheric Sciences – Arizona Regional WRF Model Data. <<http://www.atmo.arizona.edu/index.php?section=weather&id=wrf>>.
- Lipperheide, M., Bosch, J., Kleissl, J., 2015. Embedded nowcasting method using cloud speed persistence for a photovoltaic power plant. Sol. Energy 112, 223–238. <http://dx.doi.org/10.1016/j.solener.2014.11.013>.
- Lonij, V.P., Brooks, A.E., Cronin, A.D., Leuthold, M., Koch, K., 2013. Intra-hour forecasts of solar power production using measurements from a network of irradiance sensors. Sol. Energy 97, 58–66. <http://dx.doi.org/10.1016/j.solener.2013.08.002>.
- Lorenzo, A.T., Cronin, A.D., Holmgren, W.F., 2015. Irradiance Monitoring Network Data and Wind Motion Vectors. <<http://zenodo.org/record/29070>>.
- Lorenzo, A.T., Holmgren, W.F., Leuthold, M., Kim, C.K., Cronin, A.D., Betterton, E.A., 2014. Short-term PV power forecasts based on a real-time irradiance monitoring network. 2014 IEEE 40th Photovoltaic Specialist Conference (PVSC), pp. 0075–0079. <http://dx.doi.org/10.1109/PVSC.2014.6925212>.
- Marquez, R., Coimbra, C.F.M., 2012. Proposed metric for evaluation of solar forecasting models. J. Sol. Energy Eng. 135 (1), 011016. <http://dx.doi.org/10.1115/1.4007496>.
- Marquez, R., Pedro, H.T., Coimbra, C.F., 2013. Hybrid solar forecasting method uses satellite imaging and ground telemetry as inputs to ANNs. Sol. Energy 92, 176–188. <http://dx.doi.org/10.1016/j.solener.2013.02.023>.
- Mathiesen, P., Kleissl, J., 2011. Evaluation of numerical weather prediction for intra-day solar forecasting in the continental United States. Sol. Energy 85 (5), 967–977. <http://dx.doi.org/10.1016/j.solener.2011.02.013>.

- Nuss, W.A., Titley, D.W., 1994. Use of multiquadric interpolation for meteorological objective analysis. *Mon. Weather Rev.* 122 (7), 1611–1631. [http://dx.doi.org/10.1175/1520-0493\(1994\)122<1611:UOMIFM>2.0.CO;2](http://dx.doi.org/10.1175/1520-0493(1994)122<1611:UOMIFM>2.0.CO;2).
- Perez, R., Kivalov, S., Schlemmer, J., Hemker, K., Renné, D., Hoff, T.E., 2010. Validation of short and medium term operational solar radiation forecasts in the US. *Sol. Energy* 84 (12), 2161–2172. <http://dx.doi.org/10.1016/j.solener.2010.08.014>.
- Perez, R., Lorenz, E., Pelland, S., Beauharnois, M., Van Knowe, G., Hemker, K., Heinemann, D., Remund, J., Müller, S.C., Traunmüller, W., Steinmauer, G., Pozo, D., Ruiz-Arias, J.A., Lara-Fanego, V., Ramirez-Santigosa, L., Gaston-Romero, M., Pomares, L.M., 2013. Comparison of numerical weather prediction solar irradiance forecasts in the US, Canada and Europe. *Sol. Energy* 94, 305–326. <http://dx.doi.org/10.1016/j.solener.2013.05.005>.
- Sirayanone, S., 1988. Comparative Studies of Kriging, Multiquadric-Biharmonic and other Methods for Solving Resources Problems. Dissertation. Iowa State University.
- Taylor, K.E., 2001. Summarizing multiple aspects of model performance in a single diagram. *J. Geophys. Res.: Atmos.* 106 (D7), 7183–7192. <http://dx.doi.org/10.1029/2000JD900719>.
- Urquhart, B., Ghonima, M., Nguyen, D.A., Kurtz, B., Chow, C.W., Kleissl, J., 2013. Sky-imaging systems for short-term forecasting. *Solar Energy Forecasting and Resource Assessment*. Elsevier, pp. 195–232. <http://dx.doi.org/10.1016/B978-0-12-397177-7.00009-7> (Chapter 9).
- Webster, R., Oliver, M.A., 1993. How large a sample is needed to estimate the regional variogram adequately? In: Soares, A. (Ed.), *Geostatistics Tróia 92 SE – 14*. In: Quantitative Geology and Geostatistics, vol. 5. Springer, Netherlands, pp. 155–166. http://dx.doi.org/10.1007/978-94-011-1739-5_14.
- Wilcox, S., Andreas, A., 2010. Solar Resource & Meteorological Assessment Project (SOLRMAP): Observed Atmospheric and Solar Information System (OASIS); Tucson, Arizona (Data). <http://dx.doi.org/10.7799/105226>.
- Yang, D., Ye, Z., Lim, L.H. I., Dong, Z., 2015. Very short term irradiance forecasting using the lasso. *Sol. Energy* 114, 314–326. <http://dx.doi.org/10.1016/j.solener.2015.01.016>.
- Yang, H., Kurtz, B., Nguyen, D., Urquhart, B., Chow, C.W., Ghonima, M., Kleissl, J., 2014. Solar irradiance forecasting using a ground-based sky imager developed at UC San Diego. *Sol. Energy* 103, 502–524. <http://dx.doi.org/10.1016/j.solener.2014.02.044>.
- Zhang, J., Florita, A., Hodge, B.-M., Lu, S., Hamann, H.F., Banunarayanan, V., Brockway, A.M., 2015. A suite of metrics for assessing the performance of solar power forecasting. *Sol. Energy* 111, 157–175. <http://dx.doi.org/10.1016/j.solener.2014.10.016>.

APPENDIX C

REPRINT: OPTIMAL INTERPOLATION OF SATELLITE DERIVED
IRRADIANCE AND GROUND DATA

The following manuscript was published in the proceedings of the 2016 IEEE 43rd Photovoltaic Specialist Conference (PVSC). Further background material is presented in Chapter 4 of this dissertation. The manuscript is reprinted with permission from IEEE. Copyright (2016) by IEEE. Original reference: A. T. Lorenzo, M. Morfeld, W. F. Holmgren and A. D. Cronin, "Optimal interpolation of satellite derived irradiance and ground data," 2016 IEEE 43rd Photovoltaic Specialists Conference (PVSC), Portland, OR, 2016, pp. 0291–0296. doi: 10.1109/PVSC.2016.7749596

Optimal Interpolation of Satellite Derived Irradiance and Ground Data

Antonio T. Lorenzo*, Matthias Morzfeld†, William F. Holmgren†, Alexander D. Cronin§

*College of Optical Sciences, University of Arizona, Tucson, AZ, 85721, United States

†Department of Mathematics, University of Arizona, Tucson, AZ, 85721, United States

‡Department of Atmospheric Sciences, University of Arizona, Tucson, AZ, 85721, United States

§Department of Physics, University of Arizona, Tucson, AZ, 85721, United States

Abstract—We describe how Bayesian data assimilation can be used to improve nowcasts of irradiance over small, city-scale, spatial areas. Specifically, we use optimal interpolation (OI) to improve satellite derived estimates of global horizontal irradiance (GHI) using ground truth data that was collected sparsely over Tucson, AZ. Our results show that the local data indeed improves the satellite derived estimates of GHI. A key to success with OI in this context is to prescribe correlations based on cloudiness, rather than spatially. OI can be used with a variety of data, e.g., rooftop photovoltaic production data or irradiance data, as well as with several different satellite derived irradiance models.

Index Terms—data assimilation, optimal interpolation, remote sensing, solar irradiance

I. INTRODUCTION

Accurate estimates of the global horizontal irradiance (GHI) are crucial to the deployment and grid integration of photovoltaic (PV) systems. Satellite derived GHI estimates are used to design and site PV power plants, to forecast the power output of a fleet of PV generators, and to provide electric utilities real-time estimates of the distributed generation (DG) or “behind the meter” generation of rooftop PV systems. Data assimilation provides a framework to combine the large area coverage of GHI estimates derived from satellite imagery with the more accurate data of ground sensors.

Previous work has also explored using data assimilation techniques to improve solar radiation estimates [1], [2]. We use optimal interpolation (OI), which can be thought of as a generalized least squares approach [3]. OI is a statistical method to combine prior information about some parameter (the background) with observations based on the errors and correlations in the background and observations. The background is computed from satellite estimates, the observations come from a mix of GHI sensors and rooftop PV systems. OI is also used by [2], where numerical weather prediction (NWP) solar radiation data are combined with ground sensors. A key difference and innovation in our paper is that correlations used for OI are prescribed based on differences in cloudiness between locations, rather than spatial distance.

Our paper is organized as follows. We describe OI in Sec. II and apply it to satellite GHI estimates in Sec. III. We discuss the results in Sec. IV and future work in Sec. V. Finally, a summary is provided in Sec. VI.

II. OPTIMAL INTERPOLATION PROCEDURE

A. Method

We briefly describe the OI method; the derivation can be found in many data assimilation textbooks, e.g. [3]. The output of an OI routine (known as the analysis), $\hat{\mathbf{x}}$, is a vector of length N and is a weighted sum of the background (the prior information represented as an N vector), \mathbf{x}_b , and the measurements, \mathbf{y} (M vector):

$$\hat{\mathbf{x}} = \mathbf{x}_b + \mathbf{W}(\mathbf{y} - \mathbf{H}\mathbf{x}_b). \quad (1)$$

In this study, \mathbf{x}_b is composed of satellite derived clear-sky indices and \mathbf{y} is composed of clear-sky indices from a number of ground irradiance sensors. The observation matrix, \mathbf{H} ($M \times N$ matrix), maps points in the background space to points in observation space. We construct \mathbf{H} using the nearest neighbor approach of selecting the background points that are closest to the observation locations. The weight matrix, \mathbf{W} ($N \times M$ matrix), is constructed from the error covariance matrix of the background, \mathbf{P} ($N \times N$ matrix), and the error covariance of the observations, \mathbf{R} ($M \times M$ matrix) as

$$\mathbf{W} = \mathbf{PH}^T(\mathbf{R} + \mathbf{PH}\mathbf{H}^T)^{-1}. \quad (2)$$

We also compute the error covariance matrix of the analysis, $\hat{\mathbf{P}}$ ($N \times N$ matrix), as

$$\hat{\mathbf{P}} = (\mathbf{I} - \mathbf{WH})\mathbf{P}, \quad (3)$$

where \mathbf{I} is the $N \times N$ identity matrix.

An essential part of the OI routine is choosing appropriate error covariance matrices, \mathbf{R} and \mathbf{P} . The standard method, that we also follow is to assume that the errors between sensors are uncorrelated so that \mathbf{R} is a diagonal matrix. Each diagonal element of \mathbf{R} is the variance of the observations at each location over a given period (in the results that follow we used the entire study period).

The method we use to obtain \mathbf{P} is novel, in fact it is the primary difference between our work and [2]. First, we separate \mathbf{P} into a correlation matrix \mathbf{C} and diagonal variance matrix \mathbf{D} :

$$\mathbf{P} = \mathbf{D}^{1/2}\mathbf{CD}^{1/2}. \quad (4)$$

We obtain \mathbf{D} in a similar manner as \mathbf{R} : we take the variance of each pixel in the satellite image over some period of time.

Care must be taken when estimating the background correlation matrix \mathbf{C} . A standard method is to assume the correlation

decays exponentially with distance between points and this approach is taken in [2]. This method works well for resource assessment with daily or longer integration times and for nowcasts at locations with sensors nearby. The method we use depends on the actual distributions of clouds as seen by the satellite. The idea is that pixels in the background that have similar cloudiness have high correlation and those with very different cloudiness have low correlation. In the final analysis, this translates to only adjusting the cloudy areas with observations that are also cloudy and leaving the clear areas to be adjusted by observations of the clear sky.

To construct the correlation matrix \mathbf{C} ($N \times N$), we first define the distance, d_{ij} , as the difference between pixel i and pixel j of an image \mathbf{v} (N vector) that defines the cloudiness,

$$d_{ij} = |v_i - v_j|. \quad (5)$$

To obtain the elements of \mathbf{C} , c_{ij} , we apply a known correlation function, k , to each distance so that

$$c_{ij} = k(d_{ij}). \quad (6)$$

Any one of a number of covariance functions could be chosen for k ; see [4] for a partial list. In this work, we studied piecewise linear correlation functions,

$$k(r) = \begin{cases} 1 - \frac{r}{l} & r < l \\ 0 & r \geq l \end{cases}, \quad (7)$$

where l is a characteristic length that must be specified. The choices of k and l need to be tuned to the area that the algorithm is applied to. Once the error covariance matrices are defined, one can compute an analysis estimate using the above equations.

B. Data used for optimal interpolation

This study applies OI to observations and geostationary satellite data from April, May, and June 2014 in Tucson, AZ. The observation data were collected from 22 diverse sensors including a calibrated NREL MIDC sensor [5], custom irradiance sensors [6], and data from rooftop PV systems. Irradiance observations were averaged to 1 minute and PV data are reported as 5 minute averages. We note that all data sources (observations and satellite images) are available in near real-time so that the OI corrected GHI images can be used as a basis for forecasts. To simplify the computation, all data were converted to clear-sky index data using clear-sky expectations for each sensor. Five sensors, including the calibrated NREL MIDC GHI sensor, were not used in the OI process for validation and error statistics are only presented for these withheld sensors. The remaining 17 sensors are used as the observations, \mathbf{y} , in the OI routine.

The satellite data were obtained from the GOES-W geostationary satellite, which was GOES-15 for the period of interest. To obtain the background error correlation, we estimate the cloudiness image, \mathbf{v} , from the 1 km resolution, visible band of the satellite as follows. We convert the raw visible brightness counts, b_i , to visible albedo, divide by the cosine of the solar

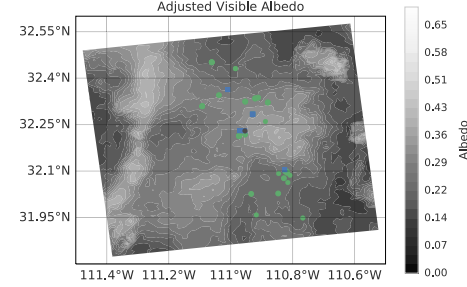


Fig. 1. Adjusted visible albedo image derived from the GOES-W visible reflectance image on 2014-04-18 18:30Z over Tucson, AZ. The lighter/high albedo areas indicate cloudy areas. The green circles are the sensors used for OI, the blue squares are the sensors used for error analysis, and the black circle in the center is the calibrated NREL MIDC sensor.

zenith angle, ϕ , to correct for the time of day, and arrive at an adjusted visible albedo,

$$v_i = \left(\frac{b_i}{255} \right)^2 / \cos(\phi_i). \quad (8)$$

We plot the adjusted visible albedo as a map over Tucson, AZ, in Fig. 1. The lighter areas in Fig. 1 correspond to areas of high albedo which indicates that the area is cloudy. This adjusted visible albedo is used to obtain the background error correlation matrix via eqs. (5)–(7) with a correlation length of $l = 0.2$. However, other quantities, such as cloud fraction, could also be used to estimate the cloudiness at each satellite pixel.

C. Satellite derived irradiance models

We studied two satellite image to GHI models to generate the background image, \mathbf{x}_b , which was also converted to clear-sky index before applying OI.

One satellite to GHI model to generate \mathbf{x}_b is a physically based model called the University of Arizona Solar Irradiance Based on Satellite (UASIBS) model [7]. UASIBS uses the visible and infrared images from the GOES-W satellite to generate a cloud mask. Then, parameterized cloud properties determined from the infrared images are used in a radiative transfer model to determine the surface GHI. This GHI estimate has the same resolution as the visible channel of the GOES-W satellite (approximately 1km).

The second model to generate \mathbf{x}_b is a semi-empirical model, which we refer to as the EM model. This model is based on the SUNY model which applies a regression to the visible channel of the GOES-W satellite [8]. The only differences between the EM model and the SUNY model are that the dynamic range is set only with the 3 months of data used in this study instead of the recommended 60 day window with seasonal correction and that the specular correction factor was neglected.

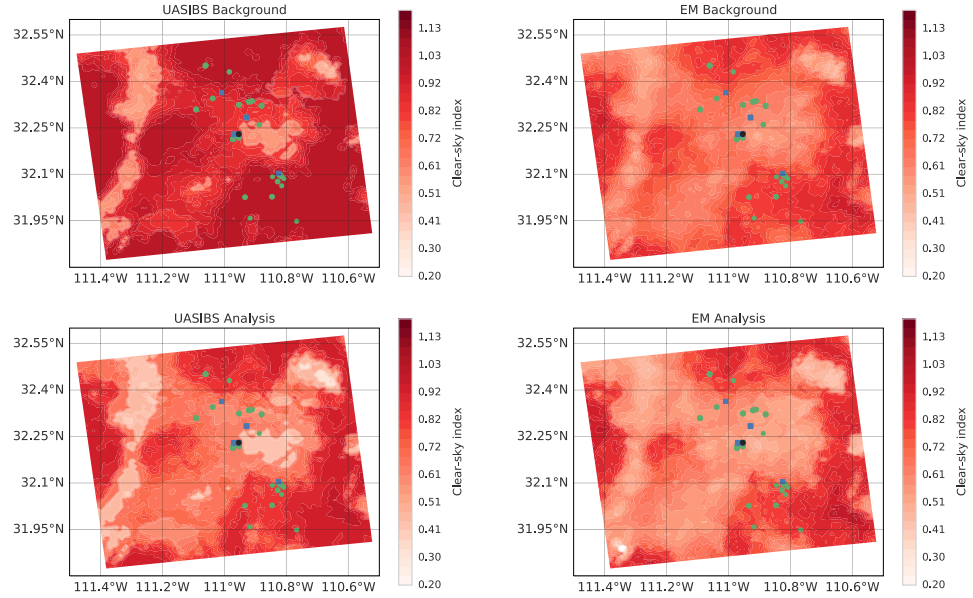


Fig. 2. Example OI results for one image/data taken on 2014-04-19 18:30Z (11:30 AM local time). The top row are the background satellite derived clear-sky index estimates before OI. The lower row are the clear-sky index analysis after performing OI. Satellite derived estimates using the UASIBS model are on the left and those using the EM model are on the right. Lighter shades indicate thicker clouds. The green circles are the sensors used for OI, the blue squares are the sensors used for error analysis, and the black circle in the center is the calibrated NREL MIDC sensor. Comparing the background and analysis, one can see that the thin cloud near the center of the image is made slightly thicker in the analysis.

III. RESULTS

In this section, we present the results of the analysis of roughly 1200 satellite images taken over Tucson, AZ. Both the UASIBS and EM models described above were used to convert the raw satellite images to estimates of GHI at the surface and then used as the background field for the OI algorithm.

Figure 2 shows uncorrected background maps of clear-sky index derived from the UASIBS and EM models and the OI corrected analysis. Notice that in the UASIBS analysis image, the thin clouds in the center of the image are thicker than in the background based on the information of the sensors near the top of the image that measure other parts of the cloud. For the EM model, OI adjusts the cloudy areas to be more cloudy and the clear areas to be more clear. We also see that the analysis images in Fig. 2 are similar suggesting that OI works robustly with different satellite image to GHI models that define the background.

Figure 3 shows an example of the errors of the background and analysis images as compared to sensor observations for a single satellite image/time processed with the UASIBS model. The errors shown are computed from sensors that are *not* used during OI. We see that the absolute error was reduced for

all sensors, including the calibrated MIDC sensor and rooftop PV systems. This suggests that the OI correctly propagates information from data to unobserved locations.

We calculated empirical cumulative distribution functions (CDF) for the observations, background, and analysis. Figure 4 shows these CDFs for the UASIBS model. The slope of zero around 0.8 in the CDF of the UASIBS background (red dashed-dotted line) indicates that the UASIBS model does not predict clear-sky indices of 0.8. The analysis (blue dashed line) does predict clear-sky indices in that range and even extends the range over 1.0 to more closely match the observations.

The empirical CDF for the EM model is shown in Fig. 5. We see that the EM model tends to over-predict clouds, but that the OI then removes much of this bias. On the other hand, the figure suggests that the analysis could be improved at smaller clear-sky indices to better match the observations.

For the 1200 images analyzed, root-mean squared errors (RMSE), mean absolute errors (MAE), and mean bias errors (MBE) decreased on average. Error statistics for the EM and UASIBS models in terms of the clear-sky index calculated over all the withheld sensors and for clear, cloudy, and all days are presented in Table I. Error statistics in units of GHI for the calibrated MIDC irradiance sensor are presented in Table II.

TABLE I

ERROR STATISTICS CALCULATED OVER 1200 SATELLITE CLEAR-SKY INDEX ESTIMATES AND OI CORRECTED ANALYSIS. BOTH THE EMPIRICAL (EM) MODEL AND UASIBS MODEL DESCRIBED IN SEC. II-C ARE SHOWN. THE MEAN ABSOLUTE ERROR (MAE), ROOT MEAN SQUARED ERROR (RMSE), AND MEAN BIAS ERROR (MBE) ARE CALCULATED OVER ALL THE WITHHELD SENSORS AND ALL IMAGE TIMES AS A SINGLE TIME-SERIES. STATISTICS WERE CALCULATED FOR ALL DAYS, ONLY CLEAR DAYS (ROUGHLY 700 DAYS), AND CLOUDY DAYS (500 DAYS). ALL NUMBERS ARE IN UNITS OF CLEAR-SKY INDEX WHICH HAS A TYPICAL RANGE OF 0 TO 1.3.

	MAE			RMSE			MBE		
	All	Clear	Cloudy	All	Clear	Cloudy	All	Clear	Cloudy
EM analysis	0.088	0.048	0.149	0.172	0.095	0.245	0.026	0.021	0.033
EM background	0.184	0.152	0.231	0.268	0.213	0.333	0.138	0.140	0.136
UASIBS analysis	0.080	0.039	0.141	0.164	0.088	0.235	-0.005	-0.004	-0.006
UASIBS background	0.094	0.047	0.164	0.190	0.099	0.275	-0.015	-0.003	-0.034

TABLE II

ERROR STATISTICS CALCULATED OVER 1200 SATELLITE GHI ESTIMATES AND OI CORRECTED ANALYSIS FOR THE CALIBRATED NREL MIDC SENSOR. BOTH THE EMPIRICAL (EM) MODEL AND UASIBS MODEL DESCRIBED IN SEC. II-C ARE SHOWN. THE MEAN ABSOLUTE ERROR (MAE), ROOT MEAN SQUARED ERROR (RMSE), AND MEAN BIAS ERROR (MBE) ARE CALCULATED OVER ALL IMAGE TIMES AS A SINGLE TIME-SERIES. STATISTICS WERE CALCULATED FOR ALL DAYS, ONLY CLEAR DAYS (ROUGHLY 700 DAYS), AND CLOUDY DAYS (500 DAYS). UNITS ARE W/m^2 .

	MAE			RMSE			MBE		
	All	Clear	Cloudy	All	Clear	Cloudy	All	Clear	Cloudy
EM analysis	56.0	23.4	104.	113.	32.3	174.	16.1	17.3	14.3
EM background	110.	85.7	145.	144.	97.0	194.	75.0	83.8	61.9
UASIBS analysis	50.9	17.5	101.	110.	26.4	171.	2.94	6.96	-3.03
UASIBS background	53.1	16.4	108.	120.	27.9	186.	-12.4	3.02	-35.2

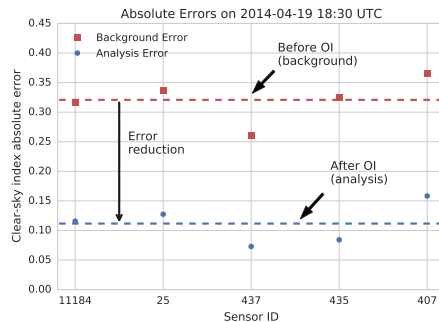


Fig. 3. A plot of the absolute error in the analysis and background images (generated with UASIBS) as compared to observations at some sensor locations showing reduced errors for a single satellite image. The sensors shown were not included in the OI correction routine. Note that sensor 11184 is the MIDC calibrated irradiance sensor and sensors 437, 435, and 407 are rooftop PV systems. The red squares indicate the absolute error in the background image while the blue circles indicate the error in the analysis. The dashed lines indicate the mean absolute errors for the sensors shown.

IV. DISCUSSION

Our results show significant improvement by the OI for the EM model. Improvements for the UASIBS model are more modest. The reasons for this are as follows. UASIBS is a more sophisticated satellite image to GHI model, so that improvements are harder to obtain. In particular, the average error values shown in the tables above differ from the large

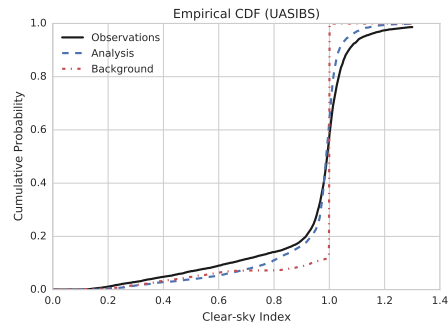


Fig. 4. UASIBS empirical cumulative distribution function. The black line is the CDF of the observations, the red dash-dotted line is the CDF of the background, and the blue dashed line is the CDF of the analysis. The UASIBS background does not predict clear-sky indices around 0.8 and does not extend beyond 1.0. The analysis shows better agreement with the observed CDF.

improvements we have seen on many days, and illustrated in Fig. 3. We suspect that average errors are likely to be affected by large errors occurring only on some days due to parallax.

Parallax refers to the discrepancy between the actual location of a cloud and the location tagged by a satellite [9]. The GOES-W satellite is located at 135°W on the equator while Tucson, AZ is at roughly 32°N and 110°W , so the satellite is viewing the clouds at an angle. The satellite geolocates each pixel as if it were at the surface. This means that a cloud

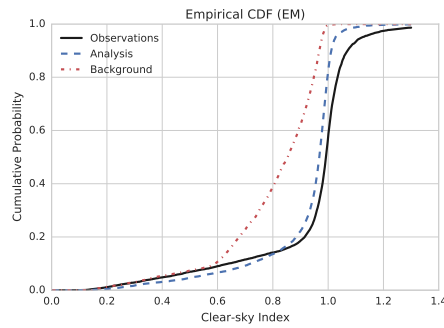


Fig. 5. The empirical cumulative distribution function for the EM model. The black line is the CDF of the observations, the red dashed-dotted line is the CDF of the background, and the blue dashed line is the CDF of the analysis. The background EM model seems to make clouds thicker than they are in reality. The analysis corrects much of this bias and changes the shape of the CDF to more closely match the observations.

obscures a pixel that is to the NE of the cloud, so the actual location of the cloud is to the SW of what the satellite tags the pixel as. Thus, when the OI algorithm tries to compare the observations with the background derived from the satellite image, the observations and background may disagree about whether a cloud is present at all.

This issue is illustrated in Fig. 6 where many sensors are near the edges of the estimated clouds. Some of the sensors locations that are reported as clear in the background are actually cloudy. The OI algorithm tries to rectify this by adjusting the areas that were clear in the background to be cloudy. When we compare this analysis to the background and adjusted visible albedo image, we see the analysis does not look physical. If we shift the satellite image by a small amount to the SW and rerun OI, we see that this shifted analysis looks more like what one would expect given the visible albedo image. This suggests that we first need to correct the parallax issue before performing OI, and that the error statistics calculated over 1200 image times are likely skewed by these errors.

V. FUTURE WORK

We plan to improve this work in several aspects. An important task will be to correct the issue of parallax that can cause large errors in the OI analysis. We have experimented with estimating the cloud top height and adjusting for parallax on a pixel by pixel basis, but found this is challenging to do well. In the future, we plan to group classes of clouds together to then determine a height for each cloud group and shift the group appropriately.

This work focused only on the area around Tucson, AZ. One future experiment could examine how OI can improve background estimates using observations that are very far apart and may experience different weather conditions.

VI. CONCLUSION

There are a number of models to convert satellite images to ground irradiance, and all are prone to errors. These satellite derived irradiance images are important to many phases of PV integration, from siting to forecasting the output of a fleet. We describe how to improve the irradiance estimates using ground data and optimal interpolation.

The optimal interpolation technique uses satellite derived estimates of GHI, ground observations, and the associated error estimates to produce a GHI estimate that has, on average, better error statistics. An important consideration for the method as described is the specification of the error correlation between pixels in the satellite image. We propose using the (almost) raw visible image from the satellite to correlate pixels based on the cloudiness at each pixel. We apply this method to a physically based satellite image to GHI model and show that the distribution of the estimated GHI more closely matches the data. Similarly, the method applied to an empirical satellite image to GHI model removes a large bias from the GHI estimate.

One limitation in the optimal interpolation method is that errors in the estimated locations of the clouds in the satellite GHI estimate can produce analysis images that are unreasonable. Thus, future work will explore correcting this issue of parallax or recognizing when this issue occurs so that optimal interpolation can be avoided for those times. Other future work includes producing a forecast from these improved satellite derived GHI nowcasts.

ACKNOWLEDGMENT

This project was funded in part by Tucson Electric Power and Arizona Public Service. We thank Technicians for Sustainability, a local solar PV installer, for providing data from rooftop PV systems. ATL thanks the University of Arizona Renewable Energy Network for support and Professor Avelino Arellano for instruction and guidance. WFH thanks the Department of Energy (DOE) Office of Energy Efficiency and Renewable Energy (EERE) Postdoctoral Research Award for support.

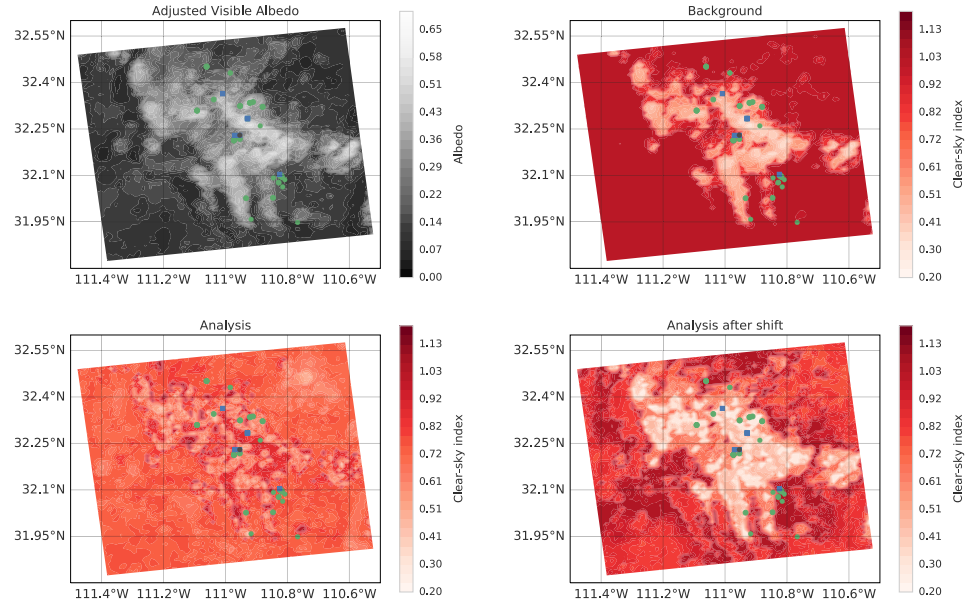


Fig. 6. Illustration of error due to parallax. The adjusted visible albedo image from the GOES-W visible channel, background clear-sky index estimate made with the USASIBS algorithm, analysis after performing OI, and analysis after shifting the satellite image are shown. The green circles are the sensors used for OI, the blue squares are the sensors used for error analysis, and the black circle in the center is the calibrated NREL MIDC sensor. We see that at sensor locations near the edge of clouds in the background, the sensors and background disagree about whether it is cloudy. This causes the OI to fail as it tries to rectify this discrepancy. If we shift the image slightly to the SW and redo the OI, we see that the sensors and background now better agree about whether the area is cloudy so that the analysis after shifting looks more reasonable.

REFERENCES

- [1] L. Linguet and J. Atif, "Estimating Surface Solar Irradiance from GOES Satellite with Particle Filter Model and Joint Probability Distribution," *Canadian Journal of Remote Sensing*, vol. 41, no. 2, pp. 71–85, jul 2015. [Online]. Available: <http://www.tandfonline.com/doi/full/10.1080/07038992.2015.1040150>
- [2] J. A. Ruiz-Arias, S. Quesada-Ruiz, E. F. Fernández, and C. A. Gueymard, "Optimal combination of gridded and ground-observed solar radiation data for regional solar resource assessment," *Solar Energy*, vol. 112, pp. 411–424, feb 2015. [Online]. Available: <http://www.sciencedirect.com/science/article/pii/S0038092X14006021>
- [3] E. Kalnay, *Atmospheric Modeling, Data Assimilation and Predictability*. Cambridge University Press, 2003.
- [4] C. Rasmussen and C. Williams, "Covariance Functions," in *Gaussian Processes for Machine Learning*. MIT Press, 2005, ch. 4, pp. 79–104. [Online]. Available: <http://ieeexplore.ieee.org/xpl/articleDetails.jsp?arnumber=6279030>
- [5] S. Wilcox and A. Andreas, "Solar Resource & Meteorological Assessment Project (SOLRMAP): Observed Atmospheric and Solar Information System (OASIS); Tucson, Arizona (Data)," nov 2010. [Online]. Available: <http://dx.doi.org/10.7799/1052226>
- [6] A. T. Lorenzo, W. F. Holmgren, M. Leuthold, C. K. Kim, A. D. Cronin, and E. a. Betterton, "Short-term PV power forecasts based on a real-time irradiance monitoring network," in *2014 IEEE 40th Photovoltaic Specialist Conference (PVSC)*, 2014, pp. 0075–0079. [Online]. Available: <http://dx.doi.org/10.1109/PVSC.2014.6925212>
- [7] C. K. Kim, W. F. Holmgren, M. Stovern, and E. A. Betterton, "Toward Improved Solar Irradiance Forecasts: Derivation of Downwelling Surface Shortwave Radiation in Arizona from Satellite," *Pure and Applied Geophysics*, may 2016. [Online]. Available: <http://link.springer.com/10.1007/s00024-016-1302-3>
- [8] R. Perez, P. Ineichen, K. Moore, M. Kmiecik, C. Chain, R. George, and F. Vignola, "A new operational model for satellite-derived irradiances: description and validation," *Solar Energy*, vol. 73, no. 5, pp. 307–317, nov 2002. [Online]. Available: <http://www.sciencedirect.com/science/article/pii/S0038092X02001226>
- [9] G. A. Vicente, J. C. Davenport, and R. A. Scofield, "The role of orographic and parallax corrections on real time high resolution satellite rainfall rate distribution," *International Journal of Remote Sensing*, vol. 23, no. 2, pp. 221–230, nov 2010. [Online]. Available: <http://www.tandfonline.com/doi/abs/10.1080/01431160010006935>

APPENDIX D

REPRINT: OPTIMAL INTERPOLATION OF SATELLITE AND GROUND
DATA FOR IRRADIANCE NOWCASTING AT CITY SCALES

The following manuscript was published as a peer-reviewed article in Solar Energy. Further discussion of this article is presented in Chapter 4 of this dissertation. The manuscript is reprinted with permission from Elsevier. Copyright (2017) by Elsevier. Original reference: A. T. Lorenzo, M. Morzfeld, W. F. Holmgren, and A. D. Cronin, “Optimal interpolation of satellite and ground data for irradiance nowcasting at city scales,” Sol. Energy, vol. 144, pp. 466-474, 2017. doi: 10.1016/j.solener.2017.01.038



Optimal interpolation of satellite and ground data for irradiance nowcasting at city scales



Antonio T. Lorenzo ^{a,*}, Matthias Morzfeld ^b, William F. Holmgren ^c, Alexander D. Cronin ^{d,a}

^a University of Arizona, College of Optical Sciences, 1630 E. University Blvd., Tucson, AZ 85721, United States

^b University of Arizona, Department of Mathematics, 617 N. Santa Rita Ave., Tucson, AZ 85721, United States

^c University of Arizona, Department of Hydrology & Atmospheric Sciences, 1118 E. 4th Street, Tucson, AZ 85721, United States

^d University of Arizona, Department of Physics, 1118 E. 4th Street, Tucson, AZ 85721, United States

ARTICLE INFO

Article history:

Received 16 November 2016

Received in revised form 4 January 2017

Accepted 15 January 2017

Keywords:

Solar irradiance

Optimal interpolation

Data assimilation

Nowcasting

ABSTRACT

We use a Bayesian method, optimal interpolation, to improve satellite derived irradiance estimates at city-scales using ground sensor data. Optimal interpolation requires error covariances in the satellite estimates and ground data, which define how information from the sensor locations is distributed across a large area. We describe three methods to choose such covariances, including a covariance parameterization that depends on the relative cloudiness between locations. Results are computed with ground data from 22 sensors over a 75 × 80 km area centered on Tucson, AZ, using two satellite derived irradiance models. The improvements in standard error metrics for both satellite models indicate that our approach is applicable to additional satellite derived irradiance models. We also show that optimal interpolation can nearly eliminate mean bias error and improve the root mean squared error by 50%.

© 2017 Elsevier Ltd. All rights reserved.

1. Introduction

Estimates of global horizontal irradiance (GHI) are essential at many stages of photovoltaic (PV) system deployment and operation. A widely used technique is to compute GHI from geostationary satellite images, which are typically available every 15–30 min and cover large areas of the globe. Such satellite derived estimates of GHI are commonly used to design and site PV power plants (Vignola et al., 2013), to forecast the output of a fleet of PV generators (Kühnert et al., 2013), and to provide real-time estimates of distributed generation (DG) or “behind the meter” generation of rooftop PV systems (Saint-Drenan et al., 2011). Satellite derived estimates have also been used to detect failures in PV systems (Drews et al., 2007).

In addition to satellite derived GHI estimates, one may have access to ground sensors that provide more accurate GHI measurements, but are often sparsely distributed. We present a method that combines the broad areal coverage of satellite derived GHI with the accurate point measurements from ground sensors in order to provide more accurate GHI estimates for city-scale areas.

Similar techniques have used ground measurements to improve satellite derived irradiance estimates in the context of improving daily (or longer) irradiance estimates. Much of this work studies

so called site adaptation techniques with the goal of improving multi-year satellite irradiance estimates using a limited measurement campaign from ground sensors (Polo et al., 2016). A number of studies use Kriging methods that rely on spatial interpolation of the ground data along with satellite derived estimates (D'Agostino and Zelenka, 1992; Journée et al., 2012; Frei et al., 2015). Others use linear bias corrections (Polo et al., 2015), polynomial bias corrections (Mieslinger et al., 2014), or apply a polynomial to correct the satellite cumulative distribution function (Schumann et al., 2011). Ruiz-Arias et al. (2015) used optimal interpolation (OI) with numerical weather prediction solar radiation data and monthly-averaged daily GHI values from ground sensors.

OI is a Bayesian technique often used in geophysics, in particular numerical weather prediction, to combine models and observations. OI is mathematically equivalent to 3D variational methods, Kriging, and Gaussian process regression (Low et al., 2015). OI and 3D variational techniques are often used in the field of meteorology, Kriging is used in the context of geostatistics, and one often encounters Gaussian process regression in the context of machine learning. Thus, each method seeks a solution with the approach and quantities, like covariances, appropriate for each context.

In the context of this study, the satellite derived GHI estimates represent the model and the ground sensor data are the observations for OI. We focus on improvements to GHI estimates from a single satellite image using OI rather than improving the

* Corresponding author.

E-mail address: atlorenzo@email.arizona.edu (A.T. Lorenzo).

multi-year satellite estimates. This single satellite image will be used to nowcast DG production and to produce forecasts. We also present a novel method to parameterize the correlation between satellite pixels using the relative cloudiness between them.

We describe the satellite derived irradiance models and observation data in Section 2, the OI method in Section 3, and three ways to estimate covariances between locations in Section 4. These covariances are critical to the success or failure of OI. A method to correct for satellite geolocation errors is described in Section 5, and parameter tuning is detailed in Section 6. We present and discuss the results of applying OI to Tucson, AZ in Section 7. Finally, a summary of the work is provided in Section 8.

2. Models and observations

2.1. Satellite derived irradiance models

To investigate how well OI works with different types of prior information, we use two different models to convert satellite images to GHI maps. The resulting GHI maps are called the “background” or “prior” in OI and will be denoted by \mathbf{x}_b . Both models use images from the GOES-W geostationary satellite that cover the city of Tucson, AZ (roughly 75×80 km). An example of a visible albedo image derived from the visible channel of GOES-W is shown in Fig. 1.

One of the models is a physical model called the University of Arizona Solar Irradiance Based on Satellite (UASIBS) model (Kim et al., 2016). UASIBS uses the visible and infrared images from the GOES-W satellite to generate a cloud mask. Then, parameterized cloud properties determined from the infrared images are used in a radiative transfer model to determine the surface GHI. This GHI estimate has the same resolution as the visible channel of the GOES-W satellite (approximately 1 km).

The second model is a semi-empirical model, which we refer to as the SE model. This model is based on the SUNY model which applies a regression to the visible channel of the GOES-W satellite (Perez et al., 2002). The only differences between our SE model and the SUNY model are that the dynamic range is set with the 3 months of data used in this study instead of the recommended 60 day window with seasonal corrections and that the specular correction factor was neglected.

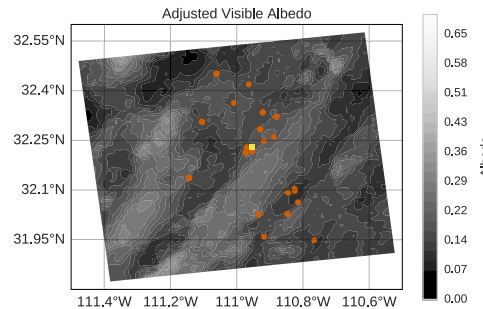


Fig. 1. Visible albedo image derived from the visible channel of the GOES-W satellite. Lighter colors indicate cloudier areas. The orange dots represent the locations of the sensors used in this study which includes both irradiance sensors and rooftop PV systems as described in Section 2.2. The yellow square in the center indicates the location of a calibrated GHI sensor on the University of Arizona campus. The image covers an area of roughly 75×80 km over Tucson, AZ. (For interpretation of the references to color in this figure legend, the reader is referred to the web version of this article.)

To remove effects of the diurnal cycle and ease incorporation of data from rooftop PV systems, all images were converted into clear-sky index images by dividing the estimated GHI by a clear-sky GHI estimate. The resulting values of clear-sky index range from nearly 0 for an overcast sky to 1 for a cloud-free sky. These conversion algorithms do not take into account image timestamp inaccuracies or satellite geolocation errors, but corrections for those errors will be discussed in Section 5.

2.2. Ground observations

The observation data are collected from 22 sensors including a calibrated NREL MIDC sensor (Wilcox and Andreas, 2010), custom irradiance sensors (Lorenzo et al., 2014), and data from rooftop PV systems. The sensor locations are indicated by orange circles in Fig. 1.

Irradiance observations were averaged to 5 min to match PV data that are reported as 5 min averages. This averaging is consistent with the inherent averaging due to the satellite spatial resolution. We note that all data sources (ground sensors and satellite images) are available in near real-time so that the OI corrected GHI images can be used as a basis for forecasts or DG nowcasts.

All data were converted to clear-sky index data using clear-sky expectations for each sensor. To produce the clear-sky expectation for one day, the measurements from preceding clear days within one week are averaged to produce an initial estimate. This initial estimate is then scaled to match the clear times on the day of interest to account for differences in turbidity or temperature. This method simplifies the calculation of clear-sky expectations for the rooftop PV systems because no parameters about the system (directional response, peak power) are assumed. The clear-sky expectations and clear-sky index data was inspected manually to confirm the quality. Note that the ground observation data may experience cloud enhancement events which lead to clear-sky indices greater than 1.

We restrict our data and analysis to solar zenith angles less than 60° . At times, we also withhold sensors from the OI routine and use these sensors to validate how well OI performs for other locations in the image besides the input sensor locations.

2.3. Data set description

About 1300 satellite images collected over April, May, and June 2014 were converted to irradiance images with the two models and paired with the corresponding ground observations. We randomly divide the data set into a training set with 437 images (252 clear and 185 cloudy images) and a verification set of 874 images (504 clear and 370 cloudy images). The training set is used to tune parameters for OI as described in Section 6. The verification set is used for error analysis and to draw conclusions about OI.

The distinction between clear and cloudy satellite images will become important in Section 3 for determining sensor error variances. Clear times are identified using a combination of the UASIBS estimates and the ground sensor data. Specifically, if the minimum value of a UASIBS clear-sky index image is greater than 0.8, the mean of the image is greater than 0.99, and the second largest deviation from 1 of any of the ground observations is less than 0.05, then we classify the image as clear. This procedure accurately identifies times at which no clouds exist in the area of study. Other methods can also be used to perform this classification (Reno and Hansen, 2016; Escrig et al., 2013; Ghonima et al., 2012), but our simple method is sufficient for our purposes.

3. Optimal interpolation

We now describe the OI method. Under wide assumptions, OI is optimal in the sense that it is the best linear, unbiased estimator of a field. Further detail can be found in data assimilation textbooks, e.g. Kalnay (2003).

The result of the OI routine, known as the analysis, \mathbf{x}_a , is a vector that is produced by computing a weighted sum of the background (or prior information), \mathbf{x}_b , and a correction vector (or “innovation” in OI) that depends on the measurements, \mathbf{y} :

$$\mathbf{x}_a = \mathbf{x}_b + \mathbf{W}(\mathbf{y} - \mathbf{H}\mathbf{x}_b). \quad (1)$$

As discussed in Section 2.1, the N satellite derived clear-sky indices from one image are represented as the background vector, \mathbf{x}_b . The measurement vector, \mathbf{y} , is a vector of length M of clear-sky indices generated from M ground irradiance sensor and rooftop PV power data observations as discussed in Section 2.2. The observation matrix, \mathbf{H} , is an $M \times N$ matrix that maps points in the background space to points in the observation space. We construct \mathbf{H} using the nearest neighbor approach of selecting the satellite pixels that are closest to the observation locations. Another possible approach is to average the points in the background that are within a given radius of each sensor location. Furthermore, \mathbf{H} can contain conversion factors to convert the units of \mathbf{x}_b to the units of \mathbf{y} . In our case however, \mathbf{H} is unitless because \mathbf{y} and \mathbf{x}_b are both in units of clear-sky index. Example background and analysis images for the UASIBS and SE models are shown in Fig. 2.

The weight matrix, \mathbf{W} , is an $N \times M$ matrix constructed from the error covariance matrices of the background, \mathbf{P} , and the observations, \mathbf{R} , as

$$\mathbf{W} = \mathbf{PH}^T(\mathbf{R} + \mathbf{PHP}^T)^{-1}. \quad (2)$$

Choosing these error covariance matrices must be done with care: they define how information is transferred from sensor locations to other locations in the satellite image, and how much weight is given to any one sensor or satellite pixel.

\mathbf{R} is defined as the error covariance matrix of the observations such that

$$\mathbf{y} = \mathbf{y}_t + \mathbf{e}, \quad \mathbf{e} \sim N(\mathbf{0}, \mathbf{R}) \quad (3)$$

where \mathbf{y}_t is the true value of the observation and \mathbf{e} is a random vector sampled from a multivariate normal distribution with mean 0 and covariance \mathbf{R} . On clear days, we assume the true clear-sky index values are 1.0. We also assume that the measurements are unbiased and that the correlations in the errors between sensors is negligible, so \mathbf{R} is a diagonal matrix in our case. Thus, we estimate the diagonal elements (sensor error variances) by computing the variance on a set of clear days in the training data set for each sensor individually. Furthermore, we restrict the minimum variance to be 0.001 or about a 3% clear-sky index RMS error to avoid exact interpolation at sensor locations. With \mathbf{R} calculated from the ground sensor data, we describe various ways to parameterize \mathbf{P} next.

4. Covariance parameterization and correlation structure

Choosing an appropriate background error covariance matrix is an important step in the OI method for this application and determines how well OI performs. The background error covariance matrix, \mathbf{P} , defines how information is transferred from sensor

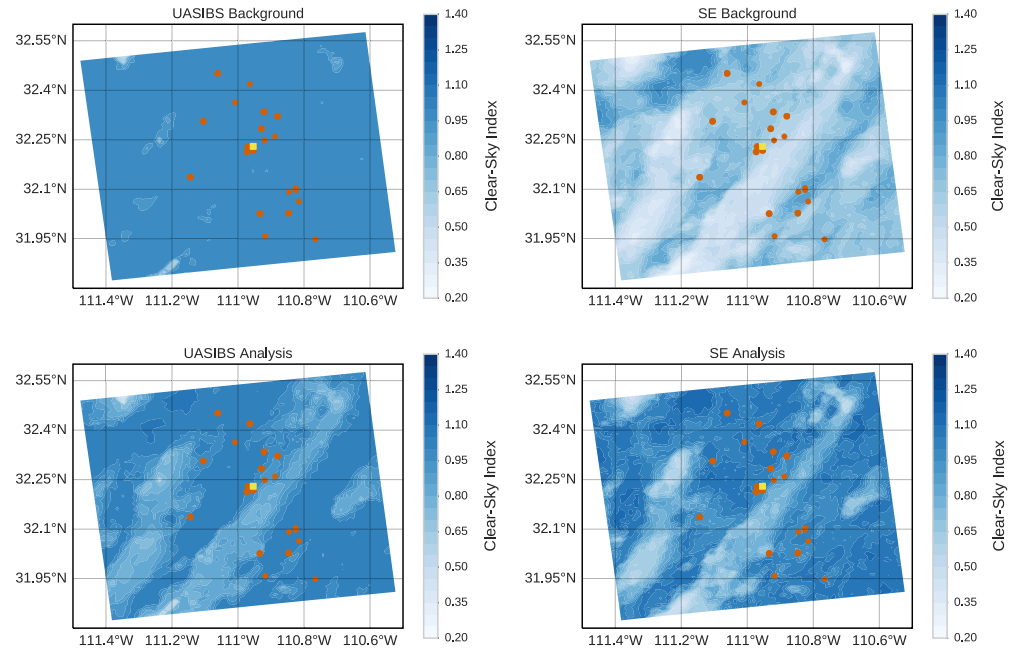


Fig. 2. Example background (top row) and analysis (bottom row) clear-sky index images using the UASIBS (left column) and SE (right column) satellite image to ground irradiance models applied to the visible satellite image shown in Fig. 1. Note that in this case, UASIBS failed to produce many clouds. OI adds clouds to the analysis and also makes the darker, clear areas even more clear. In this case, the SE model overproduces clouds. OI reduces the cloud amount while keeping clouds in suitable locations.

observation locations to locations throughout the background image. Similar to \mathbf{R} , \mathbf{P} is defined such that

$$\mathbf{x}_b = \mathbf{x}_t + \mathbf{g}, \quad \mathbf{g} \sim N(\mathbf{0}, \mathbf{P}) \quad (4)$$

where \mathbf{x}_t is the “true” value of the satellite derived clear-sky index image and \mathbf{g} is a random vector sampled from a multivariate normal distribution with mean 0 and covariance \mathbf{P} .

We will now describe three methods to calculate \mathbf{P} :

1. *Empirical*: \mathbf{P} calculated empirically from all of the background images,
2. *Spatial*: \mathbf{P} with correlations parameterized based on the physical distance between pixels, and
3. *Cloudiness*: \mathbf{P} with correlations parameterized based on the difference in cloudiness between each pixel.

4.1. Empirical covariance

The empirical \mathbf{P} is calculated by assuming that satellite-derived clear-sky index images are sampled from the same multivariate normal distribution and then simply computing the covariance using all images in the training data set. This assumption is likely invalid given the high probability of clear days leading to a non-Gaussian distribution. An analysis computed with this type of \mathbf{P} gives non-physical results, as described in Section 7, but is included for comparison.

4.2. Correlation matrix parameterization

Before describing spatial and cloudiness covariances, it is useful to decompose \mathbf{P} into a diagonal variance matrix, \mathbf{D} , and a correlation matrix, \mathbf{C} as

$$\mathbf{P} = \mathbf{D}^{1/2} \mathbf{C} \mathbf{D}^{1/2}. \quad (5)$$

Here, \mathbf{D} sets the scale of the errors while \mathbf{C} describes how errors and information spread. We obtain \mathbf{D} in a similar manner as we do for \mathbf{R} , we use a number of clear images from the training data set to estimate the variance of each pixel in the background individually. The errors in \mathbf{x}_b come mainly from the satellite image to ground irradiance conversion that often exhibits large differences in error between clear and cloudy images. Thus, we allow for a tunable scaling factor, d , in the construction of \mathbf{D} for cloudy images to account for possible model error differences between clear and cloudy skies so that

$$\mathbf{D} = d\mathbf{D}' \quad (6)$$

where \mathbf{D}' is the variance estimated from the clear images.

The correlation matrix \mathbf{C} defines how information is transferred from the sensor locations to other locations in the satellite estimate. \mathbf{C} can be parameterized based on the spatial distance between points in the background as in Ruiz-Arias et al. (2015) or, as we demonstrate, one might rely on information in the current satellite image, such as cloudiness.

To construct the elements of \mathbf{C} , c_{ij} , we apply a correlation function, k , to the distance metric r computed between each pixel i and j

$$c_{ij} = k(r_{ij}). \quad (7)$$

Any number of covariance functions, k , can be chosen; see Rasmussen and Williams (2005) for a partial list. We chose to study a piece-wise linear correlation function

$$k(r) = \begin{cases} 1 - \frac{r}{l} & r < l \\ 0 & r \geq l \end{cases} \quad (8)$$

an exponential correlation function

$$k(r) = \exp\left(-\frac{r}{l}\right), \quad (9)$$

and a square exponential correlation function

$$k(r) = \exp\left(-\frac{r^2}{l^2}\right). \quad (10)$$

For each correlation function, l is a characteristic length that we tune with a training data set for each choice of k to minimize error as described later in Section 6.

4.3. Spatial covariance

The distance metric for the spatial correlation parameterization is the standard Euclidean distance (once locations are mapped to a two dimensional plane using a map projection),

$$r_{ij} = \sqrt{(x_i - x_j)^2 + (y_i - y_j)^2}. \quad (11)$$

Thus, the spatial covariance \mathbf{P} is constructed by applying Eqs. (5)–(7) and (11) with a tuned k , l , and d as described in Section 6.

4.4. Cloudiness covariance

For what we call cloudiness covariance, we parameterize \mathbf{C} based on the difference in cloudiness in the visible satellite image. This corresponds to only adjusting the cloudy areas with observations that are experiencing similarly cloudy sky and leaving the clear areas to be adjusted by observations of the clear sky. This adjustment is made without consideration of the spatial distance between pixels. We use the adjusted visible albedo calculated from the visible satellite image rather than the processed clear-sky index maps to compute the correlation. This avoids cloud representation errors that may arise in the satellite to irradiance conversion; for example, note how UASIBS fails to produce clouds in many areas of Fig. 2. Also note that because this parameterization depends on the visible satellite image, \mathbf{C} and subsequently \mathbf{P} are calculated for each image individually.

To calculate the adjusted visible albedo, we convert the visible brightness counts from the satellite, b_i , to visible albedo and divide by the cosine of the solar zenith angle, ϕ , to correct for the time of day:

$$v_i = \left(\frac{b_i}{255}\right)^2 / \cos(\phi_i). \quad (12)$$

An example of this adjusted visible albedo is shown in Fig. 1. We also remove the constant (over the three months we studied) background albedo that is due to the land surface. This background is calculated as the average of the adjusted visible albedo on clear days in the training set so that

$$z_i = v_i - \bar{v}_i^{\text{clear}} \quad (13)$$

The distance metric for the cloudiness correlation parameterization is the absolute value of the difference between pixel values of the adjusted visible albedo image (with the land surface background removed):

$$r_{ij} = |z_i - z_j|. \quad (14)$$

Thus, the cloudiness covariance \mathbf{P} is constructed by applying Eqs. (5)–(7) and (12)–(14) with a tuned k , l , and d for each individual satellite image.

4.5. OI summary

In summary, to perform OI, one must first collect background, \mathbf{x}_b , and observation, \mathbf{y} , data. Then define observation error covari-

ances, \mathbf{R} , from the observation data and define the background error covariances, \mathbf{P} , either empirically or by following the above procedure after choosing a distance metric r , the correlation function k , the correlation length l , and the scaling factor d using Eqs. (5)–(7). Finally, Eqs. (1) and (2) can be used to compute the analysis, \mathbf{x}_a .

5. Geolocation correction

It is important to consider errors in the tagged location for each satellite pixel compared to the ground sensors and the time-stamp of the image. Furthermore, one must take into account the position of the sun in order to predict the cloud shadow location on the ground. If this cloud shadow location is inaccurate, the optimal interpolation routine may perform poorly, or worse, may invert the cloudy and clear areas of the images. Examples of an inverted analysis and the corrected analysis once these position adjustments are taken into account are shown in Fig. 3.

The first geolocation issue is called parallax, which is the discrepancy between the actual location and the location tagged by a satellite due to the satellite viewing the scene at an angle (Vicente et al., 2010). The GOES-W satellite is located at 135°W on the equator while Tucson, AZ is at roughly 32°N and 110°W. The satellite tags the location of each pixel as if it were at the surface. This means, for our region, that a cloud obscures a pixel that is to the NE of the cloud. Thus, the actual location of the cloud is to the SW of what the satellite tags the pixel as.

Another source of error is a timing issue that arises because the satellite tags each image with a single time, however it may take

the satellite 30 min to sweep and capture that image. Thus, there is uncertainty in the time that any part of the image was captured.

Estimating where the cloud shadow falls on the surface due to solar position effects is the final geolocation issue we take into account. If the shape and height of the clouds is known, the correction for both parallax and solar position is a simple geometry problem. However, cloud shape and height are difficult to determine with sufficient accuracy, and we rely only on an estimate of the height of the top of the clouds and ignore the vertical thickness. We also assume that the cloud height is uniform in one image.

Given these limitations, we use a simple strategy to correct for geolocation errors. We find a single optimal cloud height by minimizing the mean squared error (MSE) between the OI analysis and sensors that are not used to perform OI. The sensors not used are the same cross-validation sensors we will discuss next. We perform this correction using a grid search for cloud heights ranging from 0 to 14 km and we shift the entire background image based on that height, perform OI, then calculate the MSE. Once the height that minimizes MSE is found, we perform OI again on the shifted background image and save the analysis as our result for the given time. This technique assumes that there is a single cloud layer, which is not always the case and can be improved in the future.

6. Tuning OI to a specific location

As discussed in Section 4.2, k , l , and d are tunable parameters that determine how information is spread through the image. In order to find suitable values of these parameters, we split the satellite images into a training and a verification set as described

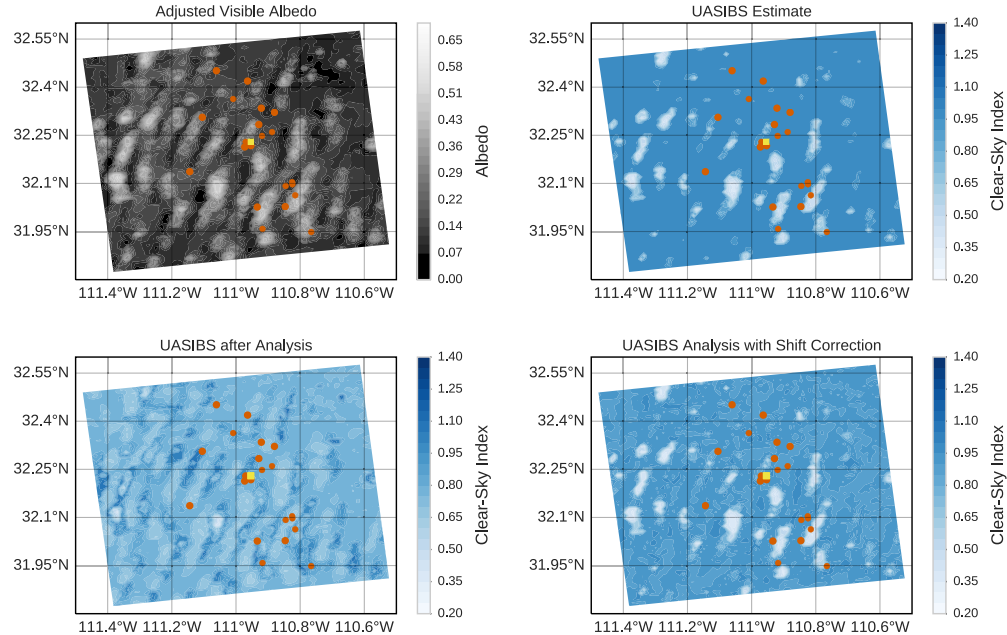


Fig. 3. An example of a time when errors in geolocation of the satellite image result in an analysis that is inconsistent with the actual satellite image. The background estimate in this case (upper right) agrees well with the visible satellite image (upper left). However, after performing OI, the analysis (lower left) has clouds in areas that should be clear according to the visible image and sometimes makes areas that should have clouds clear. After shifting the background image slightly, OI produces an analysis (lower right) that is consistent with the visible image.

in Section 2.3, and tuning is only performed with the training set. Furthermore, we perform a six fold cross-validation over the sensors in order to validate the model at locations not included in the OI calculation. We then perform a grid search through the parameter space and define the optimal parameters as those that give the lowest mean (over the cross-validation sets) MSE of the withheld sensors. This tuning is performed for both spatial and

cloudiness correlation parameterizations and for both the SE and UASIBS models.

The optimal parameters for the UASIBS and SE models using both cloudiness and spatial covariances computed only using the training data are presented in Table 1. We note that these parameters are optimal for Tucson, AZ. Other areas, sensors, or study periods may require a different parameterization of the error covariances.

Table 1

Optimal parameters for the UASIBS and SE models for both cloudiness and spatial covariances. l has units of adjusted visible albedo for cloudiness covariances and units of kilometers for spatial covariances.

		d	l	k
UASIBS	Cloudiness	156	0.2	Linear
	Spatial	225	20	Exp.
SE	Cloudiness	1.56	0.6	Exp.
	Spatial	0.25	100	Exp.

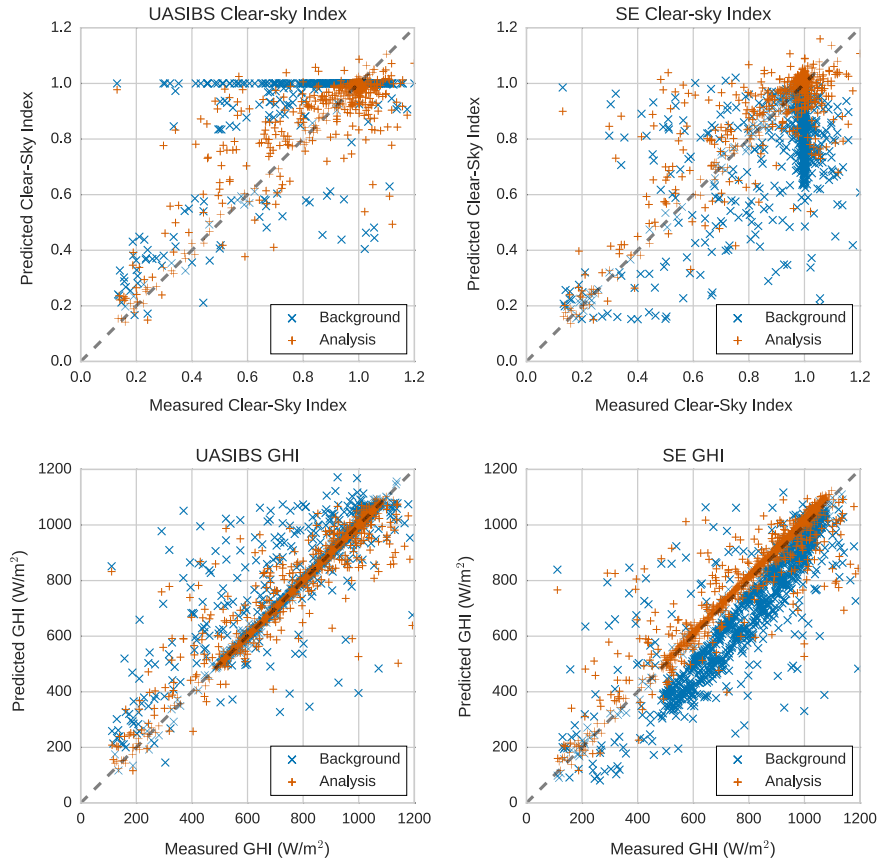


Fig. 4. Scatter plots of predicted versus measured clear-sky index (top row) and GHI (bottom row) for the calibrated NREL MIDC GHI sensor on the University of Arizona campus for both the UASIBS model (left column) and SE model (right column). The analysis was computed using cloudiness covariance, the optimal parameters listed in Table 1, and the verification data set. Data from the background images is plotted as blue 'x's and data from the OI analysis is plotted as orange '+'s. GHI is computed by multiplying clear-sky indices and an appropriate clear-sky profile. In each case, we see that the analysis values are more tightly scattered around the dashed $y = x$ line. Also notice that the UASIBS model does not predict clear-sky index values from roughly 0.6 to 0.8 but that the analysis does move some values into this range. (For interpretation of the references to color in this figure legend, the reader is referred to the web version of this article.)

In general, the minimum MSE is sensitive to the parameter choice with the most sensitivity shown for l and least sensitivity for k . A small change in l (0.1 for cloudiness and 10 km for spatial) typically degrades the MSE by 10% or more. One exception is the combination of the SE model and spatial covariance which produce MSE surfaces that are less sensitive to a range of parameters, for example a 40 km difference in l only raises the MSE by 10%.

Large d values for the UASIBS model indicate that the estimated variance from only the clear days is too low. This is because UASIBS suppresses many clouds or slight variations on clear days. An example of this on a cloudy day is shown in Fig. 2. A value of $d < 1$ for the SE model indicates that the model tends to overestimate the variance on cloudy days as a result of the tendency to overproduce clouds even at times that should be clear.

Our proposed tuning process is computationally intensive but manageable; computation for one set of (k, l, d) and one cross-validation set using 24 cores of two Intel Xeon E5-2690 v3 processors takes nearly 10 min. Thus, to tune over the six cross-validation sets, three choices of k , ten choices of both l and d , spatial and cloudiness correlation parameterizations, and the SE and UASIBS models would take nearly 7 weeks on a single 24 core machine. It would take a typical 4 core laptop or desktop nearly a year to perform the same tuning. To speed up this tuning, the bulk of the operations were converted to GPU code which decreased the run-time for a single parameter set over the test data to 5 min using a single GPU. We used the University of Arizona's El Gato supercomputer, which has 140 NVIDIA K20x GPUs, to perform the tuning in a matter of days. Once tuning is complete, OI can be computed in under five seconds for each image.

7. Results and discussion

We compute the OI analysis on each of the images in the verification data set using optimal parameters found in Section 6. First, we compute the analysis of the verification data by only withholding the NREL MIDC GHI sensor at the University of Arizona, and later we calculate errors while performing six fold cross-validation over the sensors.

Scatter plots of predicted versus measured values at the NREL MIDC sensor using cloudiness covariance are shown in Fig. 4. In the clear-sky index scatter plots, we see that the UASIBS model under-predicts clouds while the SE model over-predicts clouds. It is interesting to note that the UASIBS model does not predict clear-sky index values between 0.6 and 0.8, and that OI helps to fill in this gap. The GHI scatter plots show that the analysis performs well and is more tightly scattered around the $y = x$ line with minimal bias. It is especially striking to note how well OI improves the GHI estimates for the SE model. Figs. 2 and 4 also demonstrate that OI is not simply a bias correction applied to the whole background because the analysis is not a linear (or even polynomial) function applied to the background values. This is especially evident in the scatter plot of GHI for the SE model (lower right of Fig. 4).

We compute the mean bias error (MBE), mean absolute error (MAE), and root mean squared error (RMSE) over the verification data with 5 min average sensor data and "instantaneous" satellite estimates. For RMSE, the square root is computed after all averaging computations. The errors in GHI when only the NREL MIDC sensor was withheld from the OI routine and converting clear-sky index to GHI using the sensor's clear-sky profile are shown in Table 2.

To calculate the errors over the cross-validation sensors in order to validate OI at locations not included in the algorithm, we averaged over the withheld sensors, the cross-validation runs, and the verification images. Fig. 5 shows the reduction in errors for the UASIBS and SE models using cloudiness covariance for the analysis

Table 2

Error statistics for the NREL MIDC sensor on the University of Arizona campus. The analysis was computed with only the MIDC sensor withheld and averaged over the verification data set, and cloudiness covariance was used. Both the UASIBS and SE models show improvements and have a similar analysis RMSE. Units are W/m^2 .

	MBE	MAE	RMSE
UASIBS analysis	4.16	27.2	71.1
UASIBS background	20.7	38.8	98.8
SE analysis	11.2	36.0	72.7
SE background	-86.1	107	140

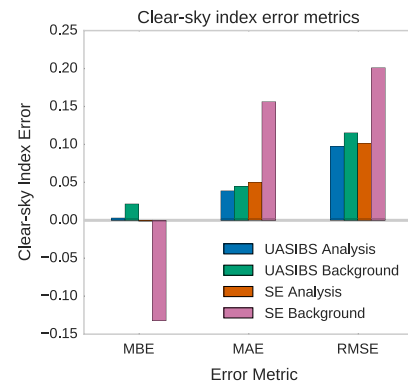


Fig. 5. Clear-sky index cross-validation error statistics for the UASIBS and SE models before (background) and after (analysis) performing OI using cloudiness covariance with the optimal parameters listed in Table 1. The error statistics were computed by averaging over the withheld sensors, the cross-validation runs, and the verification times. The SE model initially has a large bias that is corrected by the analysis. After analysis, both the UASIBS and SE models have similar RMSE.

errors as compared to the background errors. Table 3 presents the errors for the background and analysis computed with each covariance method for the UASIBS and SE models, respectively. Analyzing Figs. 4 and 5 and Tables 2 and 3, we see that the SE model initially has a large bias that is corrected in the analysis. This also leads to large MAE and RMSE relative improvements of 68% and 50%, respectively. The analysis using the best covariance parameterization for UASIBS had a RMSE relative improvement of 16%.

Furthermore, it is interesting to see that the errors after optimal interpolation are similar for both the UASIBS and SE models. We interpret this as evidence that one can use the relatively simple

Table 3

Clear-sky index error statistics using the UASIBS and SE models with cloudiness, spatial, or empirical covariance parameterizations. Errors are calculated by averaging over the withheld sensors, cross-validation runs, and verification images. OI using any of the covariance methods improves upon the background for both models. All errors are in units of clear-sky index.

	MBE	MAE	RMSE
<i>UASIBS model</i>			
Cloudiness analysis	0.003	0.039	0.097
Spatial analysis	0.004	0.038	0.099
Empirical analysis	0.000	0.043	0.105
Background	0.022	0.045	0.115
<i>SE model</i>			
Cloudiness analysis	-0.001	0.050	0.102
Spatial analysis	-0.005	0.051	0.105
Empirical analysis	-0.001	0.051	0.106
Background	-0.132	0.156	0.201

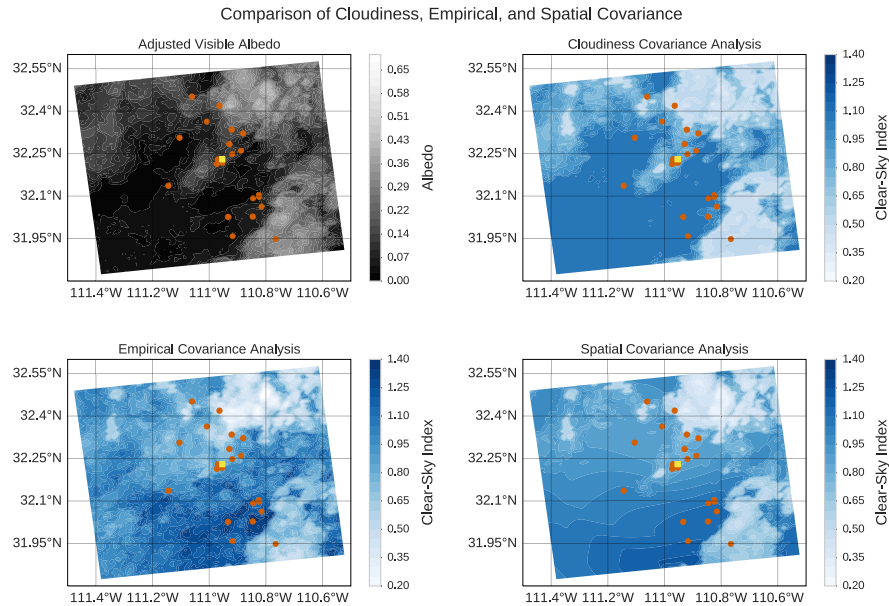


Fig. 6. Example of OI using empirical, spatial, and cloudiness covariance with the UASIBS model. The upper left shows the visible image taken from the satellite with the surface albedo removed. The upper right shows the analysis using cloudiness covariance that generally agrees with the visible albedo image. The analysis computed with an empirical covariance matrix (bottom left) generates clouds in the lower left of the image that are not present in the visible albedo image. The spatial covariance analysis (bottom right) shows a smoothly varying and thin “background cloud” that is inconsistent with the visible albedo image.

semi-empirical model with optimal interpolation and still obtain irradiance estimates that are comparable in quality to estimates from more complicated, physics-based models. This also suggests that the optimal interpolation routine that we have presented is likely to work with satellite image to irradiance models that were not studied here.

OI assumes that the background error is unbiased and Gaussian as described in Eq. (4). However, it is clear from Fig. 5 that the SE background is biased. From Fig. 4, it also appears that the UASIBS background is not Gaussian. Thus, we cannot assume that this application of OI yielded the best linear unbiased estimate, but we show that OI still produces measurable improvements.

The results in Table 3 indicate that any of the three methods to compute the background error covariance matrix produce an analysis that improves upon the background. However, when we subjectively compare the analysis of the covariance models, as in Fig. 6, we see that analysis using the cloudiness covariance method better represents the cloud pattern depicted in the visible satellite image. Clouds produced using the spatial and empirical covariance methods are physically inconsistent with the clouds depicted in the visible albedo image. For example, the lower left corner of the images in Fig. 6 should have no clouds present according to the visible albedo image, but the empirical covariance analysis has clouds present in that region. The analysis produced using spatial covariance shows a thin and smoothly varying “background cloud” that is simply not observed in the visible albedo image. Furthermore, the cloudiness covariance parameterization is calculated for each satellite image individually which likely leads to a better modeling of the spatial heterogeneity of irradiance. Thus, we recommend the cloudiness covariance parameterization as the method of choice, but additional verification sensors evenly dis-

tributed throughout the study area may help to better distinguish the parameterizations through objective measures.

8. Conclusions

We presented an application of optimal interpolation that combines ground irradiance sensor data with a satellite derived estimate of irradiance. We systematically analyzed three methods to choose an error covariance matrix for the satellite derived GHI estimates. This covariance matrix is critical to the success of OI. We observed the best results by assigning covariances based on the differences in cloudiness rather than spatial or empirical covariances. Our implementation of OI was trained and evaluated using three months of data in Tucson, AZ. We tuned the model parameters over one-third of the data, and presented the results of OI over the remaining two-thirds.

The results show that OI improves the entire satellite derived irradiance field with data from only a small number of point locations. Furthermore, the success of OI with different satellite derived irradiance models indicates that OI is likely applicable to satellite derived irradiance models not described in this paper.

In future work, we wish to study if OI is applicable to larger areas than the city scale studied here. If, for example, clouds form because of the same physical forcings, OI using cloudiness covariance may be able to use sensors in Tucson to improve irradiance estimates 100 miles away in Phoenix. Furthermore, OI as described in this paper can be extended to a Kalman filter with the use of a cloud advection model. This allows forecasts to be made that also incorporate previous satellite and ground sensor data instead of relying on a single snapshot in time.

Conflict of interest

The authors have no conflicts of interest to report.

Supplementary material

Location metadata, measurements, clear-sky expectations, and the satellite data used in this study have been released online under the CC0 1.0 license (Lorenzo and Cronin, 2016). The code to generate the optimal interpolation analysis is released under the MIT license (Lorenzo, 2016).

Acknowledgments

This project was funded in part by Tucson Electric Power and Arizona Public Service. We thank Technicians for Sustainability, a local solar PV installer, for providing data from rooftop PV systems. ATL thanks the University of Arizona Renewable Energy Network for support. WFH thanks the Department of Energy (DOE) Office of Energy Efficiency and Renewable Energy (EERE) Postdoctoral Research Award for support. This material is based upon work performed on the El Gato supercomputer supported by the National Science Foundation under Grant No. 1228509. This material is based upon work supported by the National Science Foundation under Grant No. 1619630.

References

- D'Agostino, V., Zelenka, A., 1992. Supplementing solar radiation network data by co-Kriging with satellite images. *Int. J. Climatol.* 12 (7), 749–761. <http://dx.doi.org/10.1002/joc.3370120707>.
- Drews, A., de Keizer, A., Beyer, H., Lorenz, E., Betscke, J., van Sark, W., Heydenreich, W., Wiemken, E., Stettler, S., Toggweiler, P., Bofinger, S., Schneider, M., Heilscher, G., Heinemann, D., 2007. Monitoring and remote failure detection of grid-connected PV systems based on satellite observations. *Sol. Energy* 81 (4), 548–564. <http://dx.doi.org/10.1016/j.solener.2006.06.019>.
- Escrí, H., Battlés, F., Alonso, J., Baena, F., Bosch, J., Salbidegoitia, I., Burgaleta, J., 2013. Cloud detection, classification and motion estimation using geostationary satellite imagery for cloud cover forecast. *Energy* 55, 853–859. <http://dx.doi.org/10.1016/j.energy.2013.01.054>.
- Frei, C., Willi, M., Stöckli, R., Dürr, B., 2015. Spatial analysis of sunshine duration in complex terrain by non-contemporaneous combination of station and satellite data. *Int. J. Climatol.* 35 (15), 4771–4790. <http://dx.doi.org/10.1002/joc.4322>.
- Ghonima, M.S., Urquhart, B., Chow, C.W., Shields, J.E., Cazorla, A., Kleissl, J., 2012. A method for cloud detection and opacity classification based on ground based sky imagery. *Atmos. Meas. Tech.* 5 (11), 2881–2892. <http://dx.doi.org/10.5194/amt-5-2881-2012>.
- Journéa, M., Müller, R., Bertrand, C., 2012. Solar resource assessment in the Benelux by merging Meteosat-derived climate data and ground measurements. *Sol. Energy* 86 (12), 3561–3574. <http://dx.doi.org/10.1016/j.solener.2012.06.023>.
- Kalnay, E., 2003. *Atmospheric Modeling, Data Assimilation and Predictability*. Cambridge University Press.
- Kim, C.K., Holmgren, W.F., Stovern, M., Betterton, E.A., 2016. Toward improved solar irradiance forecasts: derivation of downwelling surface shortwave radiation in arizona from satellite. *Pure Appl. Geophys.* <http://dx.doi.org/10.1007/s00024-016-1302-3>.
- Kühnert, J., Lorenz, E., Heinemann, D., 2013. Satellite-based irradiance and power forecasting for the German energy market. In: Kleissl, J. (Ed.), *Solar Energy Forecasting and Resource Assessment*. Elsevier, pp. 267–297. <http://dx.doi.org/10.1016/B978-0-12-397177-7.00011-5> (Chapter 11).
- Lorenzo, A.T., 2016. alorenzo175/satellite_irradiance_optimal_interpolation: Final Research Code. <http://dx.doi.org/10.5281/zenodo.166799>.
- Lorenzo, A.T., Cronin, A.D., 2016. Irradiance Measurements, Satellite Images, and Clear-sky Expectations for Spring 2014 in Tucson, AZ. <http://dx.doi.org/10.5281/zenodo.166799>.
- Lorenzo, A.T., Holmgren, W.F., Leuthold, M., Kim, C.K., Cronin, A.D., Betterton, E.A., 2014. Short-term PV power forecasts based on a real-time irradiance monitoring network. In: 2014 IEEE 40th Photovoltaic Specialist Conference (PVSC), pp. 0075–0079. <http://dx.doi.org/10.1109/PVSC.2014.6925212>.
- Low, K.H., Chen, J., Hoang, T.N., Xu, N., Jailllet, P., 2015. Recent Advances in Scaling Up Gaussian Process Predictive Models for Large Spatiotemporal Data. Springer International Publishing, pp. 167–181. http://dx.doi.org/10.1007/978-3-319-25138-7_16.
- Mieslinger, T., Ament, F., Chhatbar, K., Meyer, R., 2014. A new method for fusion of measured and model-derived solar radiation time-series. *Energy Procedia* 48, 1617–1626. <http://dx.doi.org/10.1016/j.egypro.2014.02.182>.
- Perez, R., Ineichen, P., Moore, K., Kmiecik, M., Chain, C., George, R., Vignola, F., 2002. A new operational model for satellite-derived irradiances: description and validation. *Sol. Energy* 73 (5), 307–317. [http://dx.doi.org/10.1016/S0038-092X\(02\)00122-6](http://dx.doi.org/10.1016/S0038-092X(02)00122-6).
- Polo, J., Martin, L., Vindel, J., 2015. Correcting satellite derived DNI with systematic and seasonal deviations: application to India. *Renew. Energy* 80, 238–243. <http://dx.doi.org/10.1016/j.renene.2015.02.031>.
- Polo, J., Wilbert, S., Ruiz-Arias, J., Meyer, R., Gueymard, C., Suri, M., Martin, L., Mieslinger, T., Blanc, P., Grant, I., Boland, J., Ineichen, P., Remund, J., Escobar, R., Troccoli, A., Sengupta, M., Nielsen, K., Renne, D., Geuder, N., Cebeaucer, T., 2016. Preliminary survey on site-adaptation techniques for satellite-derived and reanalysis solar radiation datasets. *Sol. Energy* 132, 25–37. <http://dx.doi.org/10.1016/j.solener.2016.03.019>.
- Rasmussen, C., Williams, C., 2005. Covariance functions. In: *Gaussian Processes for Machine Learning*. MIT Press, pp. 79–104 (Chapter 4).
- Reno, M.J., Hansen, C.W., 2016. Identification of periods of clear sky irradiance in time series of GHI measurements. *Renew. Energy* 90, 520–531. <http://dx.doi.org/10.1016/j.renene.2015.12.031>.
- Ruiz-Arias, J.A., Quesada-Ruiz, S., Fernández, E.F., Gueymard, C.A., 2015. Optimal combination of gridded and ground-observed solar radiation data for regional solar resource assessment. *Sol. Energy* 112, 411–424. <http://dx.doi.org/10.1016/j.solener.2014.12.011>.
- Saint-Drenan, Y.-M., Bofinger, S., Rohrig, K., Ernst, B., 2011. Regional nowcasting of the solar power production with PV-plant measurements and satellite images. In: Proceedings of the ISES Solar World Congress 2011. International Solar Energy Society, Freiburg, Germany, pp. 1–11. <http://dx.doi.org/10.18086/swc.2011.11.09>.
- Schumann, C., Beyer, H.G., Meyer, R., Chhatbar, K., 2011. Improving satellite-derived solar resource analysis with parallel ground-based measurements. In: Proceedings of the ISES Solar World Congress 2011. International Solar Energy Society, Freiburg, Germany, pp. 1–12. <http://dx.doi.org/10.18086/swc.2011.12.28>.
- Vicente, G.A., Davenport, J.C., Scofield, R.A., 2010. The role of orographic and parallax corrections on real time high resolution satellite rainfall rate distribution. *Int. J. Remote Sens.* 32 (2), 221–230. <http://dx.doi.org/10.1080/01431160010006935>.
- Vignola, F.E., McMahan, A.C., Grover, C.N., 2013. Bankable solar-radiation datasets. In: Kleissl, J. (Ed.), *Solar Energy Forecasting and Resource Assessment*. Elsevier, pp. 97–131. <http://dx.doi.org/10.1016/B978-0-12-397177-7.00005-X> (Chapter 5).
- Wilcox, S., Andreas, A., 2010. Solar Resource & Meteorological Assessment Project (SOLRMAP): Observed Atmospheric and Solar Information System (OASIS), Tucson, Arizona (Data). <http://dx.doi.org/10.7799/105226>.

APPENDIX E

LIST OF PUBLICATIONS CO-AUTHORED BY A. T. LORENZO

Peer-reviewed publications:

1. goes here

Presentations and posters:

1. poster

Other works:

1. other stuff